UNIVERSITY OF OKLAHOMA

GRADUATE COLLEGE

DESIGN, SYNTHESIS, AND APPLICATION OF DUAL FUNCTIONING BODIPY PHOTOSENSITIZERS: A THERANOSTIC PHOTODYNAMIC APPROACH FOR CANCER THERAPY

A DISSERTATION

SUBMITTED TO THE GRADUATE FACULTY

in partial fulfillment of the requirements for the

Degree of

DOCTOR OF PHILOSOPHY

By
RYAN WATLEY
Norman, Oklahoma
2015

Downloaded from SHAREOK. Persistent Handle URL: https://hdl.handle.net/11244/14053

DESIGN, SYNTHESIS, AND APPLICATION OF DUAL FUNCTIONING BODIPY PHOTOSENSITIZERS: A THERANOSTIC PHOTODYNAMIC APPROACH FOR CANCER THERAPY

A DISSERTATION APPROVED FOR THE
DEPEARTMENT OF CHEMISTRY AND BIOCHEMISTRY

BY

_____
Dr. Ken Nicholas, Chair

_____
Dr. Youngjae You

_____
Dr. Ron Halterman

_____
Dr. George Richter-Addo

_____
Dr. Simin Pulat

© Copyright by RYAN L. WATLEY 2014
All Rights Reserved.

Acknowledgements

The design, synthesis, and application of dual functioning BODIPY Photosensitizers for a theranostic approach to cancer therapy is my contribution to aid in the quest for novel treatments. I sincerely dedicate my efforts to all who have been affected directly and indirectly due to lack thereof.

I would like to express my deepest gratitude to Dr. Youngjae You as he has allowed me to flourish not only as a scientist, but also as a young man with evolving morals and compassion for others. Under his guidance, I have established myself in society and will forever be grateful for his ability to enhance my ability to think critically and solve problems.

I will forever be grateful for The National Science Foundation Oklahoma-Louis Stokes Alliance for Minority Participation, Dr. Simin Pulat, Susy Colonkey and the Bridge to Doctorate Fellowship Committee for granting me the opportunity, financial assistance, and encouragement to complete the Ph.D. I also thank The Department of Chemistry and Biochemistry at the University of Oklahoma for accepting me as a graduate student and providing a stimulating, competitive, and yet conducive learning environment. Special thanks to all advisory committee members for their enriching input, furthering my matriculation specifically Professor Ken Nicholas. His extraordinary ability to convey organic chemistry instilled the needed confidence to obtain the Ph.D. In addition, he has chaired my committee with the purpose of completing the degree with excellent writing, presentation, research, and critical thinking skills.

My findings for improving cancer therapy would not be possible without the financial support of The Oklahoma Center for the Advancement of Science and Technology (OCAST). Furthermore, I am grateful for The Department of Pharmaceutical Sciences in the College of Pharmacy at The University of Oklahoma Health Science Center for the use of its research facilities. I am thankful for Dr. Francis D'souza at the University of North Texas for being a dependable collaborator and his insight into the photochemical mechanism of my analogs.

I thank my wonderful mother Annitha, father Roland, and siblings Sanreka, Terrance, Brandon, Raulanda and Robyne for their consistent support, sacrifice and encouragement. Also, I could not have written and defended this dissertation without the impact of my grandparents the late Robbie London and Jeletha Watley. As a matter of fact, the entire London, Blunt, and Watley family were influential in my arrival. I will always have a great love for the founders of the Omega Psi Phi Fraternity, as my joining of such an esteemed group focused my daily efforts to revolve around scholarship, manhood, perseverance and uplift. Life is a series of attempts to accomplish specific, yet honorable goals. I pray this accomplished goal will influence our next generation of leaders to understand their limitations and capabilities and work to overcome them.

Lastly, but most importantly, I thank my Lord and savior Jesus Christ for his grace, mercy, and favor.

Table of Contents

Page

Acknowledgments…….…… iv

Table of Contents…….……vi

List of Tables ……...……ix

List of Figures..…….…….……x

Abstract…….……xiii

Chapter I. Introduction

1.1 Photodynamic Therapy (PDT)…….……6

1.2 Light Sources…..……...…….8

1.3 Singlet Oxygen ($^1O_2$)…...……... 9

1.4 Photosensitizer (PS)……...…..11

1.5 Fluorescence Imaging …….....15

1.6 Photosensitizer Fluorescence Detection (PSFD), Guided Resection and PDT...20

1.7 Chemical Strategies for Production of NIR BODIPY Dyes……..21

1.8 *meso*-Functionalization of BODIPY.....……..……..23

1.9 2,6- BODIPY Functionalization……..24

1.0.1 3,5-BODIPY Functionalization……..…….25

1.0.2 Modification of BORON Center……..……...26

1.0.3 Extended Conjugation Through Rigid Ring Fusion……...…….27

1.0.4 Biological Application of BODIPY Fluorophores ……...…..28

1.0.5 Biological Labels…….30

1.0.6 Enzyme Substrates……...……32

1.0.7 Environmental Indicators……...…….33

1.0.8. Cellular Satins……...……..34

Chapter II. Design and Synthesis and Mechanistic Investigation of NIR Dual Functioning BODIPY PS

2.0 Introduction……..36

2.1 Design and Synthesis of NIR Dual Functioning NIR BODIPY Analogs……....40

2.2 Results and Discussion……42
2.3 X-ray Structural Analysis of SBDPiR690…….……..43
2.4 Optical Properties……..……..44
2.5 DPBF Method for Detection of Singlet Oxygen Generation……..……47
2.6 Electrochemical Potential……...……49
2.7 Mapping of HOMO-LUMO Energy Levels……50
2.8 Time Resolved Transient Absorption Spectra……...……..52
2.9 Conclusion…….……..59
2.10 Experimental and General Methods……60

Chapter III. Application of NIR Dual Functioning BODIPY PS SBDPiR690

3.0 Introduction……75
3.1 *In vitro* Photo and Dark Toxicity……76
3.2 Drug-Bio-distribution and Clearance using SBDPiR690……78
3.3 Whole Body *In Vivo* Imaging……..……80
3.4 Optical Guided SBDPiR690 Photodynamic Therapy…….81
3.5 Conclusion……...……84
3.6 Experimental Conditions……...……..85

Chapter IV. Functionalization and Optical Properties of NIR Dual Functioning PS

4.0 Introduction……...……..86
4.1 Synthesis of Peripheral Functionalized NIR BODIPY SBDPiR690-COOR…..87
4.2 Optical Properties of SBDPiR690-COOR……..…88
4.3 Extinction Coefficient SBDPiR690-COOR……90
4.4 DPBF Method for Detection of Singlet Oxygen SBDPiR690-COOR……..…..91
4.5 Functionalized Intermediate BDP635-COOR…….……92
4.6 Functionalized Theranostic PS SBDPiR688-COOR…….……..93
4.7 Optical Properties of SBBDPiR688-COOR……...….94
4.8 Extinction Coefficient of SBDPiR688-COOR ……..…….96
4.9 DPBF Method for Detection of Singlet Oxygen of SBDPiR688-COOR……....96
4.0.1 Conclusion……...98

4.0.2 Experimental and General Methods ……...……98

Chapter V. Conclusion and Perspective……104

References……123

Appendix ……118

Cyclic Voltammogram and differential pulse volatammetry……118

List of Abbreviations ...……...…...119

List of ^{1}H NMR……..……120

List of Reaction Schemes ……..……121

Singlet Oxygen Luminescence……..122

SBDPiR690 X-Ray data table (Table 5)……...123

High Pressure Liquid Chromatography……132

List of Tables

Table Page

1. Near-Infrared fluorescent probes……..……18
2. Optical properties of select second generation photosensitizers…….38
3. Optical properties of dual functioning BODIPY photosensitizers……..46
4. Summary of redox potentials and HOMO/LUMO calculations……..51
5. Crystallography data……..….123

List of Figures

Figure Page

1. Leading cause of death in the United States from 1958 to 2010…….....2
2. Modified Gompertizian diagram of tumor burden……3
3. Photodynamic therapy protocol…….6
4. Simplified Jablonski diagram of Type I and II PDT mechanisms……7
5. First and second generation porphyrin based photosensitizers……...14
6. Simplified Jablonski diagram illustrating fluorescence imaging……17
7. Structure of BODIPY core……..……23
8. Structure of *meso*-substituted BODIPY…….……24
9. Resonance structure of BODIPY core ……..……..25
10. Chemical structures of 3,5-substituted BODIPY……....26
11. Chemical structure of boron substituted BODIPY……..……27
12. Chemical structure of rigid BODIPY …….27
13. Autofluorescence of tissue…….…….29
14. Illustration of BODIPY biological application……...….30
15. Structures of BODIPY with reactive functional group ……..32
16. Structure of fluorescent BODIPY probes as bio-sensors……34
17. Structure of fluorescent BODIPY probes for labeling……....35
18. Structure of first and second generation PSs…….……..37
19. Structures of BODIPY PSs incorporated with heavy atom halogens…..39
20. Structures of thiophene fused BODIPY……..41
21. ORTEP view of **SBDPiR690** X-ray crystal structures……43
22. Absorbance spectra of **SBDPiRs**…….....45
23. Fluorescence spectra of **SBDPiRs**……...45
24. DPBF oxidation by **SBDPiRs**.....48
25. Mapping of HOMO-LUMO energy levels……..……51
26. **SBDPiR690** Femto-second transition absorption spectrum……53
27. **SBDPiR731** Femto-second transition absorption spectrum……54
28. **SBDPiR690** Nano-second transition absorption spectrum ……55
29. **SBDPiR731** Nano-second transition absorption spectrum…….56

30. **SBDPiR690** Nano second decay spectrum ……..……..57
31. **SBDPiR731** Nano second decay spectrum ……58
32. ^{1}H NMR of compound **35**……...……...……..61
33. ^{1}H NMR of compound **36**……....62
34. ^{1}H NMR of **BDP635**…….…..63
35. ^{1}H NMR of **SBDPiR690**…….……64
36. ^{1}H NMR of **SBDPiR731**…….....65
37. ^{1}H NMR of **SBDPiR698**…….……66
38. ^{1}H NMR of **SBDPiR688**…….……67
39. HRMS EI of **SBDPiR688**……..……68
40. ^{1}H NMR of **SBDPiR740**…….69
41. ^{1}H NMR of **SBDPiR710**…….70
42. LRMS EI **SBDPiR710**……...…….71
43. ^{1}H NMR of **SBDPiR700**…….……72
44. HRMS EI of **SBDPiR700**……...……73
45. **SBDPiR690** *in vitro* photo-and dark toxicity……..……78
46. **SBDPiR690** *ex vivo* bio-distribution pattern…….……..79
47. **SBDPiR690** Whole body *in vivo* imaging……..……80
48. Tumor growth curve under experimental conditions……..…82
49. Mouse images pre and post photodynamic therapy with **SBDPIR690**...83
50. Kaplan-Maier plot of mouse survival……..…84
51. **SBDPiR690 SBDPiR690-COOR** absorbance spectrum……..……..89
52. **SBDPiR690 SBDPiR690-COOR** emission spectrum ……..…89
53. **SBDPiR690-COOR** extinction coefficient plot…….90
54. **SBDPIR690 SBDPiR690-COOR** DPBF oxidation…….…..92
55. **SBDPiR688 SBDPiR688-COOR** absorbance spectrum……95
56. **SBDPiR688 SBDPiR688-COOR** fluorescence spectrum…….95
57. **SBDPiR688-COOR** extinction coefficient plot…….96
58. **SBDPiR688 SBDPiR688-COOR** DPBF plot……..…….97
59. ^{1}H NMR of **SBDPiR690-COOR**……99
60. HRMS EI of **SBDPiR690-COOR**……..……..100

61. ^{1}H NMR of **BDP635-COOR**……..…..101
62. HRMS EI of **BDP635-COOR**……..……101
63. ^{1}H NMR of **SBDPiR688-COOR**……..103
64. HRMS EI of **SBDPiR688-COOR**……103
65. Cyclic voltammogram and differential pulse voltammetry……...…128
66. Singlet oxygen luminescence……...…….130
67. HPLC chromatogram of **SBDPiR690**……...……131
68. HPLC chromatogram of **SBDPiR698**……...……131
69. HPLC chromatogram of **SBDPiR688**……...…133
70. HPLC chromatogram of **SBDPiR710**……...……134

Abstract

DESIGN, SYNTHESIS, AND APPLICATION OF DUAL FUNCTIONING BODIPY PHOTOSENSITIZERS: A THERANOSTIC PHOTODYNAMIC APPROACH FOR CANCER THERAPY

Ryan Watley

2014

Development of concomitant photodynamic therapy (PDT) and photosensitizer fluorescence detection (PFD), termed theranostics, is of primary interest as combining the two modalities stands to offer a more personalized cost effective "see, treat, and monitor" approach. As a minimally invasive drug-device strategy, the standard protocol involves photosensitizer (light sensitive drug) or fluorophore administration followed by light activation. Specifically, PDT is an approved regimen for the treatment of non-malignant and neoplastic disease. The cytotoxic effect derives from an activated photosensitizer reaction with local oxygen, which produces a tumor damaging species known as singlet oxygen. PFD employs a fluorophore as an invaluable tool for monitoring photosensitizer bio-distribution along with delineating healthy and diseased tissue in the native environment. The two, PDT and PFD, are distinguished via competing photochemical mechanism of administered drugs, which in part hampers their combined application.

A photosensitizer's therapeutic efficacy is invariably linked to intersystem crossing, which attenuates fluorescence required for imaging. Improving fluorescence yield of photosensitizer's stands to impart information concerning drug location and

concentration. These parameters are vital for determining the optimal time of illumination within PDT. Furthermore, fusion of PDT and PFD enables impromptu eradication of detected disease and subsequent monitoring of photodynamic response when targeted photosensitizers are used.

This dissertation explores the design and synthesis of NIR dual functioning mono-BODIPY photosensitizers for optical image-guided PDT. The synthetic methodology excludes conventional incorporation of halogens as heavy atoms, which alter photophysical properties. Moreover, identification of the key structure photophysical property relationship for obtaining both effective fluorescence and singlet oxygen generation was uncovered along with elucidation of the photochemical mechanism. Above all, application through fluorescence bio-distribution studies and whole body *in vivo* imaging facilitates more effective tumor ablation through optimizing drug-light intervals for PDT.

The objective of this dissertation is to develop NIR BODIPY photosensitizers applicable for imaging and therapy with one PS. Chapter I describes ingenious efforts to develop NIR BODIPY dyes, yet none have surfaced as dual agents for fluorescence detection and therapy. In addition, Chapter I highlight functionalization of NIR BODIPY dyes for improving water solubility, and tethering to cancer specific biomolecules.

In Chapter II, citing the weak fluorescence of porphyrin based PS and populated triplet state of BODIPY fluorophores, intersystem crossing and production of singlet oxygen was accomplished without the use of heavy halogen atoms such as Br and I. The heavy atom effect significantly reduces the fluorescence, thus limiting its dual-application. BODIPY and thiophene units were fused for extended conjugation with varying electronic effects. An investigation into the structure photophyscial property relationship concluded electron-withdrawing groups enable singlet oxygen generation absent conventional heavy atom incorporation. The lead compound, **SBDPiR690** has an inherent brightness and phototoxic power of 26,400 $M^{-1}cm^{-1}$ and 50,400 $M^{-1}cm^{-1}$, respectively. The design and synthesis of several analogs resulted in an improved **SBDPIR688** analog with a brightness of 37, 440 $M^{-1}cm^{-1}$ and phototoxic power of 45,120 $M^{-1}cm^{-1}$.

Chapter III demonstrates the translation of our lead compound **SBDPiR690** photo physical properties *in vitro* and *in vivo.* Specifically, concentration dependence on cell survival illustrates minimal dark toxicity at the cell monolayer. Furthermore, brightness of the parent compound proved advantageous for non-invasive imaging of bio-distribution. The pharmacokinetic pattern helps establish an optimal drug light interval for vascular-targeted PDT, which was successful in total eradication of sub-cutaneous colon 26 tumor.

In Chapter IV, we modify parent compounds through incorporating functional groups potentially facilitating improved aqueous solubility and overall improved

pharmacokinetics. The inclusion of ester moieties through substitution of the boron center disrupts singlet oxygen generation in our improved analog SBDPiR688. However, ester synthons at the peripheral sites of the lead compound SBDPiR690 maintain its therapeutic capability through singlet oxygen generation. The ester functionality offers potential conjugation of target specific ligands for improved pharmacodynamics.

Chapter I. Introduction

Cancer is a disease characterized by the growth and proliferation of abnormal cells.[1] Among the five leading causes of death between 1958 and 2010 cancer ranked second to heart disease.[2] However, heart disease fatalities have consistently declined, while the impact of cancer has remained by and large constant.[3] According to this rate, it is probable cancer will soon become the leading cause of death (Fig. 1). Advances in research, particularly sequencing of the human genome[4], have afforded a better understanding of the tumor microenvironment and thus the evolution of malignant disease. The causes of cancer are multiple and vary through exposure to carcinogens (e.g. chemicals, radioactive material, and viruses) that initiate aberration in proto-oncogenes, which are biomolecules that control normal cell growth.[5] Promotion of modified proto-oncogenes results in neoplastic lesions. The latter are transformed to clinical cancer and metastasis, which defines the progression of transformed cells. Overall initiation, promotion, transformation, and metastasis are the distinct phases of cancer evolution and is coined multistep carcinogenesis.[6]

Chemotherapy and surgery are prominent treatments for eradicating the growth and proliferation of abnormal cells. The gompertzian diagram below (Fig. 2) is a model of malignant tissue growth versus time in respect to established therapeutic modalities.[7] The red legend indicates tumor burden (cell growth), which can be diagnosed at 10^9 cells, symptomatic at $10^{10\text{-}11}$ cells, and can be fatal at or beyond 10^{12} cells. The blue legend represents infrequent rounds of chemotherapy with each reduction in tumor

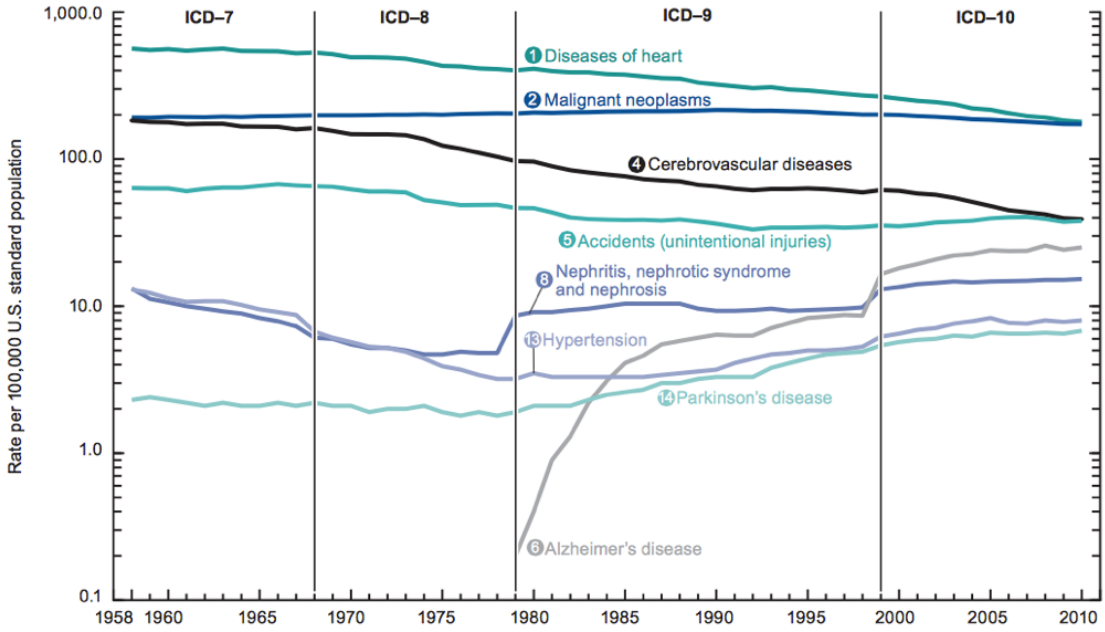


Figure 1. Leading cause of death in the United States from 1958 to 2010.[8]

burden signifying cell kill. However, the cell growth rate is greater than the rate of cell kill. Overall, infrequent rounds of chemotherapy at the symptomatic stage only prolong survival. The light blue legend represents frequent rounds of chemotherapy at the diagnostic stage. The cell kill rate is greater than the cell growth rate; however, the dosage is over an extended period of time. Surgical resection significantly reduces the tumor burden in a short span. Adjuvant chemotherapy is efficient at total eradication of tumor growth with frequent doses. The diagram clearly illustrates the effectiveness of surgery adjuvant chemotherapy, but of note is the considerable small margin between the diagnostic stage and fatality. Early detection is vital for therapeutic suppression and eradication of the cell growth rate.

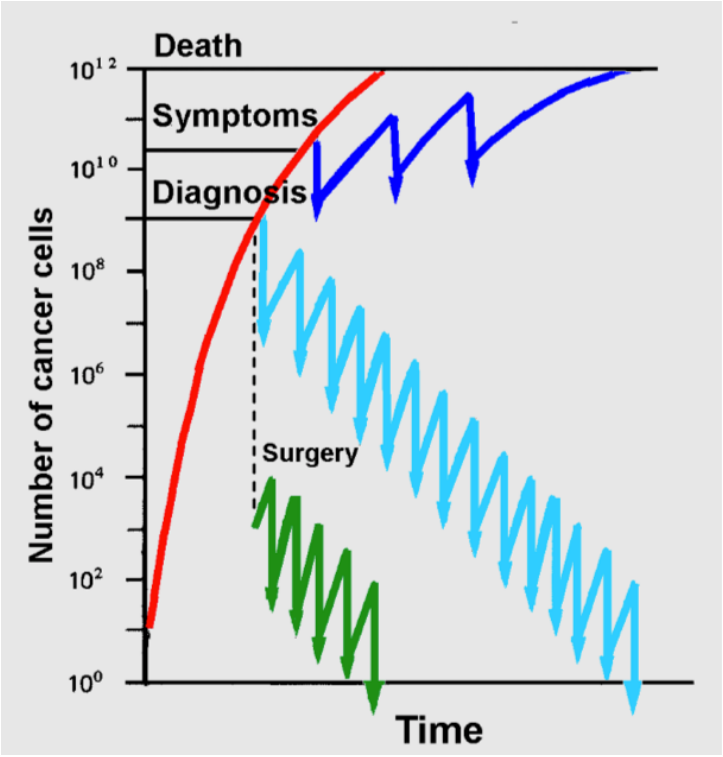


Figure 2. Modified gompertzian diagram of tumor burden versus time in respect to conventional therapy techniques.[7, 9]

Magnetic Resonance Imaging (MRI) and Positron Emission Tomography (PET) have been firmly established as diagnostic modalities.[10] However, MRI exposes patients to large magnetic fields and is limited to macroscopic imaging.[11] In contrast, PET is sensitive enough to diagnose at the microscopic level but involves the use of radioactive agents.[12] Radioactive agents are known carcinogens. Near IR fluorescence imaging is a sensitive technique for detecting and visualizing cells at the microscopic level.[13] While it is limited in terms of resolving cellular events, the technique has been invaluable for demarcating malignant and normal cells during surgical resection.[14] This technique, as well as its limitations, will be discussed more in depth within sections 1.5 and 1.6.

The established therapy modalities (e.g. surgery, radiotherapy, and chemotherapy) are successful at reducing tumor burden. However, patients often succumb to side effects. Surgical resection of organs and/or amputation of limbs can significantly alter patients' lives. Furthermore, due to function of certain tissue and/or proximity to vital healthy tissue, surgery is not a habitual option. Radiotherapy seeks to offer selectivity of cancer cells through matching the geometry of tumor with radioactive beams despite radiation being a known carcinogen.[15] Chemotherapeutic agents lack the ability to decipher between healthy and malignant cells. This manifests changes in physical appearances and poor prognosis (e.g. alopecia, pneumonia, and organ failure). Target-specific agents have demonstrated early clinical prominence, yet extensive investigations yield slight improvements in therapeutic outcomes.[16] Moreover, the significant financial commitment and invested time for procuring novel agents are disparaging as drugs entering clinical and commercialization continue to decline.[17] These facts and the persistent threat of cancer demand expansion of primary therapy regimens to include effective yet under-developed approaches.

Theranostics is the combination of detection (diagnostic) and therapy concomitantly with the goal of achieving personalized medicine through real time monitoring and tuning of therapy and dose. Theranostic Photodynamic Therapy was designed to improve prognosis and therapy due to its dual selectivity, use of non-ionizing material, and relatively low cost, yet it is not primarily considered. Clinical and preclinical research aims to promote theranostic PDT through the development of near-infra-red (NIR) fluorescent photosensitizers as detection and therapeutic (theranostic) agents that

derive from inorganic (nano-particles) and organic scaffolds. The effort is attributed in part to the optical advantages associated with the "biological window" (700-900 nm) including minimal endogenous chromophore interference and reduced light scattering. Photofrin and Protoporphyrin IX, discovered by Doughtery[18] and Kennedy[19] respectively, are among approved photosensitizers used for imaging and therapy of esophageal, bladder, and brain cancers.[20] However, the optical properties are less than ideal, which limit their application and the expansion of theranostic PDT. In addition, more sensitive agents are needed for detection of neoplasms and overall improvement of treatment and patient survival.[21] Organic-based dyes such rhodamines, fluoresceins, and cyanines have proven to be advantageous in terms of imaging compared to porphyrin-based PS[22] but fail to address theranostic photodynamic therapy limitations comprehensively. The difluoro-boroindacene family (4,4-difluoro-4bora-3a,4a-diaza-s-indacene), abbreviated hereafter as BODIPY[23], has earned increasing interest for excellent optical properties and is established as a versatile heterocyclic scaffold.[24]

The central focus of this work investigates structural determinants of NIR BODIPY analogs for balanced fluorescence emission and singlet oxygen generation for overall effective brightness and phototoxic power. The work: 1) develops NIR dual-functioning photosensitizers through the variation of electronic properties, 2) elucidates the photochemical mechanism using transition absorption spectroscopy, 3) demonstrates application of dual functioning BODIPY photosensitizers for optical imaging and photodynamic therapy, and 4) incorporates reactive functional moieties enabling tethering of target-specific ligands. The following sections will discuss the intricacies

and current state of the art of PDT. In addition, select literature of BODIPY dye application as imaging and therapeutic agents is introduced in support of this approach to design brighter and more phototoxic BODIPY theranostic photosensitizers.

1.1 Photodynamic Therapy (PDT)

The photodynamic effect achieved in PDT derives via three essential components of light, photosensitizer, and oxygen.[25] Individually none are therapeutic but together initiate a photochemical molecular oxygen reaction producing the cytotoxic singlet oxygen.[26] The clinical protocol begins with administration of a photosensitizer. After sufficient time delay (drug-light interval), the PS ideally accumulates within the desired location, and light is focused to illuminate the target tissue (Fig. 3).[27]

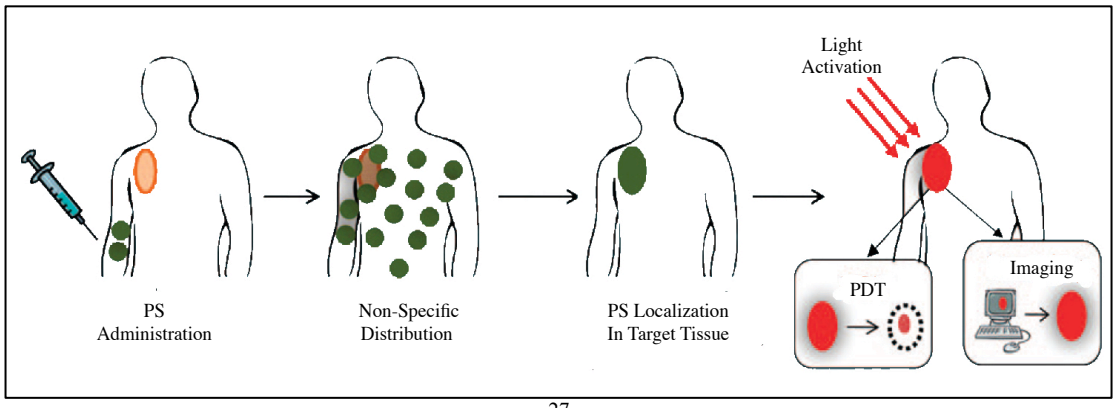


Figure 3. Photodynamic therapy protocol[27], reprinted with permission from [4]. Copyright (2010) American Chemical Society.

Theoretically, the interaction of light and accumulated photosensitizer yields a singlet state photosensitizer (^{1}PS).[28] The excited state molecule internally converts and energy can be lost via fluorescence to the ground state or intersystem crossing to a triplet state

and yields a triplet state photosensitizer (^{3}PS). The latter process causes an antitumor effect via a type I or II mechanism.[29] The type I mechanism is a direct PS reaction with biological molecules that forms radicals and subsequent superoxides. The type II mechanism, the widely accepted photochemical process, involves an energy transfer from the triplet state PS to native oxygen at the diseased site to produce toxic singlet oxygen (Fig. 4).[30]

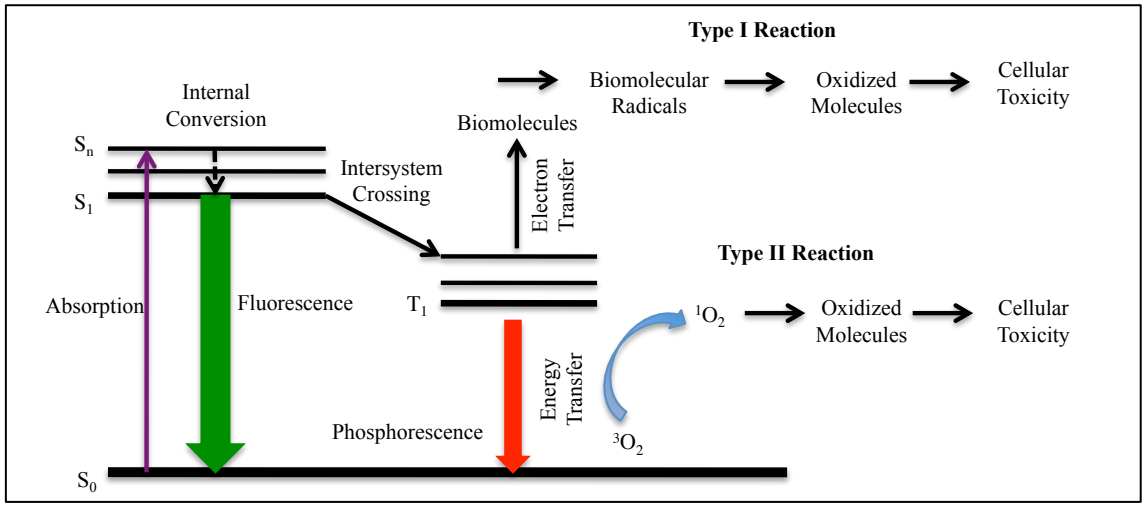


Figure 4. Simplified Jablonski diagram of type I and type II PDT cell-death mechanisms.

The cell death mechanism, e.g. necrosis or apoptosis, is a direct result of the type and dose of PS used, drug-light interval, and dosimetry. PDT is believed to synergistically induce tumor damage through vascular hemorrhage, direct cell kill, and stimulate the innate immune system.[30] The advantages of PDT are found in the ability to control the site specific dug activation; however, for primary clinical use, adequate improvements in light source and photosensitizer properties are needed.

1.2 Light Sources

Photosensitizer development and technological advances, which includes a multitude of devices such as light sources, delivery method techniques, and instruments for dosimetry, have driven and enabled the advancement of clinical PDT. Light sources are determined by PS absorption and ability to generate sufficient power to the disease location ergonomically with high efficiency.[31] The conventional light dose consists of 1-5 watts of power within the 630-850 nm wavelength range and irradiances up to hundreds of mW cm^{-2}.[32] The wavelength range, also known as the therapeutic window, is critical for optimizing tissue penetration of light as endogenous chromophores of hemoglobin derivatives and water can absorb incident light below and beyond this range.[33]

Light sources have emerged primarily from three categories: broad emission filtered lamps, lasers, and light emitting diodes (LED). Early clinical treatments involved oversized argon-ion lasers, which are less than ideal for the clinical setting due to constant realignment with the target and the short wavelength emission bands.[31] Solid-state lasers have surfaced offering a more compact design while maintaining high power and the advantage of wavelength tunability; yet remain expensive and with many technicalities.[34] Broadband emission lamps have the advantage of being applicable to all photosensitizers through the incorporation of narrowband and long-pass filters for absorption compatibility.[35] However, broadband output and power are difficult to encapsulate within optical fibers. The latter is required to excite deep-seated tissues that are only accessible through biological orifices. Therefore, a large tradeoff exists

between broadband excitation and power. This limits lamp excitation sources to superficial lesions.[36]

Recently, diodes lasers have been explored as viable options for photosensitizer excitation sources. Diode lasers are compact, inexpensive, high powered, and cover visible to NIR absorptions. Conversely to lamp sources, diodes can be coupled with endoscopes for expansion of PDT to deep-seated malignancies.[37] As diode lasers are state of the art, future advances include organic diodes and configurable diode geometry for matching targets. Furthermore, efforts are being made to reduce source cost, which could facilitate community and eventual home-care application.[32]

1.3 Singlet Oxygen ($^1O_2$)

The interaction of light, photosensitizer, and molecular oxygen results in photodynamic action through inactivation of viruses and cells.[38] As shown in figure 4, singlet oxygen generated via the type II reaction is the final integral component responsible for an anti-tumor effect. Prior to this reaction, quenching or deactivation of the lowest triplet excited state by molecular oxygen (O_2) is required for production of singlet oxygen.[39] Singlet oxygen can exist in two states, ($^1\Sigma_g$) and ($^1\Delta_g$), and both are formed in the event energy transferred from the triplet state is $\geq$ 157 kJ mol^{-1}, the energy of the upper excited state ($^1\Sigma_g$).[40] The lowest excited state of singlet oxygen, has an excited state energy of 94 kJ mol^{-1}. Upon formation of the highest state, the highly reactive but metastable singlet oxygen ($^1\Delta_g$) is achieved through electronic and vibrational energy transfer.[41]

The efficiency of singlet oxygen generation is known as the singlet oxygen quantum yield (ϕ_Δ).[42] This parameter is the prime indicator of a photosensitizer's ability to cause a photodynamic effect. The ϕ_Δ is an integer that exists between zero and one, with one representing the ideal case. This scale has been established on the principle of one absorbed photon can maximally produce one molecule of singlet oxygen. Again, the ideal case is every photon absorbed yields one molecule of singlet oxygen.[42]

Many methods have been developed, tested, and applied for determination of the singlet oxygen quantum yield. Various techniques for accurate values include direct methods such as time resolved near-infrared luminescence and time resolved thermal lensing (TRTL). The 1290 nm NIR emission of $^1\Delta_g$ allows it to be monitored directly by NIR luminescence.[43] Conventional indirect methods for determined singlet oxygen quantum yields include chemical trapping and direct monitoring of O_2 consumption. Indirect techniques for determining singlet oxygen quantum yields are common in that the quantum yields can be determined without the use of expensive and specialized instrumentation. In addition, most indirect chemical trapping methods, particularly oxygenation of 1,3-diphenylisobenzofuran (DPBF) and *p*-nitrodimethylaniline (RNO), are routine well-understood experiments due to considerable work elucidating singlet oxygen and acceptor mechanisms.[44]

Monitoring of molecular oxygen consumption for singlet oxygen quantum yield involves measuring the oxygen concentration in the presence of a photosensitizer and

singlet oxygen acceptor before and after excitation. The acceptor essentially traps singlet oxygen produced via excitation of PS, and modifies the oxygen concentration in the system. While ϕ_Δ is effective for assessing PS within the cell mono-layer, *in vivo* evaluation is better characterized by its phototoxic power (PP), which is the product of extinction coefficient (ε) and singlet oxygen quantum yield.[25]

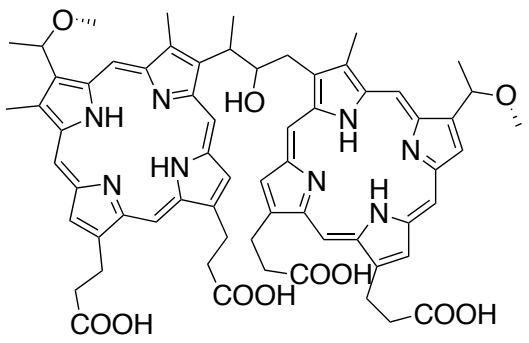
1.4 Photosensitizers

Photosensitizers are the essential component in PDT. While therapy through light drug interaction dates back to the mid 1800s, the current era of photosensitizer development was given birth through investigations of hematoporphyrin by S. Schwartz and R.L. Lipson at the Mayo clinic in the 1960s.[20, 45] Lipson *et al.* were able to accomplish optimal tumor localization and enhancement of fluorescence diagnostic efficacy through purification of crude porphyrin. These efforts solidified the utility of porphryin as a diagnostic tool.

Dougherty *et al.* later discovered hematoporphyrin derivative's potential as a photosensitizer upon observation of partial and complete response to PDT.[46] Such promising antitumor activity led to its commercialization as the first approved PS for Barret's esophageal, cervical, papillary, endobroncheal, gastric, and papillary bladder cancers.[47] Commonly known as Photofrin, it is one of the most widely used clinical PSs.[48] While effective, Photofrin exists as a mixture of dimers and high oligomers, has lasting side effects such as skin phototoxicity, and sub-optimal absorbance at 640 nm. These limit Photofrin PDT's application to deep-seated malignancies.[49]

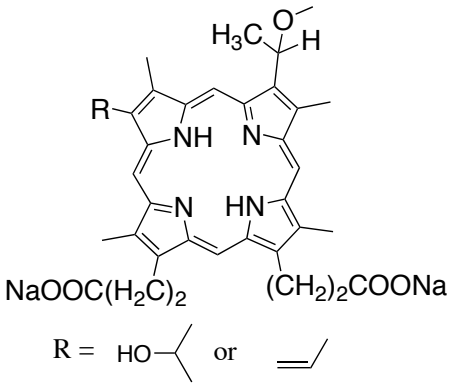
These findings spawned the development of several second-generation photosensitizers, which have emerged to clinical trials attempting to surpass the shortcomings of Photofrin and meet the criteria of the ideal photosensitizer (Fig. 5). The ideal photosensitizers should 1) be chemically pure of a known composition with a reproducible synthesis for unambiguous interpretation of the overall effect, 2) have high extinction coefficient corresponding to the absorption in the NIR region 650 nm to 800 nm, (3) demonstrate preferential tumor accumulation and retention in addition to rapid clearance from outside organs of interest facilitated by water solubility, stability, and hydrophobic character, 4) have high singlet oxygen quantum yield for PDT, and 5) have balanced singlet oxygen and fluorescence quantum yields for dual functionality i.e. tumor eradication and fluorescence detection.[21, 25]

First generation photosensitizers



1

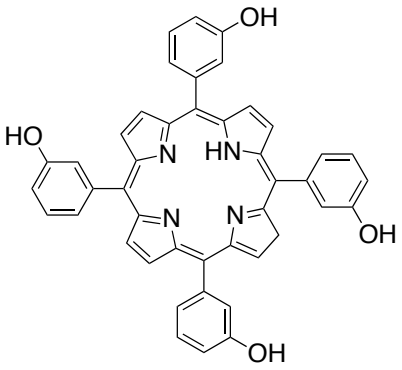
Haematoporphyrin
Derivative (HPD)
Lipson, Dougherty, Snell
and Kelly
advanced work in PDT



2

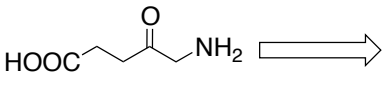
Photofrin
(simplified)
Clinical trials 1975-1999

Second Generation Photosensitizers



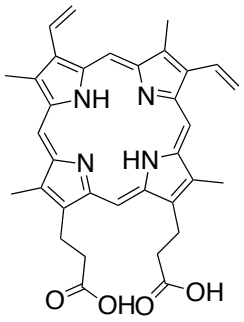
3

Foscan *m*-THPC
approved for head
and neck cancers



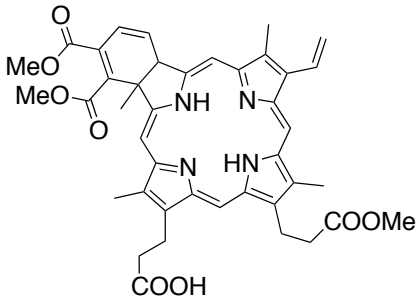
4

Aminolevulnic acid



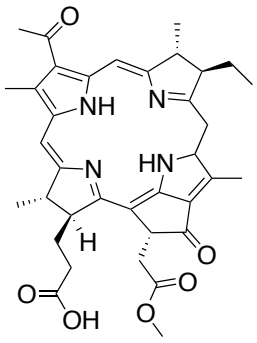
5

Protoporphyrin IX
Apporved as PDT
Prodrug and for
Fluorescence Detection



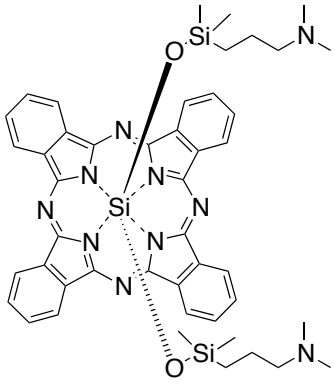
6

Benzoporphyrin
Derivative
(Verteporfin
approved for AMD



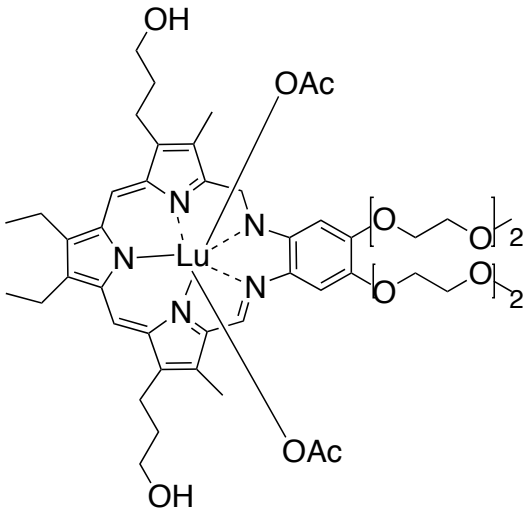
7

Padoporfin (Tookad)
Approved for Prostate Cancer



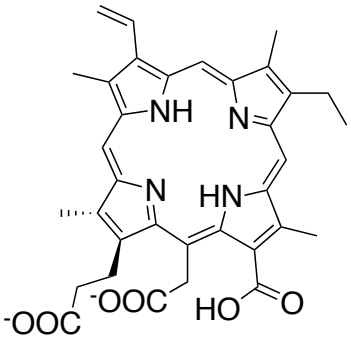
8

Pthalocyanine 4 (Pc4)
T-cell lymphoma clinical trial



9

Texaphyrin
(LuTex)
Breast Cancer Clinical Trials



10

Chlorophyll-a derivtive
(Radachlorin) clinical trial for
various cancer

Figure 5. FDA approved and current clinical trial first and second generation porphyrin based PSs.[47, 50]

A new era of photosensitizer development is currently in effect as the design, synthesis and application of NIR target specific and/or activatable dual functioning photosensitizers are being investigated. Conjugating second-generation photosensitizers with tumor specific moieties such as folic acid, carbohydrates, and peptides or tethering to biologically active molecular beacons demonstrate encouraging photodynamic efficiency *in vitro* and *in vivo*.[21, 51] However, investigations into active and passive targeting of photosensitizers by Pandey *et al*. concluded with emphasis on respective compounds' partition coefficients i.e. lipophilicity contribute to enhanced permeation and retention of PS, which leads to more effective photosensitization.[21] These structure activity relationship studies have provided pertinent information for the design of novel target selective photosensitizers.

1.5 Fluorescence Imaging

The observation of human body systems with light is perhaps one of the most practiced imaging techniques in clinical and biomedical research as it enables characterization of intact tissue.[52] Early clinical implementation involved the use of metal rigid bronchoscopes to visualize air passageways for detecting disease tissue. Many risk, such as the need for sedation, damaging of vocal cords, scratching and tearing of tissue led to the development of the first flexible fiber optic bronchoscope.[53] Imaging capability further evolved upon incorporating an excitation light with the flexible fiber inventing a novel highly sensitive light induced fluorescence emission (LIFE) endoscopy technique.[54] This method exposes tissues to a broad excitation spectrum (white light) and clinicians are able to observe the autofluorescence of normal/abnormal tissue for identifying gross morphology changes. Underpinning this technique is the optical properties of chromophores embedded within human tissue. These chromophores vary depending on cell type and absorb light between 200 nm – 500 nm and have an emission spectrum over the 300 nm – 700 nm range.[55] Clinicians ultimately excite the tissue of interest and obtain detailed functional and anatomical information.

LIFE optical imaging has been revolutionized through the development of fluorophores as a means of contrasting or delineating regions of tissue of interest. Localization of exogenous fluorophores offers highly sensitive fluorescence detection of neoplastic lesions, including mapping of molecular events for retrieval of new biomarkers.[27] The new state of the art has been fostered by the discovery, design, and synthesis of biocompatible fluorescent probes emitting light within the biological near infrared

window.[22] Fluorophores offer advantages of stability and limited toxicity in contrast to radiolabeled compounds, which have limited half-lives and may cause exposure of ionizing radiation to both patient and clinician.

Theoretically, fluorophores absorb light in the ground state (S_0) and become excited to a singlet (S_n) state. Upon internal conversion to the S_1 state, this excitation energy is lost through radiative decay given off as an emission light. The excited state can also intersystem cross (ISC) to a triplet state and decay by phosphorescence to the ground state (Fig. 6). Loss of energy by either or both pathways can be harnessed for imaging application.[22] The florescence emission of molecules is characterized by the fluorescent quantum yield (Φ_{flu}). This parameter is defined as the ratio of photons emitted to photons absorbed.[42] However, fluorescence quantum yield alone is not adequate to characterize *in vivo* efficiency. The absorbance and emission efficiency should be considered for the design and application of fluorophores *in vivo* Brightness, the product of fluorescence quantum yield and extinction coefficient ($\Phi_{flu} \times \varepsilon$), is a more sufficient parameter to characterize fluorophores. The lone values of extinction coefficient or fluorescence quantum yield are often misleading, but their product is a comprehensive parameter to judge fluorophore effectiveness.

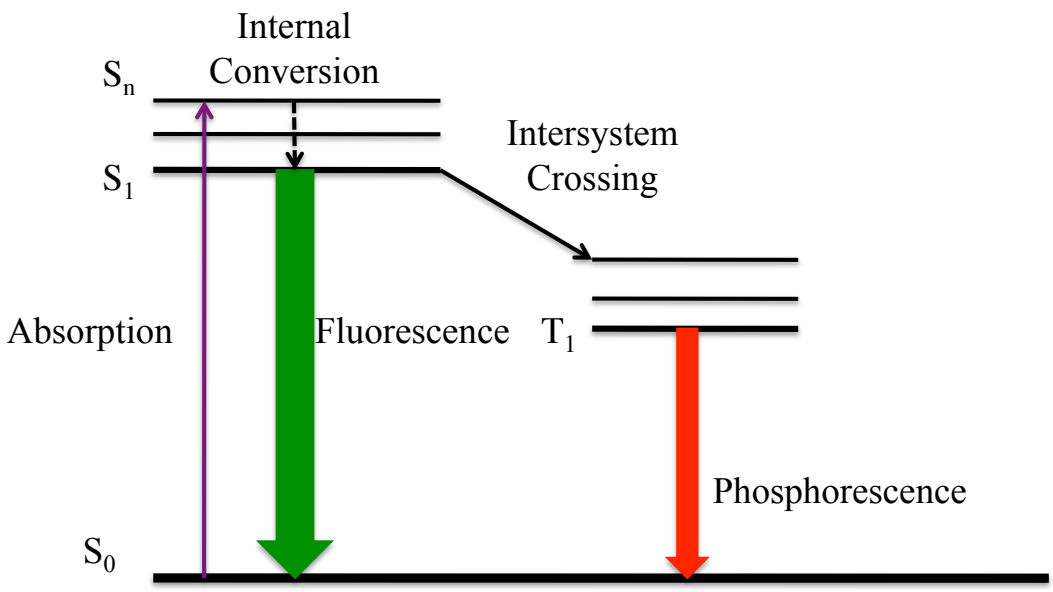


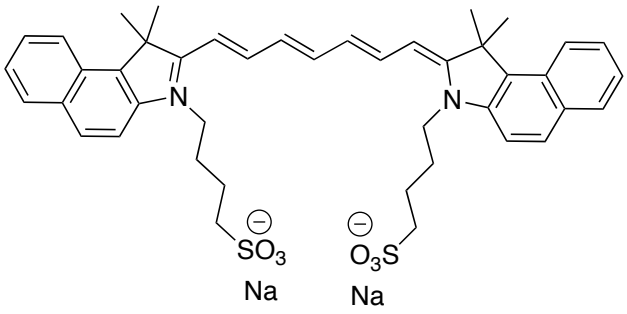
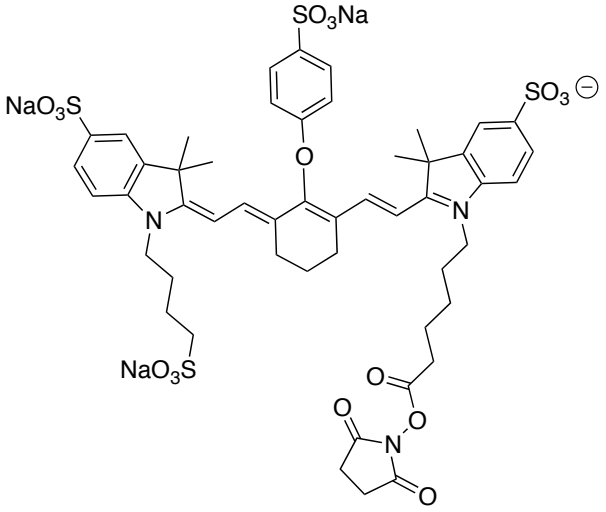
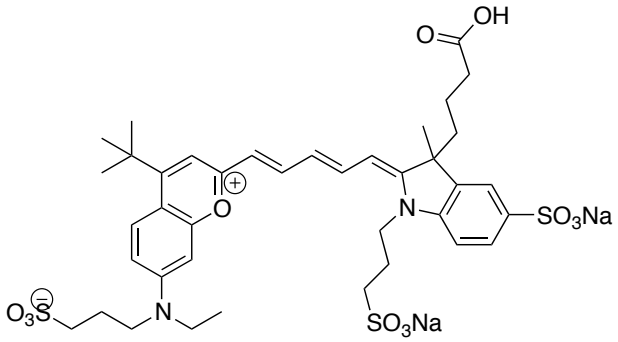
Figure 6. Simplified Jablonski diagram illustrating fluorescence imaging mechanism.

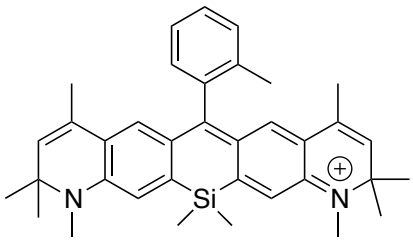
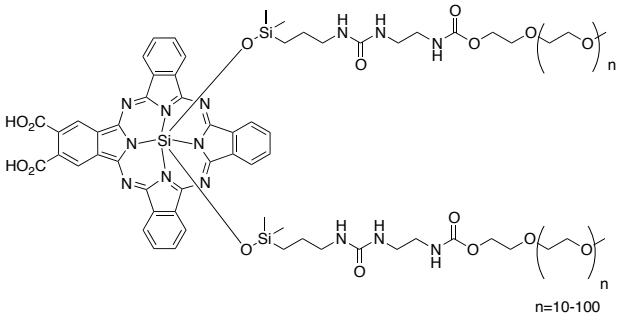
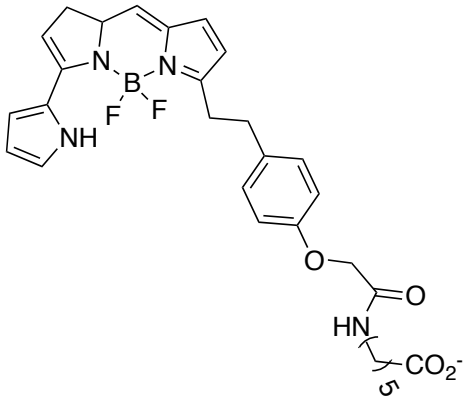
Efforts to enhance NIR dyes have been focused on classes of cyanines, squarines, pthalocyanines, porphyrins, and BODIPY skeletons (Table 1). The Food and Drug Administration has approved indocyanine green as a fluorescent probe for retinal angiography.[56] Despite its NIR absorption, ICG has a low quantum yield, (0.3% in water), lacks photostability, and is inert in terms of functionalization to biomolecules.[57] Improvement of photo/chemical stability, quantum yields, and water solubility of the mentioned alternative classes stands to yield more transparent information, as natural embedded chromophores are excluded by the near infrared excitation and emission.[53, 58]

In addition to NIR optical properties, the ideal dye should be synthetically feasible with inherent reactivity for inclusion of functional groups. IRDye800CW has established significant pre-clinical progress as it absorbs NIR light (800nm) and is functionalized

with N-hydroxysuccinide.[59] The reactive functional group allows tagging to receptor specific molecules for improved bio-distribution and target and tissue ratio.[55]

Table 1. NIR fluorescent probes [22]

NIR Dye	**Structure**	Abs. Max (nm)	Flu. Max (nm)
Indo-cyanine Green (ICG)		800	810
IRDye800CW NHS ester		778	794
DY-783 NHS ester		783	800

Si-R720		721	740
La Jolla Blue		680	700
BODIPY 630/650		646	660

Together, including the arrival of NIR lasers as ergonomic excitation sources and sensitive detectors[32], these have expanded the limitations of conventional UV optical techniques from 1-2 millimeter surface and subsurface imaging to achieve imaging depths of several centimeters.[55] However, fluorophores lack the ability to induce cell toxicity, which hampers their application as theranostic agents.

1.6 Photosensitizer Fluorescence Detection (PSFD), Guided Resection and PDT

The use of photosensitizers for imaging purposes facilitates a combinatorial approach for detection and therapy (theranostics) of cancer. Photosensitizers primarily serve as therapeutics due to their high singlet oxygen generation. However, garnishment of photosensitizer's minor, but effective fluorescence provides means for accurately determining the gap between drug administration and illumination, examining PDT mechanisms, and marking therapy responses.[27]

The two (PDT and PSFD) follow basic illumination principles but provide different outcomes through controlled light and photosensitizer dosages. For example Photofrin PDT serves to cause cell death with a drug concentration of 5.0 mg/kg while PSFD inflicts minimal to no cytotoxicity but instead fluoresces due to effective subtraction of background emission and photosensitizer concentrations of 0.25 mg/kg.[27, 60] PSFD dates back to early 1900s where Policard observed preferential malignant accumulation of heamatoporphyin through its fluorescence. Subsequent investigations into many first and second-generation photosensitizers have revealed innate ability to emit localized florescence and demarcate cancerous tissue upon illumination with UV light.[61] The endogenous conversion of the prodrug aminolevulinic acid into protoporhyrin IX (PpIX) has emerged a primary PSFD agent. PpIX is biologically formed in cells and chelated by iron as an intermediate via biosynthesis of hemoglobin. However, in most malignant tumors the chelation process by ferrocheletase is retarded. Administration of exogenous aminolevulinic acid mounts high concentration of PpIX where its fluorescence offers a stark contrast between healthy and malignant tissue.[62]

Photosensitizers primarily serve as therapeutics due to their high singlet oxygen quantum yield; however, the minor fluorescence capability has ushered the scaffold as a staple in surgery and PDT. The ability of porphyrin photosensitizers to localize and fluoresce optimizes surgical resection by visualizing small tumors with high sensitivity to define tumor and healthy tissue margins.[63] This in turn allows for exclusive PDT of those tissues that cannot be surgically excised. This development was paramount for resection of cancerous tissue, as keen precision is needed avoid healthy tissue. Incident removal of healthy tissue can drastically alter patients' quality of life and residual disease results in reoccurrence.[64]

Photosensitizer fluorescence detection has become more frequent in clinical and medical procedures.[27] This theranostic approach is invaluable for developing personalized methods to counter inadequate treatment outcomes and assist with identification of neoplastic lesions to bolster early detection, prevision of surgical intervention, and adjuvant therapy.

1.7 Chemical Strategies for Producing NIR BODIPY DYE

Advancements in the numerous fields of modern science and medicine have enabled the design of new fluorophores that can be illuminated within the red or near-infrared (NIR) region of the electromagnetic spectrum. These efforts have been aimed at visualizing intact biological tissue beyond the epithelial layer. Fluorophores of fluorescein and cyanine have long demonstrated clinical efficacy, yet novel scaffolds and strategies are needed to overcome problems of currently approved dyes and to expand application of

fluorescence imaging in the clinic.[65] Due to its advantageous photophysical properties and versatility for structural modification, BODIPY dyes have gained interest in attempts to translate these characteristics in biomedical application.

BODIPY dye consists of a dipyromethene ligand chelated with a di-substituted boron atom, which is commonly a BF_2 moiety. The joining of pyrrole units forms the dipyrromethene ligand via an interpyrolic methine bridge. BF_2 chelation constrains the fluorophore to a fixed planar π-electron system. The structural uniqueness offers a high photostability with an intense absorption and emission profile, high extinction coefficient (40,000 to 80,000 $M^{-1}cm^{-1}$), and high fluoresence quantum yield > 0.60. Furthermore, BODIPY resists aggregation in organic solvent and is insensitive to pH and solvent polarity.[23]

The typical BODIPY absorption profile exhibits a sharp UV band due to the S_0-S_1 transition at 500-525 nm, a hypsochromic shoulder around 480 nm indicative of vibrational conversions, and a broad band peak at 375 nm attributed to an S_0.S_2 transition.[25] The emission band is located at 530-560 nm as an S_1 to ground state transition. Due to a slow rate of intersystem crossing, phosphorescence is undetected.[23] The absorption profile can be shifted bathochromatically through modification of the BODIPY core (Fig. 7). The slightly polarized heteroatoms yield delta negative and positive reaction sites at varying positions on the internal zwitterionic core.[66] The photophysical properties are a result of the nature, number, and location of added

substituents. A number of BODIPY derivatives with red to NIR absorption profiles have been accomplished through functionalization at positions 8, 2,6- and 3,5-.

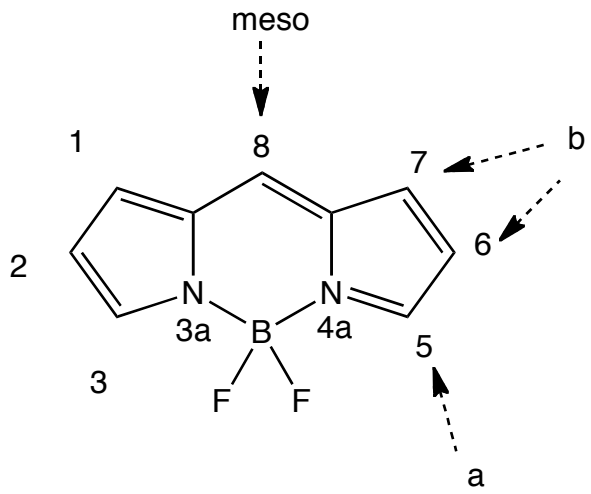


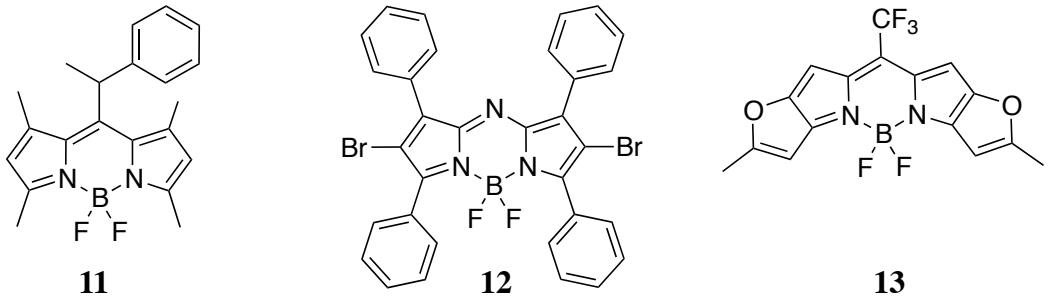
Figure 7. Structure of BODIPY core and its IUPAC numbering system.

1.8 *meso*-Functionalization of BODIPY

BODIPY core modification at the C-8 (meso) (Fig. 8) is facilitated by acid catalyzed condensation of the pyrrole unit with desired substituted acyl chlorides or aromatic aldehydes.[67] Modulation of the *meso*-position with electro-neutral substituents has shown negligible affects to absorption and emission properties.[68] A new class of BODIPY dyes termed aza-BODIPYs are the most successful BODIPY-based PDT agents to date. These derivatives, prepared by O'Shea *et al.* and functionalized by Burgess, are characterized by the exchange of the *meso*-carbon with nitrogen.[69] The substitution increases the absorption maxima of the dyes by reducing the S_0-S_1 (π-π^*) transition. The absorption and emission bands are between 650-800 nm with a high molar extinction coefficient.[25] Furthermore, the aza-BODIPY has demonstrated imaging

capability through its minor but effective fluorescence (Φ_{flu}= 0.1). However, for noninvasive imaging of deep-seated malignancies, a higher fluorescence quantum yield, therefore brightness is desired.

Direct substitution of the meso-position with an electron-withdrawing group is a hallmark of the keio-fluor (KFL) class of BODPIY based dyes. This institutes a π-donor π-acceptor mechanism, which is responsible for the observed bathochromic shift of absorbance and emission maxima. However, no therapeutic effect has been observed, and therefore KFL scaffolds are not applicable as theranostic agents.



11 **12** **13**

Figure 8. Structures of *meso*-substituted BODIPY.

1.9 2,6-BODIPY Functionalization

The 2,6- positions on the BODIPY core are prime for electrophilic substitution as these bare the least positive charge according to the mesomeric structures of the BODIPY core (Fig. 9). Electrophilic substitutions of sulfonation, halogenation, and nitration have been established by Li[70], Lee[71], and Thivierge[72] at the 2,6- positions.[73] Inclusion of sulfonate groups has shown to improve water solubility with negligible effects to photophysical properties. However, substitution by halogens and nitro groups has

significant impact on the fluorescence quantum yield. The decrease in fluorescence is a result of the heavy atom effect in respect to halogenation and photo-induced electron transfer associated with the nitration of fluorophores.[24]

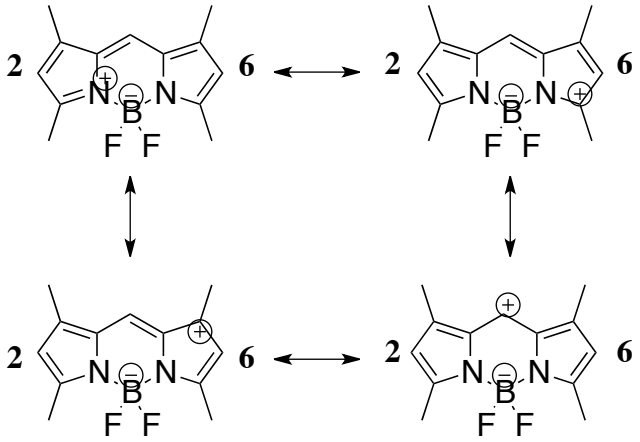


Figure 9. Resonance structures of BODIPY core illustrating the nucleophilic 2,6-position.

An alternative method of bathochromic shifting of the absorption profile involves extending the π-conjugation through palladium-mediated C-H functionalization for mono- and di- substitution products.[72] This ideology has been established for the generation of hydrophilic molecules with functional moieties enabling bio-conjugation.[70, 72]

1.0.1 3,5-BODIPY Functionalization

The acidic nature of methyl substituents at positions 3 and 5 has produced various styryl fluophores (Fig. 10). Knoevenagel condensation has afforded significant red shifts in absorption profiles.[74] This methodology offers highly functionalized BODIPY analogs

in a convenient one-step reaction. As reported by Dehaen and Boens[75], electron deficient BODIPY such as 3,5 dichloro undergo nucleophilic aromatic substitution as a means of functionalization and/or increasing the photophyscial properties (Fig. 10). Also BODIPY with 3,5-halogens are prime substrates for well-established transition metal catalyzed reactions such as Heck, Stille, Sonogashira, and Suzuki.[23, 25] The above strategies have been demonstrated in the synthesis of novel BODIPY-based fluorophores applicable as biosensors and bio-labels.

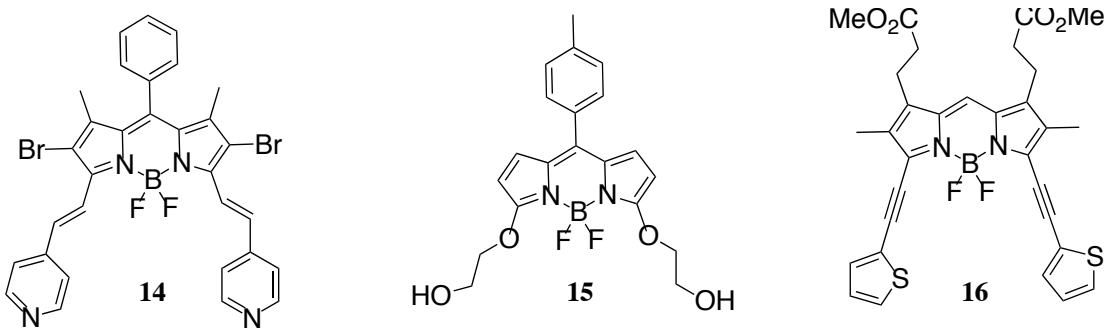
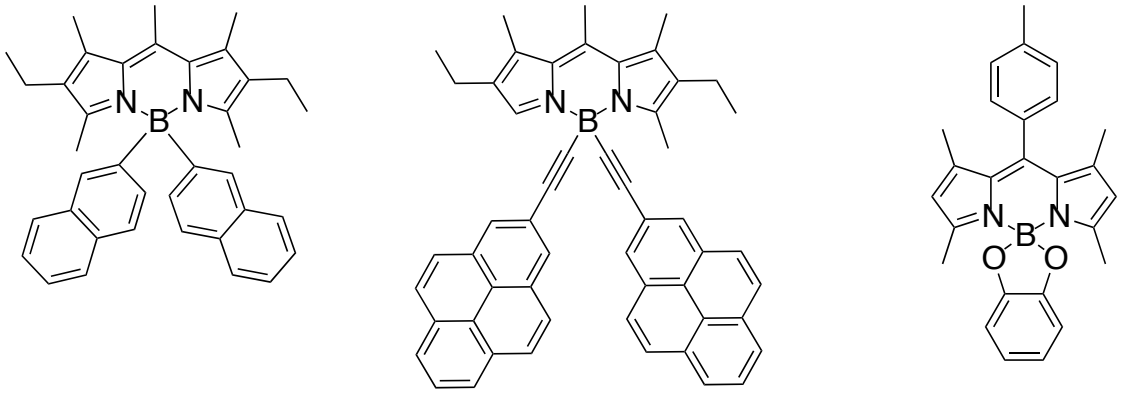


Figure 10. Chemical structures of various 3,5-substituted BODIPYs.

1.0.2 Modification of Boron Center

Substitution of the boron center is advantageous for circumventing problems of parent BODIPY i.e. small stokes shifts and fluorescence quenching. Replacement by aryl, ethynyl and alkoxide groups provide a class of highly fluorescent dyes identified by their substitution moieties as C-BODIPYs, E-BODIPYs, and O-BODIPYS[76], respectively (Fig. 11). The appendage of one or more polycycles to the boron center provides multiple light absorbing units to partner with the energy acceptor of the BODIPY nucleus. Ziessel *et al.* have investigated the rapid energy transfer between the two fluorphores and have cited significant overlap of the donor polycycle emission and acceptor BODIPY absorption.[24] In addition, the impact on photophysical properties by

the ethynyl substituents were negligible. The dyes below are being explored as energy transfer cassettes and electroluminescent devices.

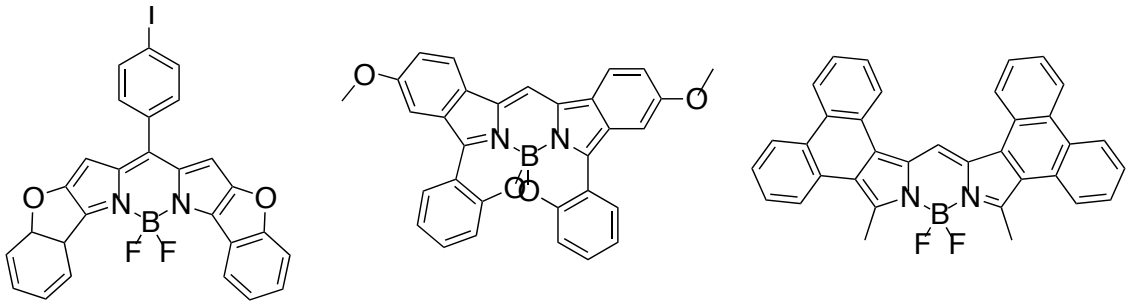


17 **18** **19**

Figure 11. Chemical structures of various boron substituted BODIPYs.

1.0.3 Extended Conjugation Through Rigid Ring Fusion

The generation of long emission BODIPY dyes has been accomplished through ring fusion. The enhancement in emission derives from restricted bond rotation and steric hindrance. Ring annulation at the β,β'-position has surfaced as a solid strategy for generating BODIPY fused phenanthrene, spiro-fuorene moieties, and benzene from aryl fused-pyrroles and 2-acetyl-phenols as shown in figure 12.[77]



20 **21** **22**

Figure 12. Chemical structures of rigid BODIPYs.

1.0.4 Biological Application of BODIPY Fluorophores

Fluorophores conjugated to biomolecules i.e. proteins and peptides serve to elucidate various molecular pathways as these conjugates act as reporters of biological systems.[78] The compatibility of fluorophores with various bio-analytical and optical imaging techniques such as DNA sequencing, gel electrophoresis, *in vivo* imaging, vascular mapping, and nucleic acid detection allow characterization of subject biomolecules within intact tissue.

As briefly mentioned in Chapter I, the emphasis on developing fluorophores with near infrared absorption and emission profiles revolves around the endogenous absorption and scattering of UV/visible light. Specifically water, lipids, oxyhemoglobin, deoxyhemoglobin and other biomolecules absorb UV and visible light, which hampers tissue penetration. UV illumination of these embedded molecules yield tissue autofluorescence and thus a low contrast between biological targets and surrounding tissue. Low energy near infrared light allows deeper penetration as the tissue extinction coefficient is significantly lower. Therefore, a significant increase in target-to-tissue is ratio established (Fig. 13).[79]

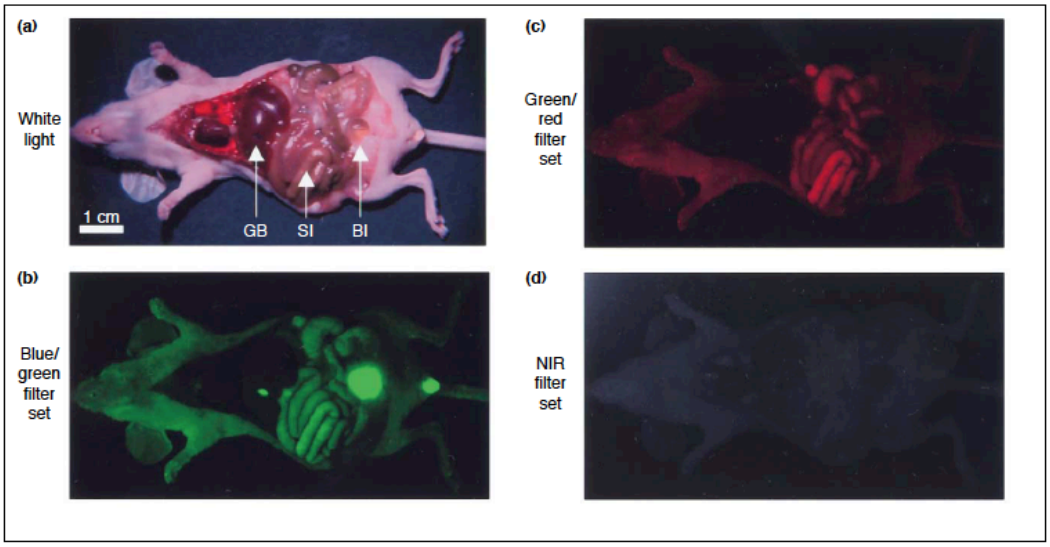


Figure 13. Autofluorescence of tissue in response to various excitation/emission filters; (GB:gall bladder, SI: small intestines, BI: bladder).[57] Reprinted with permission from [51] Copyright (2003) Elsevier.

As BODIPY dyes have excellent photophysical properties, translation of these attributes biologically has proven to be advantageous. The semi-porphryin scaffold has been applied as a biological label, reporter of enzymatic activity, sensor for metals ions and protons, and stain for subcellular localization[22] (Fig. 14).

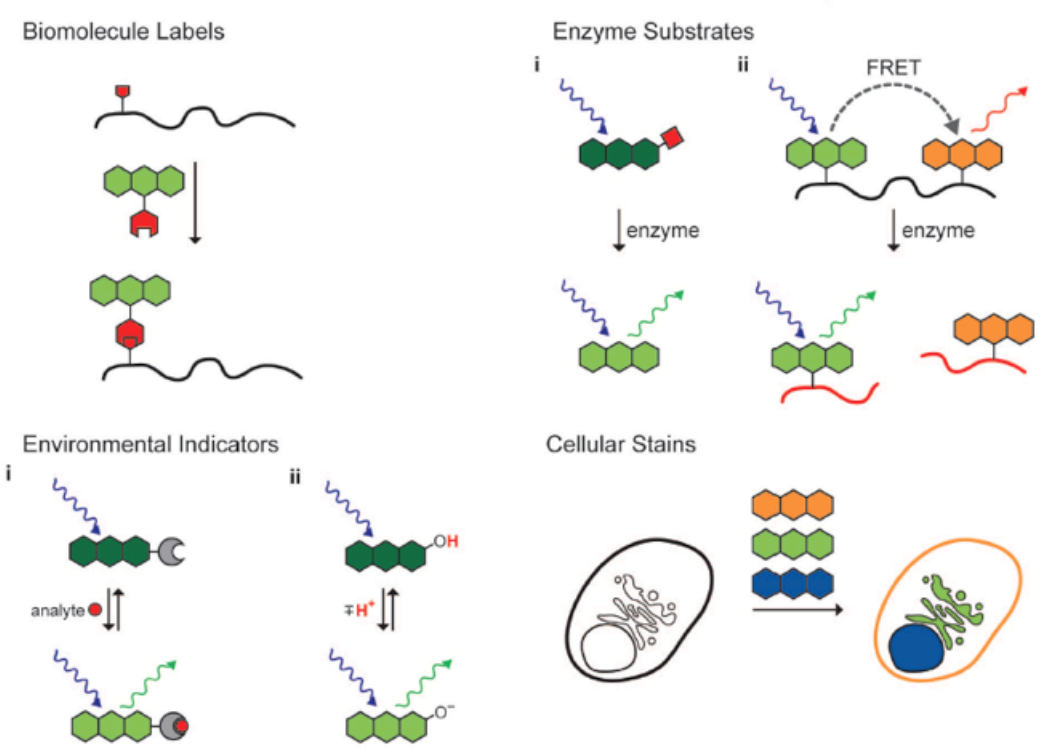


Figure 14. Illustration of BODIPY biological application. Reprinted with permission from [29]. Copyright (2008) American Chemical Society.

1.0.5 Biological Labels

In effort to comprehend the evolution and innovate treatment of disease, there has been an increased demand for substrates and tools to investigate bio-molecular interactions. As organisms do not emit a specific signal, fluorophore labeled biomolecules serve as unique and powerful tools for addressing this need. For example, biomolecules have been successfully tagged with fluorophores for intracellular and whole body imaging. However, this technique is limited to the efficacy of available fluorophores.

BODIPY dyes are prime candidates as biological labels due to high fluorescent quantum yield, large absorption coefficient, and minimal dark toxicity. The reactivity

within the BODIPY structure enables facile conjugation of biological ligands such as nucleotides, amino acids, lipids, and proteins. In general BODIPY-biomolecule conjugates are facilitated by conversion of terminal carboxylic acids to reactive motifs such as succinimdyl esters, maleimides, and bioorthoginal reaction partners (Fig. 15).

Tethering of functionalized BODIPY to target specific ligands such as antibodies serves to visualize drug bio-distribution and detect receptor interactions. In addition, biomolecule conjugation can be accomplished with negligible effects to natural function due to small size of BODIPY.

Many UV absorbing BODIPY based fluorophores are being used for live cell imaging. With the assistance of two-photon imaging, BODIPY based probes have been successful at imaging deeper intact-tissue.[80] *In vivo* cellular labeling of sugars and amino acids has been reported utilizing copper free and copper facilitated click chemistry. BODIPY modified alkyne based probes were designed as non-perturbing "bio-orthogonal reporters" applied for labeling of azide modified surface glycans of CHO cells.[81]

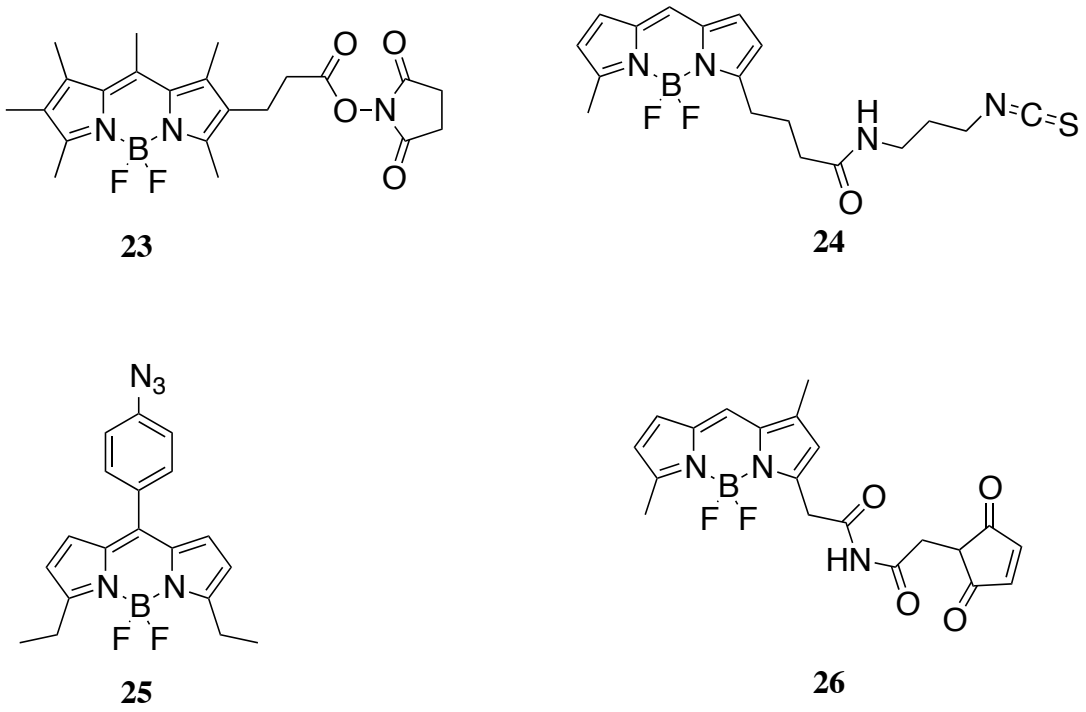


Figure 15. Structures of BODIPY with reactive functional groups**.**

1.0.6 Enzyme Substrates

Fluorometric assays are traditionally used to detect and analyze enzymatic activity. Assays measure the fluorescence difference between the fluorophore substrate and product for analyses of various enzymes.[82] The ability to identify and understand such activity is vital to quantify enzymatic activity *ex vivo*. Conventional fluorophore assays of fluorescein and hemoglobin are often inconclusive due to the minute difference between substrate and product fluorescence.[83] The optical properties of BODIPY are advantageous for enhancing analysis efficiency. Protease assays have employed the principle of Fluorescence Resonance Energy Transfer (FRET) for reducing proteins ability to fluoresce through self-quenching.[84] Conjugation of multiple BODIPY

fluorophores to proteins causes this reduction and upon hydrolyses the protein is able to fluoresce proportional to biological activity.[85]

1.0.7 Environmental Indicators

The tissue microenvironment provides a rich source of potential biomarkers such as pH and metal ions, which are indicative of disease onset. Design and synthesis of fluorescent sensors detecting deviation from regulatory levels have gained considerable interest over the past decade. These sensors arise from principles of Photoinduced electron and Internal Charge Transfer (PeT and ICT) incorporated into fluorophore spacer receptor constructs. The receptor binds to an analyte causing a shift in fluorescence or wavelength absorption. In either applied principle, fluorescence emission is essentially reduced or shutoff preceding analyte binding.[23] In the case of PeT, no spectral change is observed, however ICT is accompanied with significant spectral shifts. BODIPY-based sensors have been developed with inherent PeT and ICT. The sensors have been developed for monitoring imbalance in pH[86], Zn^{2+}[87], Hg^{2+} Ni^{2+}[88], K^{+}[89], Cu^{2+} levels (Fig. 16).[90]

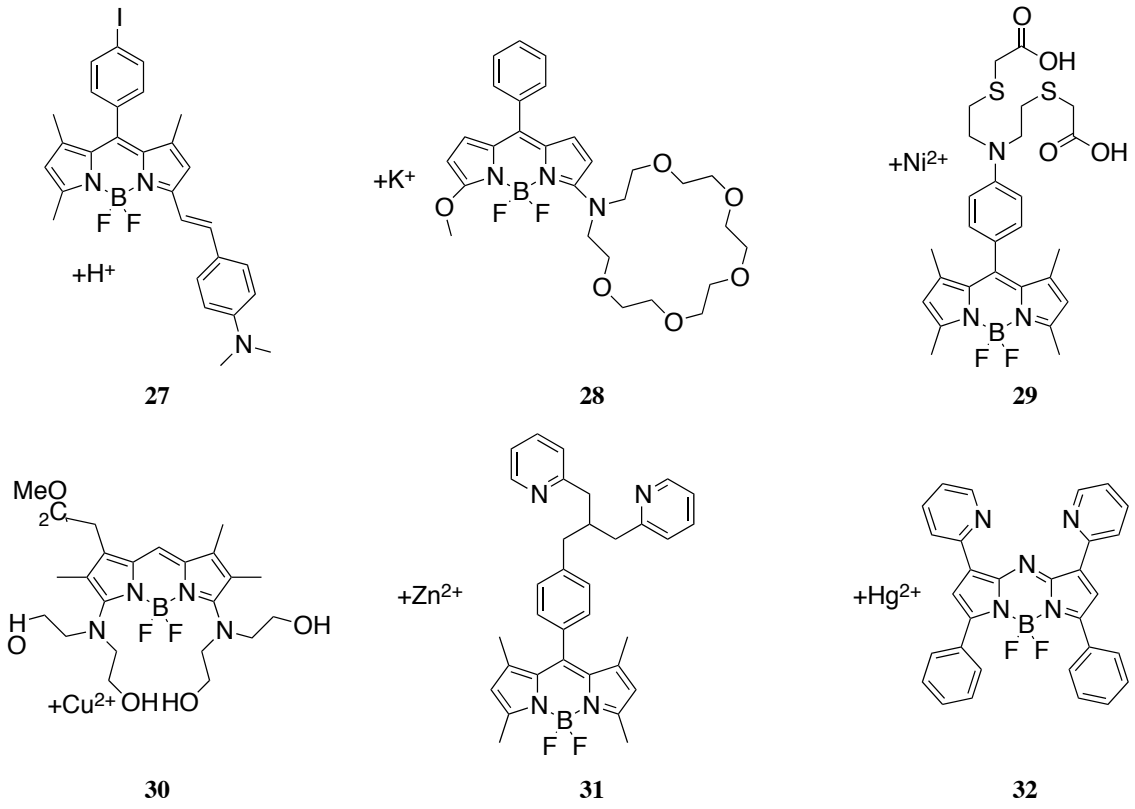
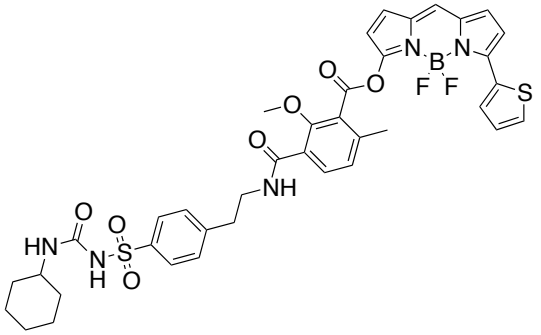


Figure 16. Chemical structure of BODIPY dyes applied as bio-sensors.

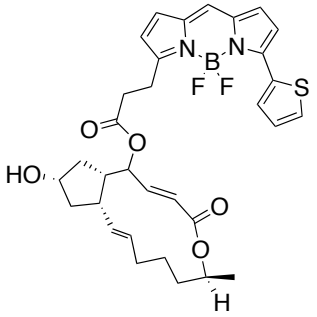
1.0.8 Cellular Stains

Visualization of intracellular components is difficult due to their transparent nature. Thus investigation of the cell's organelles through staining provides a visual aid for characterizing cellular morphology and function.[91] BODIPY dyes applied for organelle staining is well established in the pre-clinical setting as their small size and appropriate amphilicity facilitate permeation and retention within cellular compartments, respectively.[92] BODIPY dyes such as BODIPY TR-glibenclamide and BODIPY ceramide effectively stain the endoplasmic reticulum and Golgi apparatus accordingly. BODIPY conjugates, namely BODIPY FL-ceramide, BODIPY FL C_5 –sphingomyelin, and BODIPY brefeldin A, have been developed with varying emission wavelengths for

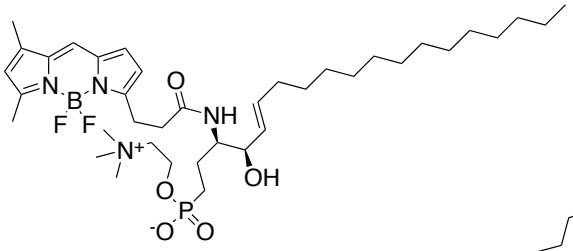
live cell imaging and flow cytometry (Fig. 17).[93] Overall the intracellular localization is not ffected due to the low molecular weight of BODIPY.



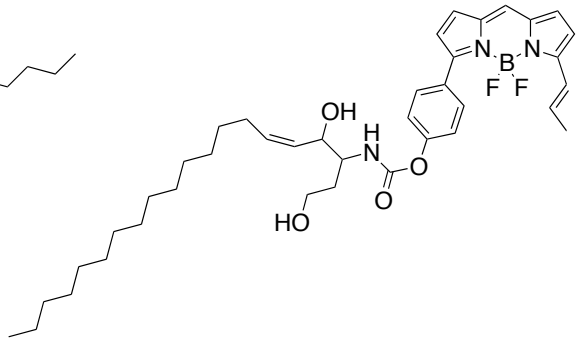
BODIPY-TR-glibenclamide



BODIPY- brefeldin A



BODIPY-FL C_5- Sphingomyelin



BODIPY TR-ceramide

Figure 17. Fluorescent BODIPY probes for endoplasmic reticulum and golgi apparatus labeling.

Chapter II. Design, Synthesis, and Mechanistic Investigation of NIR Dual Functioning BODIPY PS

1.0 Introduction

Photodynamic therapy's stagnant application as a primary treatment modality stems from a lack of photosensitizer development. Since the worldwide approval of Photofrin, many disadvantages and guidelines for improvements in therapeutic efficacy have surfaced. For example, Photofrin absorbs red light at approximately 630 nm, which does not allow tissue penetration beyond a few millimeters. At the above wavelength, the molar absorptivity (3,000 M^{-1} cm^{-1}) is low, which necessitates extended and intense light dosage. These less than optimal properties limit Photofrin mediated PDT application to superficial tumors or those accessible by endoscope. Extended and intense light dosages along with slow clearance from skin post treatment causes skin photosensitivity. Hence, the design of novel photosensitizers has been focused toward improving Photofrin's shortcomings with the following guidelines: (1) minimal toxicity absent illumination (i.e. no toxic effect without interaction with light) (2) absorption within the biological window, (3) chemical purity, (4) high brightness for imaging, (5) high phototoxic power for therapy, and (6) appropriate lipophilic/hydrophobic balance for selective accumulation or possess functional groups for targeting. Many second-generation photosensitizers have since been approved as their design seeks to follow the set guidelines. However, none satisfy all criteria (Table 2). Most approved PSs are of the tetrapyrole structure and are limited in terms synthetic modification and brightness (Fig. 18).

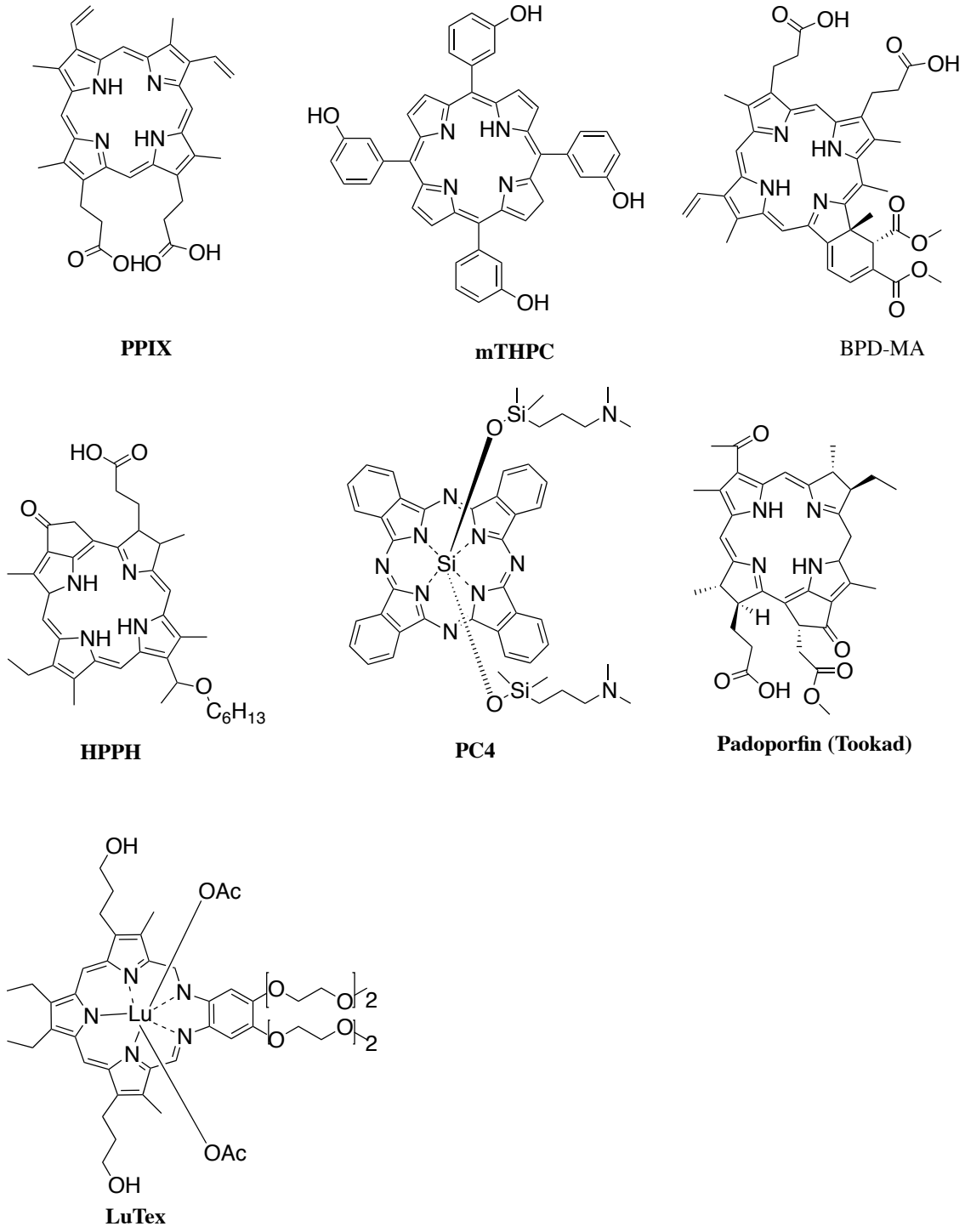
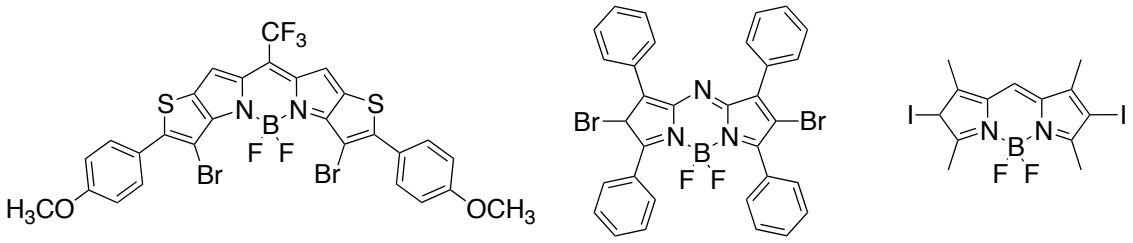


Figure 18. Structure and photophysical characteristics of clinically approved late stage clinical PSs.

Table 2. Optical properties of select 2nd generation PS.

2nd Generation PSs	λ_{abs} nm	ε $M^{-1}cm^{-1}$	Φ_{flu}	Φ_{Δ}	BT $M^{-1}cm^{-1}$	PP $M^{-1}cm^{-1}$
PpIX[50a, 94a]	635	~5000	0.16[b]	0.56	800	2,800
mTHPC[95b]	650	29,600	0.09	0.43	2,664	12,728
HPPH[96c]	638	45,000	0.43	0.48	19,350	21,600
BDP-MA[97b]	686	34,000	0.05	0.76	1,700	25,840
Pc 4[98d]	680	230,000	0.38[e]	0.43	87,400	98,900

As a result of increasing cancer targets being subjected to PDT, new classes of PSs are needed to address the deficiencies of porphyrin scaffolds. BODIPY (4,4-difluoro-4-bora-3a, 4a-diaza-s-indacene) dyes are attractive as PSs due to their unique optical properties, in particular they possess high molar extinction coefficients and fluorescence quantum yields (Brightness).[23] Singlet oxygen generation is atypical of BODIPY dyes due to ineffective intersystem crossing. However, BODIPY dyes can be converted to photosensitizers through incorporation of heavy atoms. This phenomenon, known as the heavy atom effect, increases spin orbit coupling and thereby facilitates intersystem crossing and ultimately singlet oxygen generation.[99] O'Shea *et al*. incorporated heavy atoms into the BODIPY core of tetraarylazadipyrromethanes (aza-BDP) to yield a singlet oxygen quantum yield of 0.74.[99a, 99b, 100] However, further reports highlight that inclusion of heavy atoms results in cytotoxicity in the absence of light and compromises (i.e. shuts off) fluorescence yields due to increased intersystem crossing efficiency[101] (Fig. 19). Thus, fluorescent BODIPY PSs without heavy atoms are preferred for efficient imaging and therapy applications.



33 **34** **35**

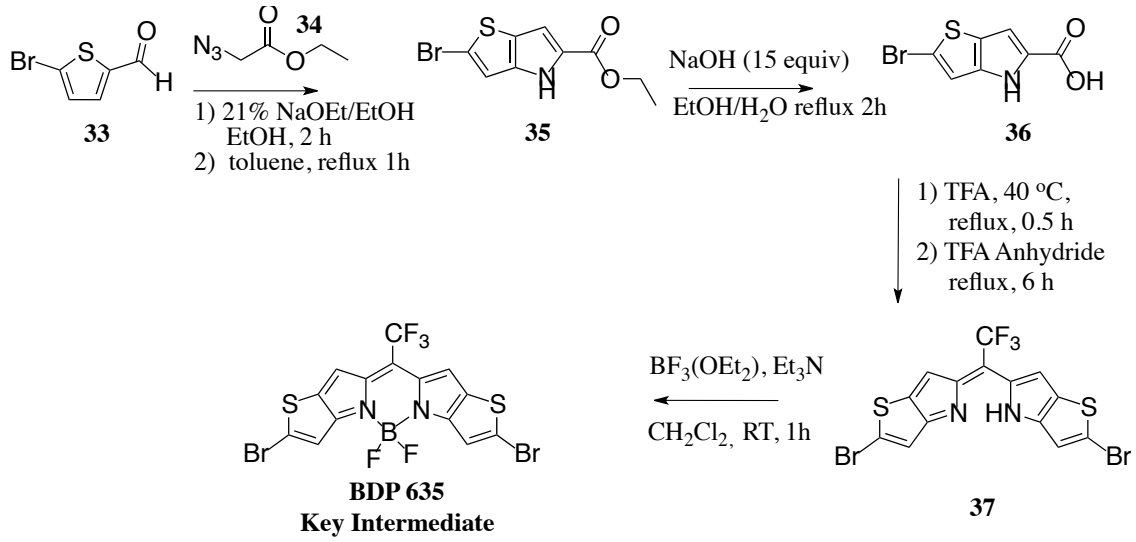
Figure 19. BODIPY PSs through incorporation of heavy atom halogens.

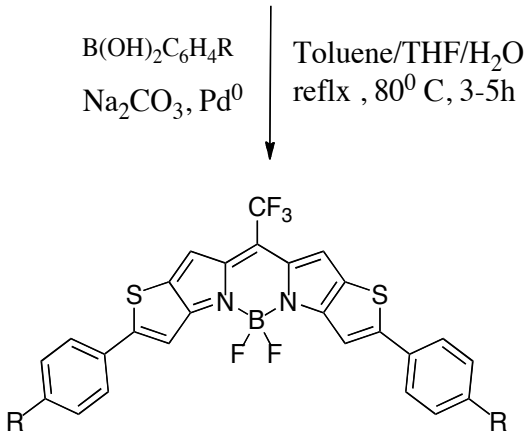
This chapter reports our research work to develop an unprecedented case of BODIPY PSs without heavy atom halogen assistance. In the search for NIR BODIPY dyes, we discovered that SBDPiR690 possesses inherent and advantageous photophysical properties of singlet oxygen generation ($\Phi_{\Delta} = 0.42$) and fluorescence quantum yield ($\Phi_{flu} = 0.22$). The rare coexistence of these photophysical properties in conjunction with a high extinction coefficient (120,000 $M^{-1} cm^{-1}$) afforded appreciable BT, 26,400 $M^{-1}cm^{-1}$, and PP, 50,400 $M^{-1}cm^{-1}$ and indicated this mono-chromophore's potential as a dual functioning fPS for theranostics.

The innate ability of **SBDPiR690** to intersystem cross allows the use of BODIPY's full compendium of photophysical properties for combined imaging and therapy. Drawing inspiration from this rare phenomenon within the BODIPY scaffold, we set out to identify the structural contribution for inducing intersystem crossing. Herein, the peripheral substituent affects on photophysical properties were analyzed to establish a BODIPY structure-photophysical property relationship – in particular, we validate the key factor for SO generation of these non-heavy atom-assisted BODIPY PSs through transient absorption spectra.

2.1 Design and Synthesis of NIR Dual Functioning NIR BODIPY Analogs

The design of the novel compounds, **SBDPiR688**, **SBDPiR698**, **SBDPiR700** and **SBDPiR710**, was principled upon the serendipitous discovery of singlet oxygen generation by non-halogenated **SBDPiR690**. A structure photophysical property investigation reveal analogs possessing oxygen at the peripheral sites are incapable of producing singlet oxygen (Table 3). This finding is attributed to the strong donating character of the atom. Therefore, agents were designed to incorporate substituents with modulated electron donating groups at the peripheral positions as in **SBDPiR710** and increasing degrees of electron withdrawing groups: **SBDPiR698 < SBDPiR688 < SBDPiR700**.





SBDPiR688 R= CF_3 28%
SBDPiR698 R= F 32%
SBDPiR710 R= CH_3 43%
SBDPIR700 R= CN 37%
SBDPiR690 R= H 60%
SBDPiR731 R= OMe 50%
SBDPiR740 R= OH 54%

Scheme 1. Synthesis of **NIR BODIPY PS.**

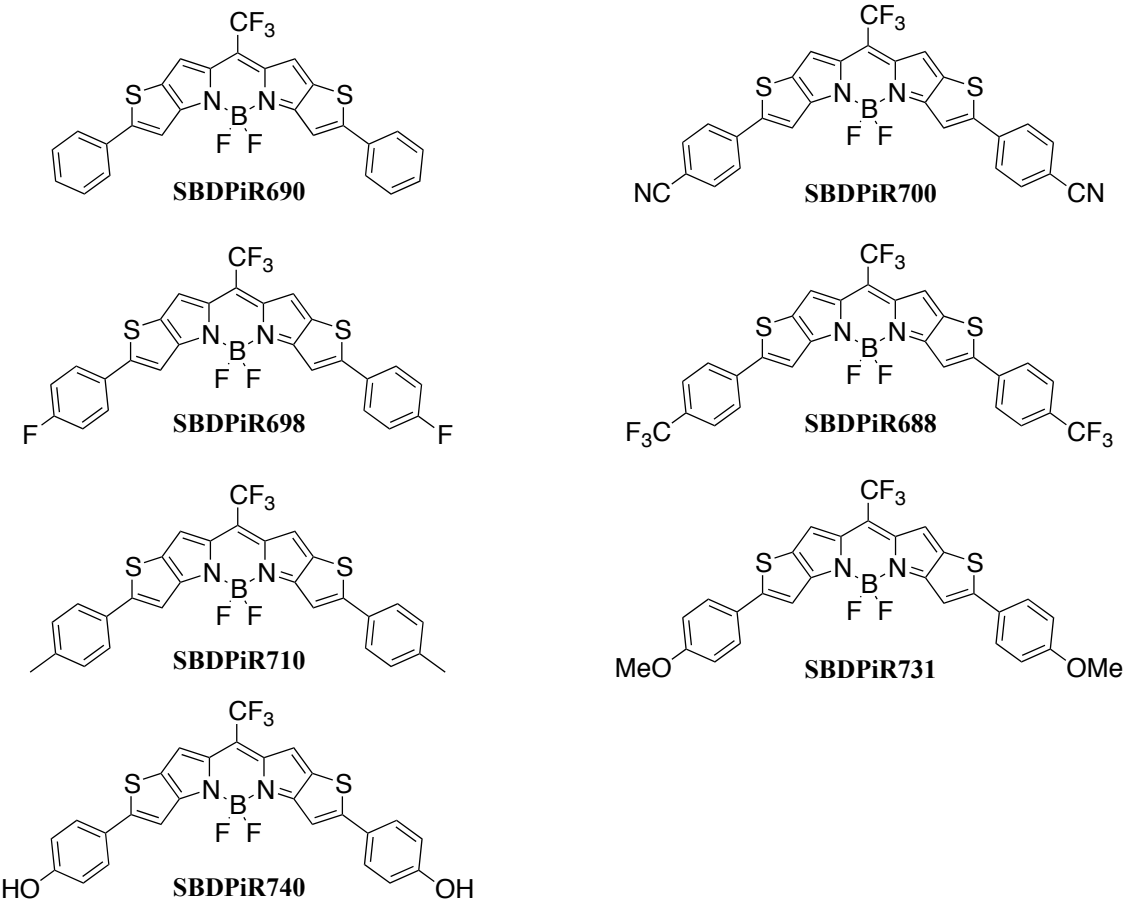


Figure 20. Structure of thiophene fused BODIPY Infrared absorption maxima (SBDPiRxxx).

2.2 RESULTS AND DISCUSSION

The starting point of our synthesis was the reaction of commercially available bromothiophene carboxyaldehyde **33** and ethyl azido acetate **34** in the presence of 21% sodium ethoxide to promote an aldol dehydration reaction (Scheme 1).[102] The intermediate, (Z)-ethyl 2-azido-3-(5-bromothiophen-2-yl)acrylate, was not characterized, but dissolved in toluene at 100° C for 1 h to yield the five membered cyclized product **35**. Hydrolysis of the **35** by 15 equivalents of sodium hydroxide afforded **36** in high yields. These conventional synthetic reactions provide the building blocks to an invaluable thieno-pyrrole-fused key intermediate **BDP635.** This intermediate was recently established as an efficient platform for developing NIR multifunctional agents.[102] The red emitting dye was synthesized through a one-pot TFA mediated decarboxylation of **36** at 45° C followed by condensation of TFA anhydride to obtain the CF_3 *meso*-substituted dipyromethane unit. Chelation of dipyromethane with boron trifluoride followed by purification via flash chromatography yields the **BDP635** with a yield of 16%.[102] The conjugated-π framework and peripheral bromines give rise to a powerful electrophile that is ideal for Suzuki-Miyaura coupling reactions.

Compounds **BDP635**, **SBDPiR690**, **SBDPiR731**, and **SBDPiR740** were synthesized in a previous study [*Chemistry An Asian Journal* **2013**, 8,3123-3132] and repeated for control studies. The novel compounds, **SBDPiR688, SBDPiR698, SBDPiR700** and **SBDPiR710**, were synthesized according to Scheme 1. In an one-pot reaction, **BDP635** and the respective commercially available aryl-boronic acid were dissolved in a biphasic mixture under reflux 80° C to achieve the reported analogs. The reaction times

and yields varied between 2-4 hours and 60-32% respectively. This is a direct *para* – substituent effect as electron-withdrawing groups deactivate the phenyl ring of the aryl boronic acids. Reaction completion was judged by a distinct color change as extending the conjugation bathochromatically shifts the emission. This proved advantageous for synthesizing electron-withdrawing analogs. The compounds were purified via column chromatography on silica gel prior to spectroscopic and biological analysis. Suzuki coupling hallmarks of easily separated inorganic starting material and bi-products are evident with the pure ^{1}H NMRs. We further characterized each analog through high-resolution mass spectrometry.

2.3 X-ray structural analysis of SBDPiR690

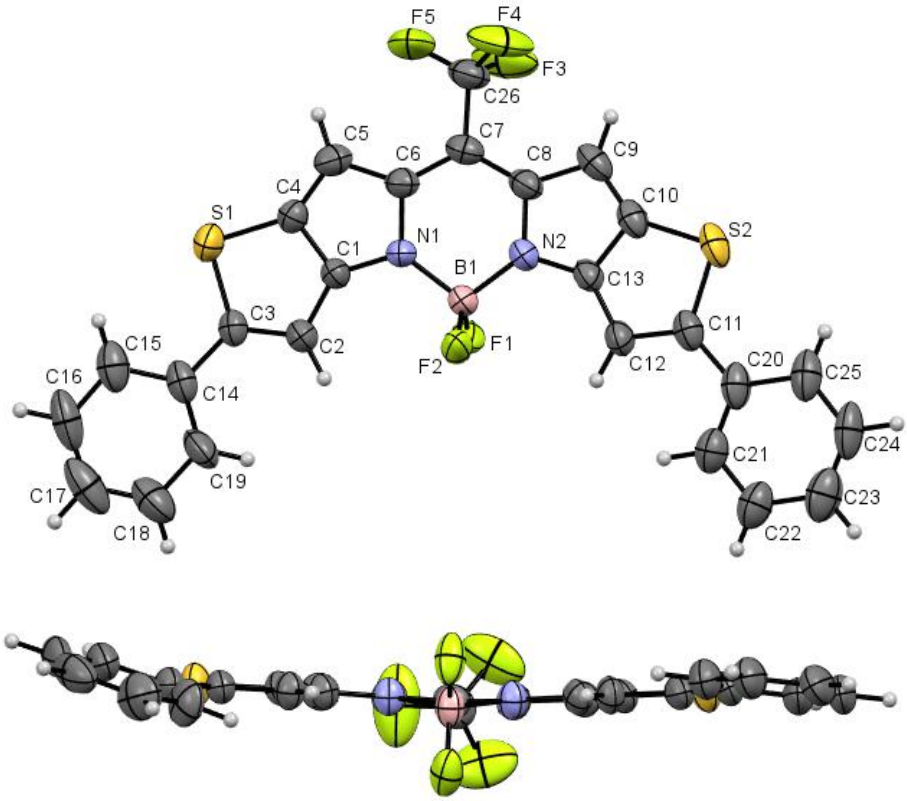


Figure 21. ORTEP view of the X-ray crystal structures of SBDPiR690.

Displacement ellipsoids are drawn at the 50% probability level.

The X-ray crystal structure was obtained at the University of North Texas. The X-ray crystal structure of SBDPiR690 confirmed its structural similarities with that of dibromo-intermediate (BDP635)[102]. The molecule crystallized in the monoclinic crystal system with space group P21/c. The five core fused rings were almost planar (Fig. 21). The conjugated nature of the middle ring was confirmed by the comparable bond lengths of between C7-C6 (1.396 Å) and C7-C8 (1.393 Å); between C6-N1 (1.398 Å) and C8-N2 (1.392 Å); and between N1-B1 (1.509 Å) and N2-B1 (1.526 Å). The boron center also maintains tetrahedral geometry with an N1-B1-N2 angle of 105.7° and an F-B-F angle of 108.5°. Two phenyl groups, although rotatable in a solution, were also close to the same plane with the main core. The dihedral angles of S1-C3-C14-C15 and S2-C11-C20-C25 were 11.6° and 15.4°, respectively.

2.4 Optical Properties

The absorption and emission spectroscopic data are presented in Table 3. The **SBDPiRs** exhibited the signature sharp absorption characteristic of BODIPY dyes indicative of the $S_0 - S_1$ transition (Fig. 22). The varying substituents impacted the absorption and emission maxima. **SBDPiR**s with electron donating groups (CH_3, OMe, OH) have red-shifted maxima compared to **SBDPiR**s with electron withdrawing groups (F and CF_3) – λ_{abs} = 688, 698 vs. 709 ~ 738 and λ_{flu} = 695, 705 vs. 712 – 763. The bathochromic shifts by electron donating groups was evident – 21 ~ 50 nm shift in λabs of and 12 ~ 63 nm shift in λ_{flu} from those of **BDPiR690**. It is perhaps due to a better push/pull

system between pull group (CF_3) at the meso position and push group (OH, OCH_3, and CH_3 groups) at the *para*-position of the phenyl groups[23]. In addition, this correlation was manifested in the Stokes shift. **SBDPiR688** absorbance to emission shift was relatively small (7 nm), while that of **SBDPiR740** was 25 nm (Fig. 23).

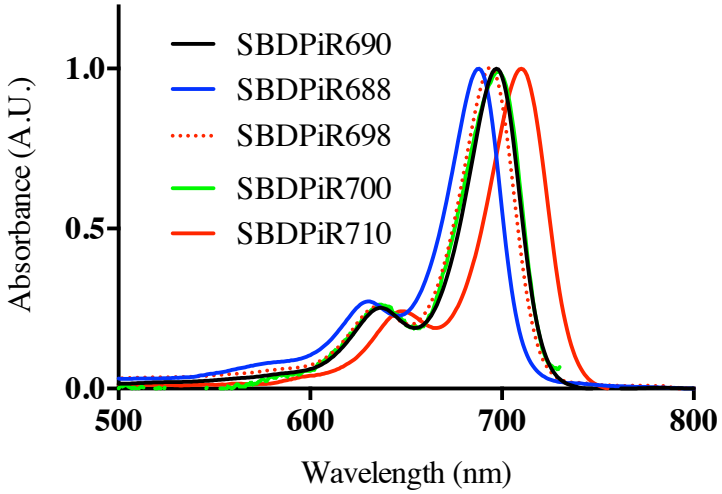


Figure 22. Absorbance spectra of SBDPiRs

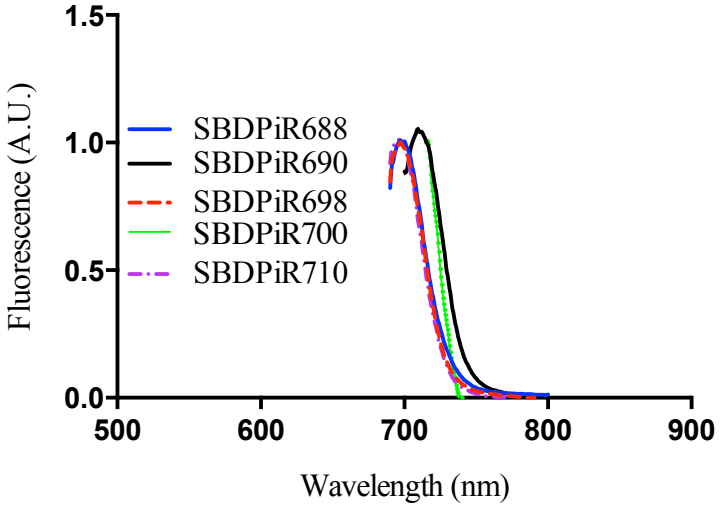


Figure 23. Fluorescence spectra of SBDPiR

Singlet oxygen quantum yield is defined as the ratio of molecules of singlet oxygen generated over photons absorbed. The value was determined by measuring the phosphorescence of singlet oxygen after the excitation of BODIPYs[102] The electronic properties of the para-substituents demonstrated positive and negative effects in respect to SO generation. While SBDPiRs with electron donating groups (CH_3, OH, and OMe) did not show any detectable Φ_Δ, SBDPiRs with electronic withdrawing groups (F and CF_3) exhibited moderate Φ_Δ (0.20 and 0.47).

Table 3. **Photophysical characteristics of SBDPiRs**

Compound	R	λ_{abs} [nm]	λ_{flu} [nm]	$\varepsilon^{[a]}$ [M^{-1} cm^{-1}]	$\Phi_{flu}^{[b]}$	$\Phi_{\Delta}^{[c]}$	$BT^{[e]}$ [M^{-1} cm^{-1}]	$PP^{[f]}$ [M^{-1} cm^{-1}]
SBDPiR690	H	688	700	120,000	0.22	0.42	26,400	50,400
SBDPiR688	CF_3	688	695	211,000	0.39	0.47	82,290	99,170
SBDPiR698	F	698	705	146,000	0.38	0.20	55,480	29,200
SBDPiR700	CN	700	715	146,251	-	-	-	-
SBDPiR710	CH_3	709	712	287,000	0.67	ND	192,290	ND
SBDPiR731	OCH_3	731	755	185,000	0.38	ND	70,300	ND
SBDPiR740	OH	738	763	160,000	0.10	ND	16,000	ND

[a] Molar absorptivity measurements were carried out in $CHCl_3$ except BDP740-OH performed in EtOH. [b] The fluorescence quantum yield was determined in $CHCl_3$ (MeOH for BDP740-OH) at 298 K with Aza BODIPY $\Phi_{flu} = 0.34$. [b] Quantum yields determined in $CHCl_3$ at 298 K with KFL-4 as reference. [c] SO quantum yield was determined in $CHCl_3$ with $[Ru(bipy)_3]Cl_2$ as a reference ($\Phi_\Delta = 0.77$ in MeOH). [d] Not determined under our experimental conditions. ND: Not Detected. [e] Brightness (= ε ×

Φ_{flu}) [f] Phototoxic Power (= ε × Φ_{Δ}) [f] $\boldsymbol{\Phi_{flu}}$ for SBDPiR688, -698 is 0.39 and 0.38 with respect to $ADPBBF_2$ (0.34).

In comparison to Φ_{flu} and Φ_{Δ}, BT and PP are better parameters for judging fluorescence imaging and PDT capability as these consider the extinction coefficient of PSs: BT = ε × Φ_{flu} and PP = ε × Φ_{Δ} [102]. Light harvesting is critical in particular for *in vivo* conditions where the excitation light is extremely limited due to the light attenuation by tissues. The BT and PP of electron withdrawing analogs SBDPiR690, 688, and 698 were higher than those all second generation PSs in Fig. 1 except Pc 4. These optical characteristics are good indicators of the potential as dual functioning fPSs. SBDPiR688 showed excellent BT and PP comparable to those of Pc 4.

2.5 DPBF Method for Detection of Singlet Oxygen

The analogs present were investigated for singlet oxygen generation. Tetrahydrofuran (THF) solutions of the novel **SBDiRs** were irradiated with broadband light, 400-850 nm, at 0.5 mW/cm^2. Singlet oxygen generation was approximated experimentally through the oxidation of 1,3-diphenylisobenzofuran (DPBF), a known singlet oxygen scavenger. The presence of reactive oxygen species such as singlet oxygen causes an evident decrease in the DPBF absorbance band at 410 nm. The initial concentrations were 5 x 10^{-6} M of **SBDPiR** and 90 x 10^{-6} M of DPBF over a period of 16 min. **SBDPiR690** was shown in our previous study to have a high singlet oxygen quantum yield (O_{Δ}) of 0.42, and therefore was used as positive control (Fig. 24).

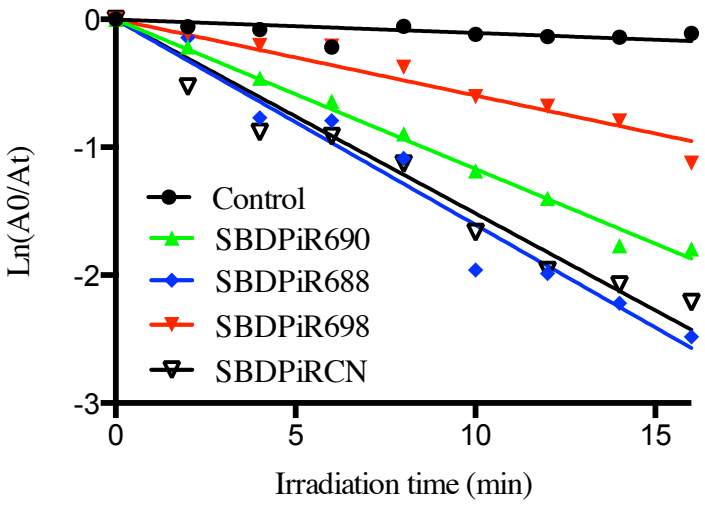


Figure 24. Time-dependent decrease of absorbance (410 nm) by oxidation of DPBF (90 x 10^{-6} M) with SBDPiR (5 x 10^{-6} M) under broadband light (400-850 nm at 0.5 mW/cm^2).

While **SBDPiR710** rate of DPBF oxygenation is subtle at 0.5 fold, analogs **SBDPiR688, SBDPiR700,** and **SBDPiR698** demonstrate folds of 1.0, 2.0, and 2.5 respectively. The less significant rate associated with **SBDPiR710** is due hypothetically to the persistent electron donating effect of the -CH_3 substituent. Again, this trend was visualized in our initial study, as $^1O_2$ for **SBDPiR731** and -**740** were negative. Further validation was obtained by the phosphorescence spectra of $^1O_2$ at 1270 nm. The intensity of the respective 1270 nm peaks align with the DPBF data illustrating **SBDPiR688** > **SBDPiR698** in respect to singlet oxygen generation efficiency. **SBDPiR710** was not detected in the spectrum, indicating no singlet oxygen generation. Noteworthy is the relatively high fluorescence quantum yield (Φ_{flu}) ~ 0.77 for both singlet oxygen generating analogs. This demonstrates their ability to transition between

both S_1 to S_0 and S_1 to T. These coexisting optical characteristics are of primary importance for developing theranostic agents.

2.6 Electrochemical Potential.

The redox potentials of all SBDPiRs were determined by Dr. Francis D'souza at the University of North Texas. The electrochemical potentials were measured in CH_2Cl_2 containing 0.1 M TBAP with Ag/AgCl as a reference electrode and ferrocence/ferrocinium (Fc/Fc^+) as an internal redox standard (Table 4). Excluding **SBDPiR740**, all **SBDPiRs** underwent two completely reversible redox potentials forming the respective stable anion(s) and cation(s)[102]. Cyclic voltammograms of the new analogs showed the oxidation potential range from $E_{1/2}$ = 0.78 to 1.22 V and the reduction potentials between $E_{1/2}$ = -0.76 to -1.51 V.

In our initial study[102], we discovered a natural relationship between the energy gap of first oxidation and reduction potentials with Φ_Δ. BDP635 (dibrominated intermediate) and SBDPiR 690 had the largest energy gaps between the redox potentials, 1.77 and 1.72 V. These two exemplify appreciable SO generation ($\Phi_\Delta > 0.2$) among 12 analogs. The energy gaps of the remaining analogs were smaller, ranging from 1.57 to 0.92 V. Interestingly enough, the large energy gap, 1.58 and 1.70 V, is persistent in the two new analogs (SBDPiRs 688 and 698) containing electron-withdrawing groups.

2.7 Mapping of HOMO-LUMO Energy Levels

We estimated the HOMO and LUMO energy levels of the two groups of BODPY analogs – with electron withdrawing groups (SBDPiR688 and 698) or electron donating groups (SBDPiR710, 731, 740) – from their first oxidation and reduction potentials (Table 4), mapped in the graph (Fig. 22). The standard method equation $E_{HOMO/LUMO}$= (-4.78 + ($E^{1/2}_{ref\ vs.\ Ag/Ag+}$ (–$E^{1/2}_{OX/RED\ vs.\ Ag/Ag+}$) was used to calculate the energy levels where -$E^{1/2}_{ref}$ = is the half potential of ferrocene vs Ag/Ag^{+}.[103] The HOMO energy levels of the analogs with electron donating groups decreased by -0.10, -0.19, and -0.23 eV while the decrease of the analogs with electron withdrawing groups was much smaller, by -0.01 and -0.15 eV, compared to the HOMO energy level of SBDPiR690. The HOMO-LUMO energy gaps of SBDPiRs with electron withdrawing groups also were larger, 1.70 and 1.66 eV, than those of SBDPiRs with electron donating groups, 1.34 ~ 1.53 eV.

The relation between the HOMO-LUMO energy gap and Φ_{Δ} of all BODIPY analogs (including analogs in our previous reference[102] we have prepared) was plotted (Fig. 25). Even though we could not identify a single equation covering the relationship for all the compounds in our previous study and current works, there was a noticeable trend. It appears > ~1.5 eV of HOMO-LUMO gap is necessary for our BODIPY analogs to exhibit appreciable SO generation (Φ_{Δ} > ~0.2). This trend alone does not suffice for the observed SO generation: there were two analogs with > 1.5 eV gaps but without SO generation.[102]

Table 4. Summary of Redox Potentials.

Compound	R	$E^{1/2}$(ox)[a] (CV) [V]	$E^{1/2}$(red)[a] (CV) [V]	HOMO[b] (CV) [eV]	LUMO[b] (CV) [eV]	E_{gap}[c] (CV) [eV]
SBDPiR690	H	0.79	-0.93	-5.17	-3.45	-1.72
SBDPiR688	CF_3	0.94	-0.76	-5.32	-3.62	-1.70
SBDPiR698	F	0.78	-0.80	-5.16	-3.50	-1.66
SBDPiR700	CN	-	-	-	-	-
SBDPiR710	CH_3	0.69	-0.84	-5.07	-3.54	-1.53
SBDPiR731	OCH_3	0.98	-0.45	-5.36	-3.93	-1.43
SBDPiR740	OH	1.02	-0.32	-5.40	-4.06	-1.34

[a] Half potentials of first oxidation and reductions

$E_{HOMO(Fc)}$= -4.78 eV

$E^{1/2}{}_{ox}$(Fc)= 0.40[104]

[b] E_{HOMO} = -4.78 + ($E^{1/2}{}_{ox}$(Fc)-($E^{1/2}{}_{ox}$)); [b] E_{LUMO} = -4.78 + ($E^{1/2}{}_{ox}$(Fc)-($E^{1/2}{}_{red}$))[103]

[c] E_{gap} = E_{HOMO}-E_{LUMO}

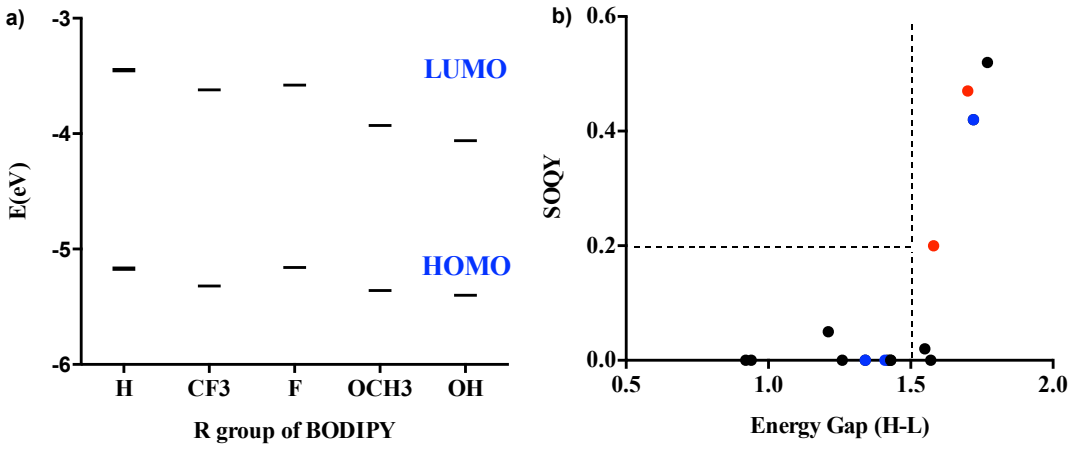


Figure 25. a) Mapping of HOMO LUMO energy levels, b) Critical HOMO-LUMO energy difference threshold required for ≥ 0.2 SO quantum yield.

2.8 Time-resolved Transient Absorption Spectra

Transition absorption experiments were performed by Dr. Francis D'souza. In order to study the triplet state of SBDPiRs, we recorded time-resolved spectra of SBDPiRs 690 and 731[105]. For both compounds, significant bleaching band was detected in the femtosecond transient absorption spectra (A and B), at 708 nm and 726-754 nm, respectively, due to the depletion of ground state SBDPiRs (Figs. 26 and 27). In the nanosecond transient absorption spectra (C and D), positive absorption peak was observed at 594 and 550-650 nm for SBRPiRs 690 and 731 nm, respectively, presumably due to the absorption of triplet species of these dyes (Figs. 28 and 29). Interestingly, transient bands of the triplet-excited state were persistent for nearly 50 ms in the case of SBDPiR731 compared to about 3 ms of 690 (Figs. 30 and 31). Since longer triplet lifetime is preferred for SO generation, we hypothesize that the determinant factor for SO generation of, at least, these two dyes is not triplet state lifetime, but possibly the quantum yield of triplet state, the other key factor of Φ_Δ. Detailed spectral studies are underway to prove this hypothesis, which will be presented in due course.

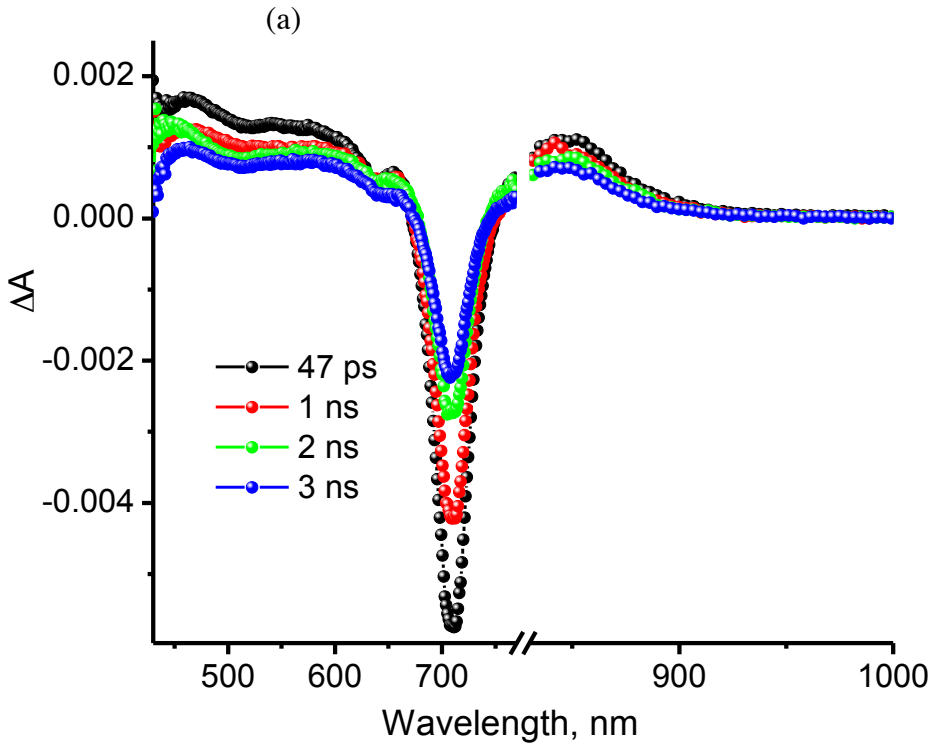


Figure 26. Femto-second spectrum of **SBDPiR690** at the indicated time intervals in oxygen free benzonitrile.

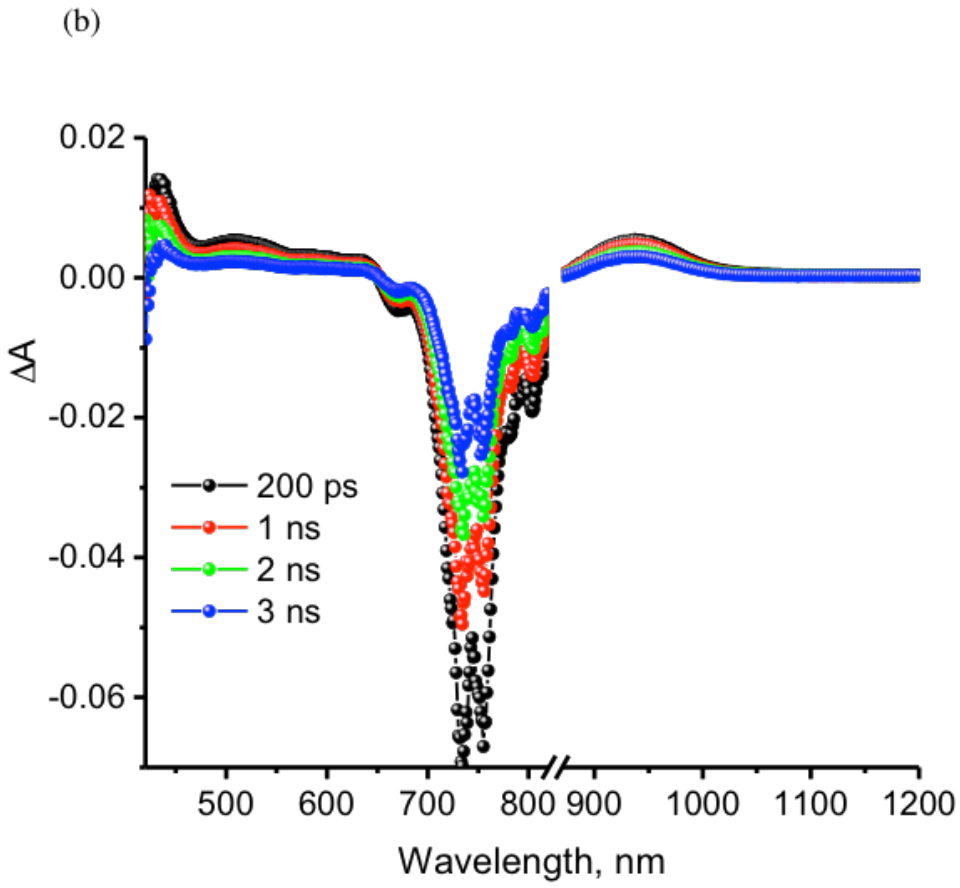


Figure 27. Femto-second spectrum of **SBDPiR731** at the indicated time intervals in oxygen free benzonitrile.

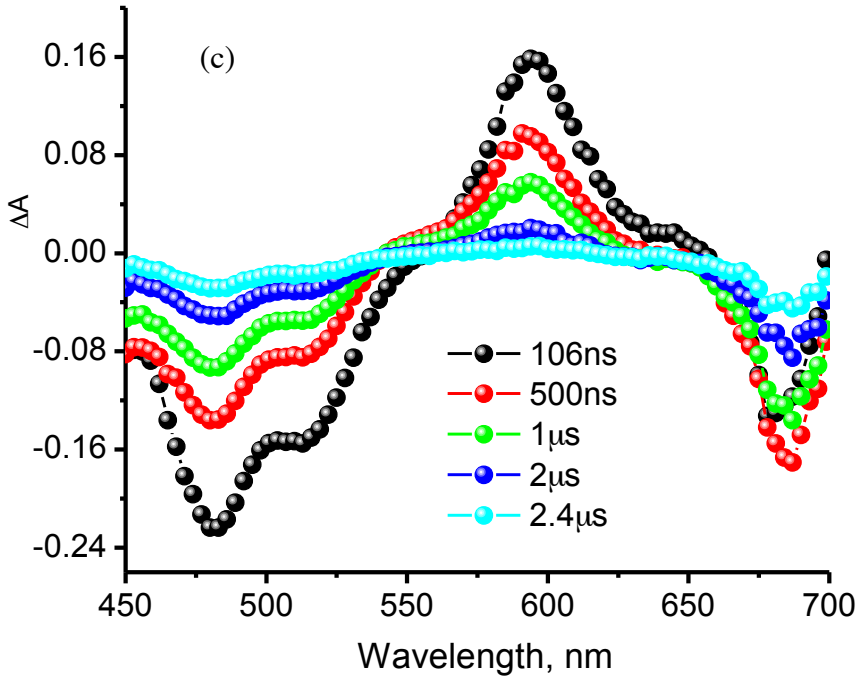


Figure 28. nano-second transient absorption spectrum of **SBDPiR690** at the indicated time intervals in oxygen free benzonitrile.

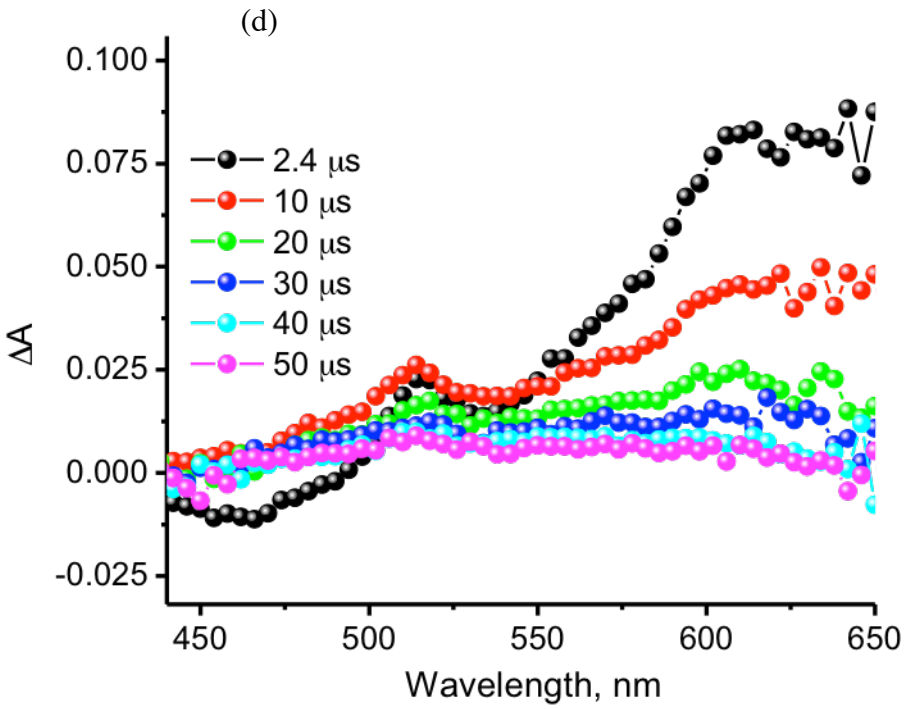


Figure 29. nano-second transient absorption spectrum of **SBDPiR731** at the indicated time intervals in oxygen free benzonitrile

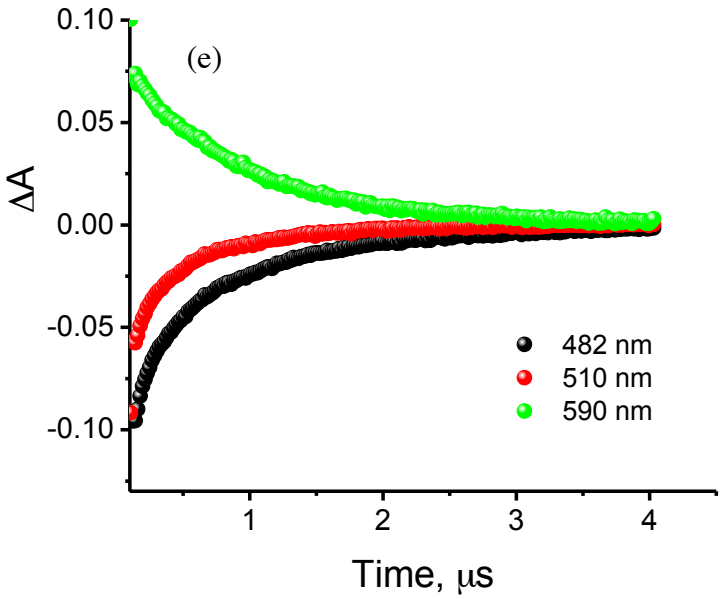


Figure 30. Decay profile of **SBDPiR690** after nanosecond pulsed excitation at the indicated time intervals wavelength in oxygen free benzonitrile.

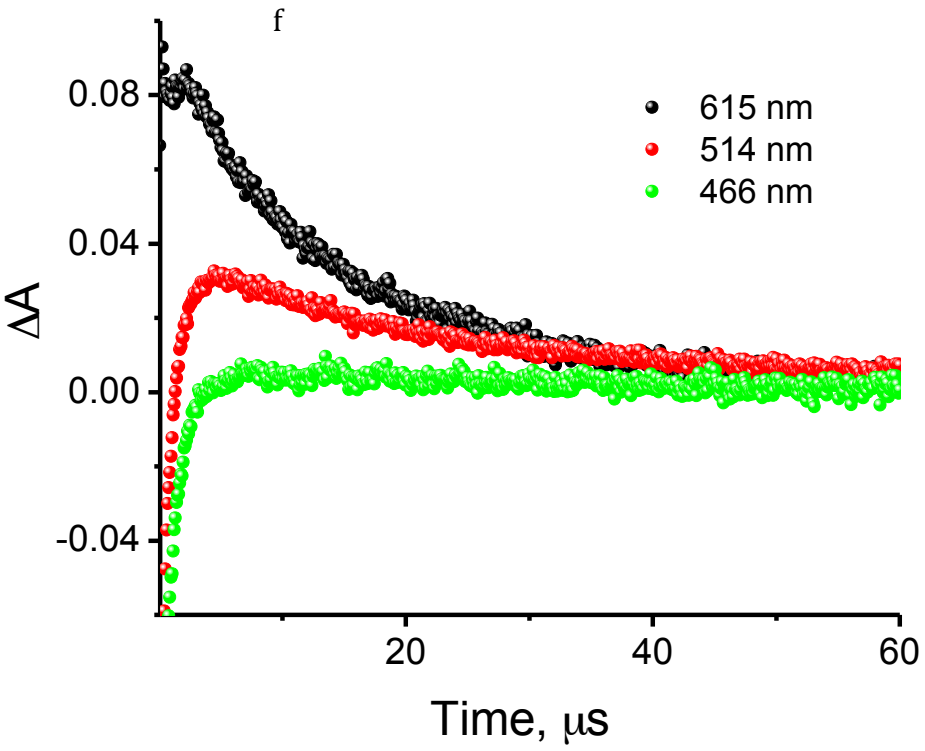


Figure 31. Decay profile **of SBDPiR731** after nanosecond pulsed excitation at the indicated time intervals wavelength in oxygen free benzonitrile.

2.9 Conclusion

Photodynamic therapy's clinical use has been hampered due to less than ideal photosensitizers. The BODIPY class of dyes have shown promise to overcome the limitations set by approved photosensitizer classes such a porphryins and pathalocyanines. Until now, it was of conventional practice to design potential BODIPY photosenistizers to incorporate (1) extended conjugation with π-donor and π-acceptor substituents in hopes of visible to near infrared absorption (2) inclusion of the heavy atom effect i.e. coupled Br, I, for induction of intersystem crossing and subsequent triplet state to $^1O_2$ generation (3) A resonance energy transfer between dimers, dyads, or triads of BODIPY dyes and sensitizers for broad band absorption in the visible region and $^1O_2$ generation. Heretofore even as recent as the year 2013 and 2014, the scientific community insists the HAE must be incorporated within mono-chromophore BODIPY dyes for ISC i.e. through spin orbit coupling.[106, 107]

We successfully demonstrated that monomeric BODIPY-based dyes can generate singlet oxygen without heavy atom effect and the efficiency of singlet oxygen generation can be modulated by the substituents. From the structure-property relationship analysis of these SBDPiRs, we observed that the electron withdrawing groups at the aromatic ring increased both HOMO-LUMO energy gap and singlet oxygen quantum yield. More noticeable was that the SBDPiR photosensitizers also showed moderate brightness, which makes these suitable for the optical image-guided PDT. The transition absorption spectroscopy offers details mechanistic evidence of intersystem crossing absent heavy atom contribution.

2.0.1 Experimental and General Methods

2.0.2 (**35**) Ethyl 2-bromo-4H-thieno[3,2-b]pyrrole-5-carboxylate[102]: Ethyl azidoacetate (31.0 g, 240.31 mmol) and 5-bromothiophene 2-carboxyaldehyde (11.5 g, 60.0 mmol) were dissolved in absolute ethanol (500.0 mL) under ice at -15 °C for 25 min. A 21% ethoxide solution (0.089 L, 240.0 mmol) was added dropwise to the mixture and stirring continued for 2 h. A saturated solution of ammonium chloride was added to yield a yellow precipitate, which was collected by filtration and dried. The resulting brown residue was dissolved in toluene and allowed to reflux 2 h. The solvent was evaporated and purified by column chromatography (silica gel) using gradient elution of ethylacetate: hexane (5-30:95-70) to obtain a brown solid, yield 75%. ^{1}H NMR (300 MHz, CD_2Cl_2) δ 1.38 (t, J = 7.2 Hz, 3H), 4.37 (q, 2H), 7.03 (s, 1H), 7.04 (s, 1H), 9.18 (br s, 1H). ethyl 2-bromo-4H-thieno[3,2-b]pyrrole-5-carboxylate **(35)** has been previously reported and was synthesized by the literature with minor modifications.[105]

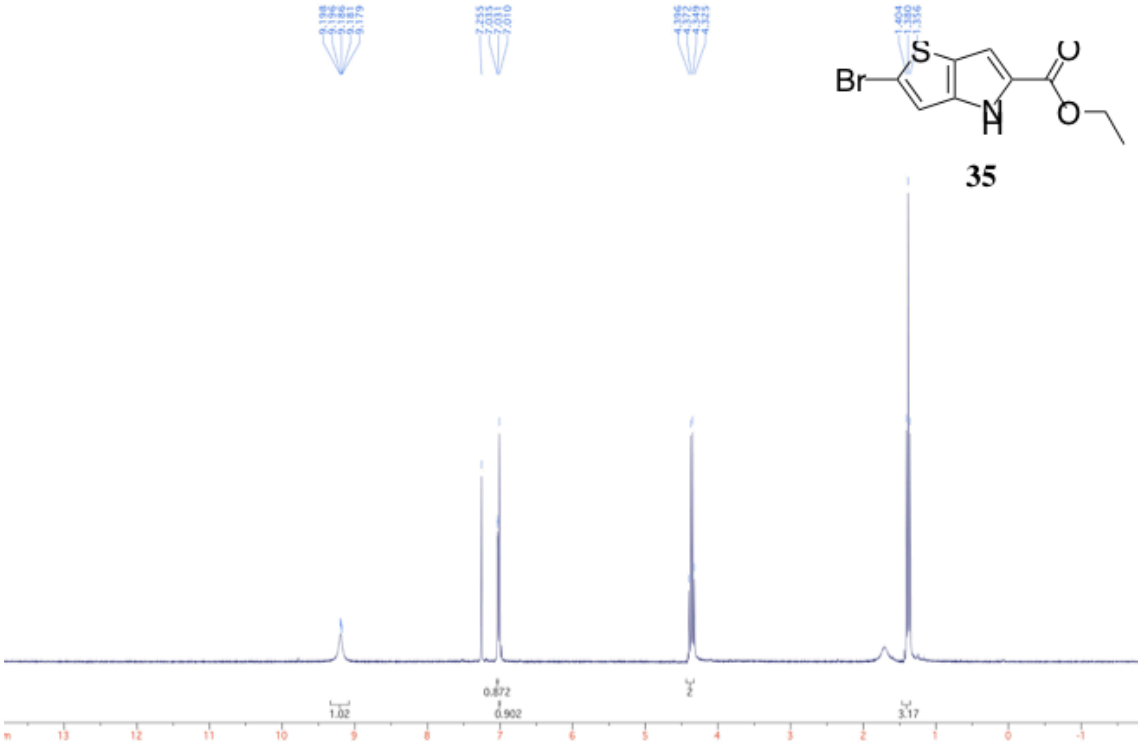


Figure 32. ^{1}H NMR of compound **35**

2.0.2 (**36**) 2-Bromo-4H-thieno[3,2-b]pyrrole-5-carboxylic acid [102]: Ethyl-2-bromo-4H-thieno[3,2-b]pyrrole-5-carboxylate (**35**) (5.0 g, 18 mmol) was dissolved in ethanol (100.0 mL). Sodium hydroxide (11.0 g, 0.28 mol in water (50.0 mL) was added under reflux for 1.5 h. The reaction was cooled to room temperature and then chilled in ice to acidify mixture with concentrated hydrochloric acid. The precipitate was filtered and, washed with water and dried. **36** was obtained as a dark green solid (3.7 g, 82%). ^{1}H NMR (300 MHz, CD_2Cl_2) δ 6.94 (s, 1H), 7.12 (s, 1H), 11.99 (s, 1H). **(36)** has been previously reported and was synthesized by the literature with minor modifications.[105]

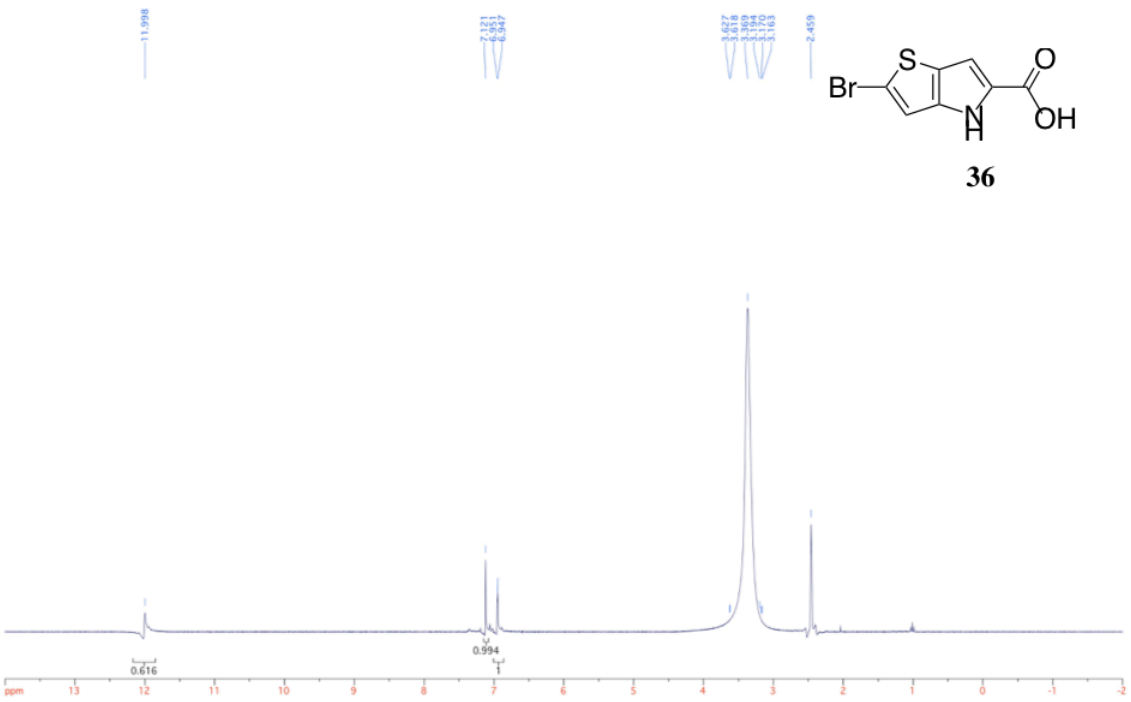


Figure 33. ^{1}H NMR of compound **36**.

2.0.3 (BDP635) 2,8-Dibromo-5,5-difluoro-11-(trifluoromethyl)-5H-thieno[2',3':4,5] pyrrolo [1,2-c] thieno[2',3':4,5]pyrrolo[2,1-f][1,3,2]diazaborinin-4-ium-5-uide[102]: 2-Bromo-4*H*-thieno[3,2-*b*]pyrrole-5-carboxylic acid (**51**) (2.0 g, 8.1 mmol SFs!!) was dissolved in trifluoroacetic acid (25 mL) and stirred at 40 °C for 30 min. Trifluoroacetic anhydride (15 mL) was added and the mixture stirred at 80 °C for 6 h forming an intense blue color. After cooling, the reaction was poured into saturated aqueous $NaHCO_3$ solution to neutralize. The formed precipitate was filtered, washed with water and dried *in vacuo*. The resulting compound (**52**) was dissolved in dichloromethane (500 mL), boron trifluoride diethyl ether complex (7 mL) and triethylamine (5 mL) were added to stir for 1 h. The reaction mixture was added directly to silica gel (eluent CH_2Cl_2) for purification to obtain **(BDP635)** as a bluish green metallic solid (0.215 g,

5%). ^{1}H NMR (CD_2Cl_2, 300 MHz): δ=7.3 (s, 2H), 7.2 (s, 2H); **BDP635** has been previously reported and was synthesized by the literature with modification.[105]

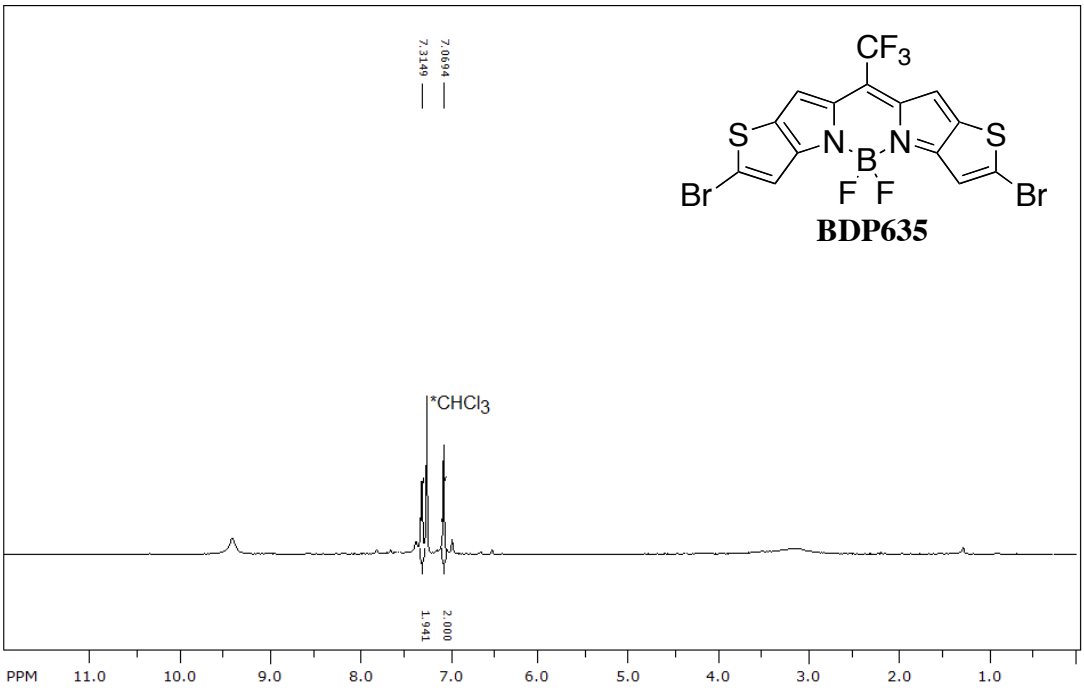


Figure 34. ^{1}H NMR of **BDP635**.

2.0.4 (SBDPiR690) 5,5-Difluoro-2,8-diphenyl-11-(trifluoromethyl)-5H-thieno [2',3':4,5]pyrrolo[1,2-c]thieno[2',3':4,5]pyrrolo[2,1-f][1,3,2]diazaborinin-4-ium-5-uide [102]: ^{1}H NMR (CD_2Cl_2, 300 MHz): δ 7.8 (s, 1H), 7.7 (s, 1H), 7.6 (d, J = 8.0 Hz, 4H), 7.5 (s,1H), 7.4 (peaks overlap, 7H). HRMS EI (m/z): Calculated for $C_{26}H_{14}BF_5N_2S_2$ 524.0612; Found: 524.0599 [M]+. SBDiR690 has been previously reported and was synthesized by the literature with modification.[102]

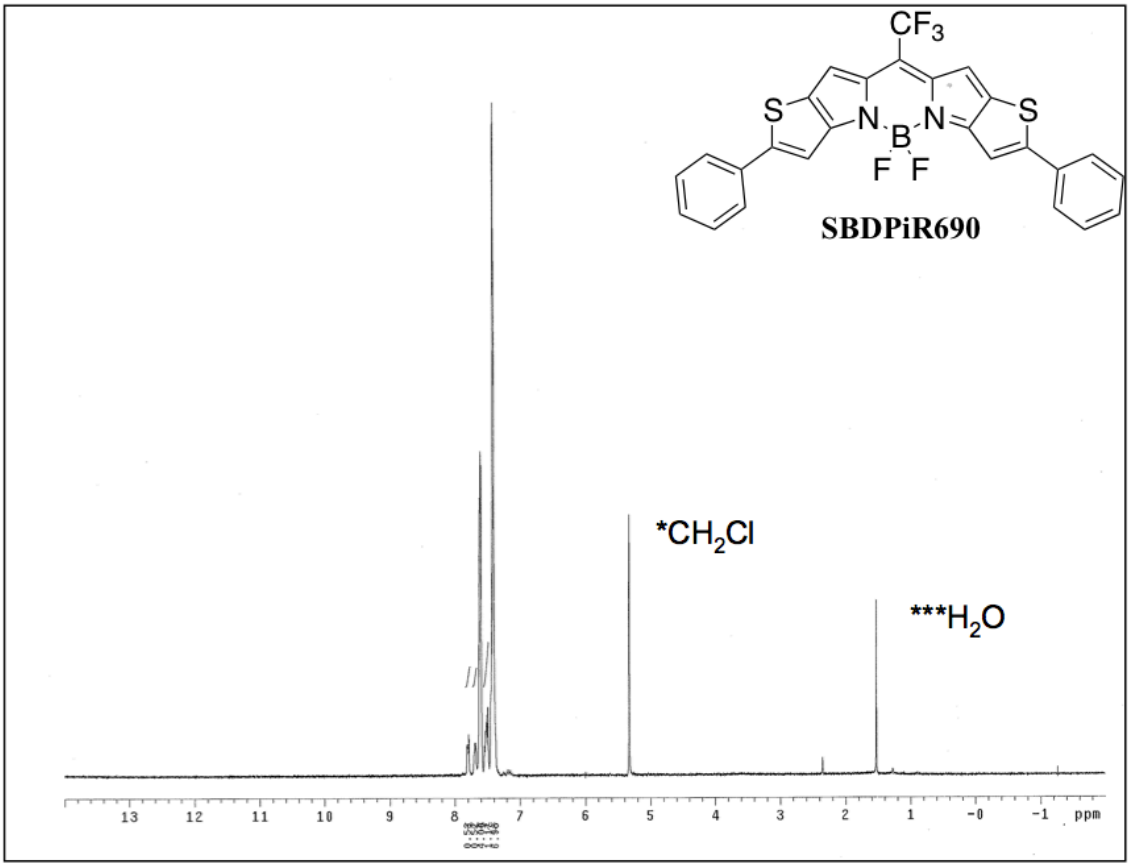


Figure 35. ^{1}H NMR of **SBDPiR690**.

2.0.5 (SBDPiR731) 5,5-Difluoro-2,8-bis(4-methoxyphenyl)-11-(trifluoromethyl)-5H-thieno[2',3':4,5]pyrrolo[1,2-c]thieno[2',3':4,5]pyrrolo[2,1-f][1,3,2]diazaborinin-4-ium-5-uide [102]: ^{1}H NMR (CD_2Cl_2, 300 MHz): δ 7.8 (d, J = 8.0 Hz, 4H), 7.3 (s, 2H), 7.3 (s, 2H), 7.0 (d, J = 8.0 Hz, 4H), 3.9 (s, 6H); HRMS EI (m/z): Calculated for $C_{28}H_{18}BF_5N_2O_2S_2$ 584.0823; Found: 584.0825 [M]+. **SBDPiR731** has been previously reported and was synthesized by the literature with modification.[102]

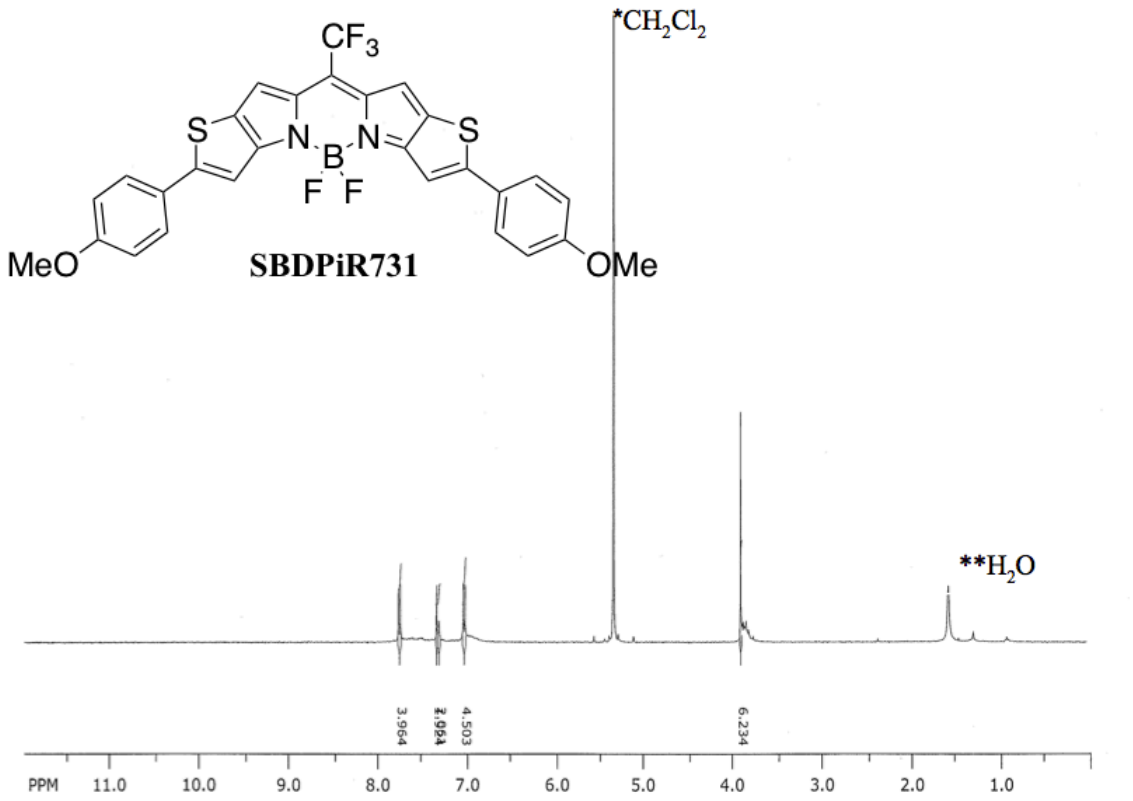


Figure 36. ^{1}H NMR of **SBDPiR731**.

2.0.6 (SBDPiR698) 5,5-Difluoro-2,8-bis(4-fluorophenyl)-11-(trifluoromethyl)-5H-thieno[2',3':4,5] pyrrolo[1,2-c] thieno[2',3':4,5] pyrrolo[2,1-f][1,3,2] diazaborinin-4-ium-5-uide: To a solution of **BDP635** (0.100 g, 0.188 mmol) in toluene, tetrahydrofuran, water (30 mL 1:1:1) was added 4-fluorophenyl boronic acid (0.079 g, 0.57 mmol), Na_2CO_3 (0.060 g, 0.566 mmol). The reaction was purged with nitrogen gas for 10 min. A catalytic amount of $[Pd(PPh_3)_4]$ (0.033 g, ~5 mol %) was added and the reaction was heated to 80 °C for 2-3 h. After completion of the reaction, the reaction was diluted with 10 mL water and extracted with toluene. The combined organic layer was washed with water and brine (100 mL each) and dried over anhydrous Na_2SO_4. The dried mixture was purified by silica-gel column chromatography (80:20

hexanes:toluene) to afford **SBDPiR698** as a dark green solid (0.034 g, 32%). ^{1}H NMR (CD_2Cl_2, 300 MHz): δ= 7.8 (t, *J* = 7.6, 4H), 7.4 (s, 4H), 7.2(t, *J* = 8.3, 4H); HRMS EI (m/z): calculated for $C_{26}H_{12}BF_7N_2S_2$: 560.0423; found 560.0416 $[M]^+$.

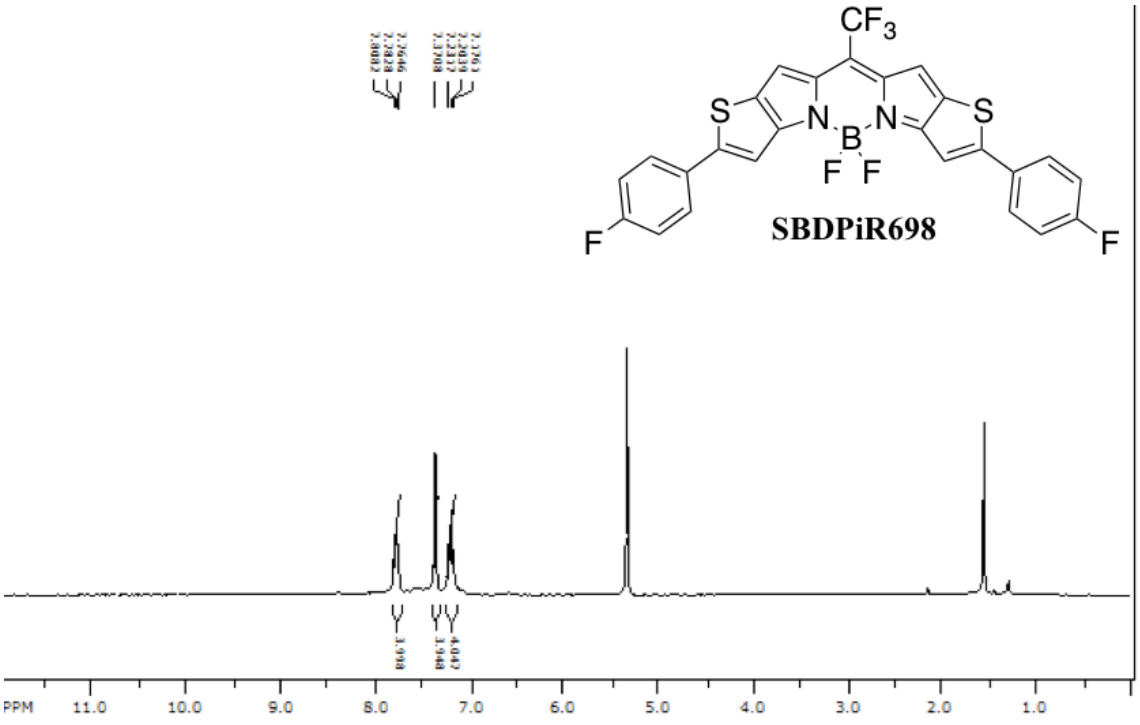


Figure 37. ^{1}H NMR of **SBDPiR698**.

2.0.7 (SBDPiR688) 5,5-Difluoro-11-(trifluoromethyl)-2,8-bis (4-(trifluoromethyl) phenyl)-5H-thieno[2',3':4,5]pyrrolo[1,2-c]thieno[2',3':4,5]pyrrolo[2,1-f][1,3,2]diazaborinin-4-ium-5-uide: The method described for **SBDPiR698** was followed using **BDP635** (0.100 g, 0.18 mmol), 4-(trifluoromethyl)phenyl) boronic acid (0.100 g, 0.526 mmol), Na_2CO_3 (0.060 g, 0.566 mmol). The dried mixture was purified by silica-gel column chromatography (90:10 hexanes:ethyl acetate) to afford **SBDPiR688** as a dark green solid (0.103 g, 28%). ^{1}H NMR (CD_2Cl_2, 300 MHz): δ= 7.9

(d, J = 8.1, 4H), 7.6 (d, J = 3.6, 4H), 7.5 (s, 2H), 7.4 (s, 2H); HRMS EI (m/z): calculated for $C_{28}H_{12}BF_{11}N_2S_2$ 660.0359; found 660.0355 [M]+.

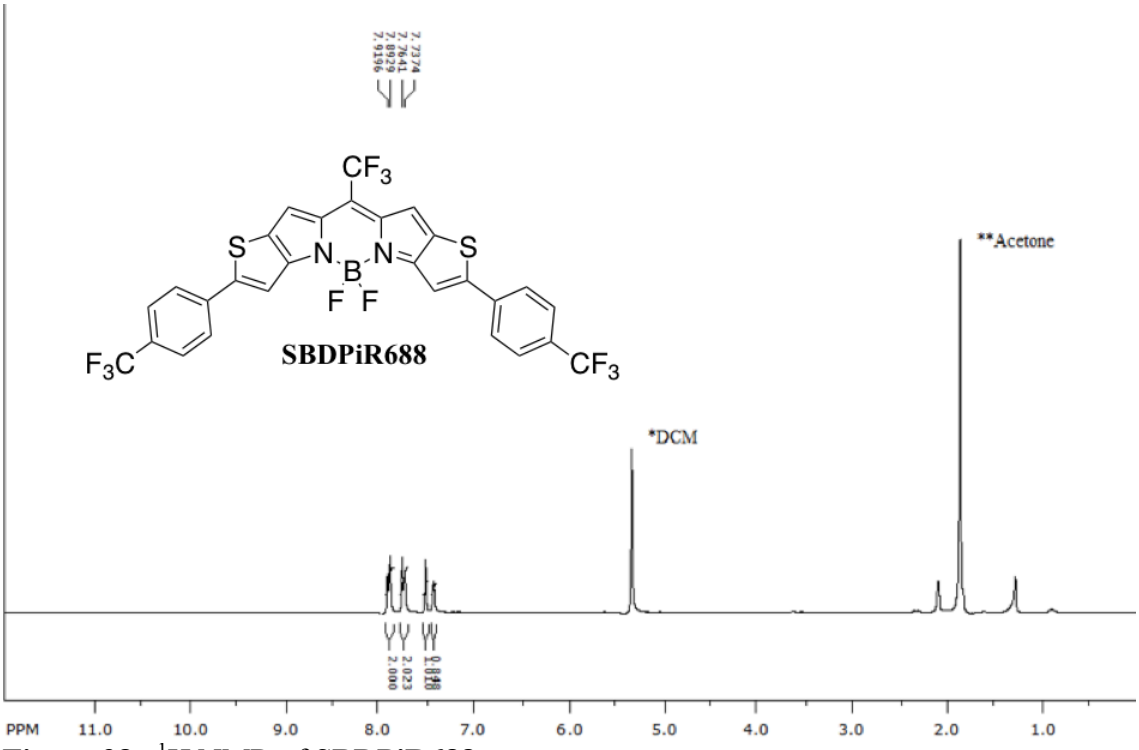


Figure 38. ^{1}H NMR of **SBDPiR688**

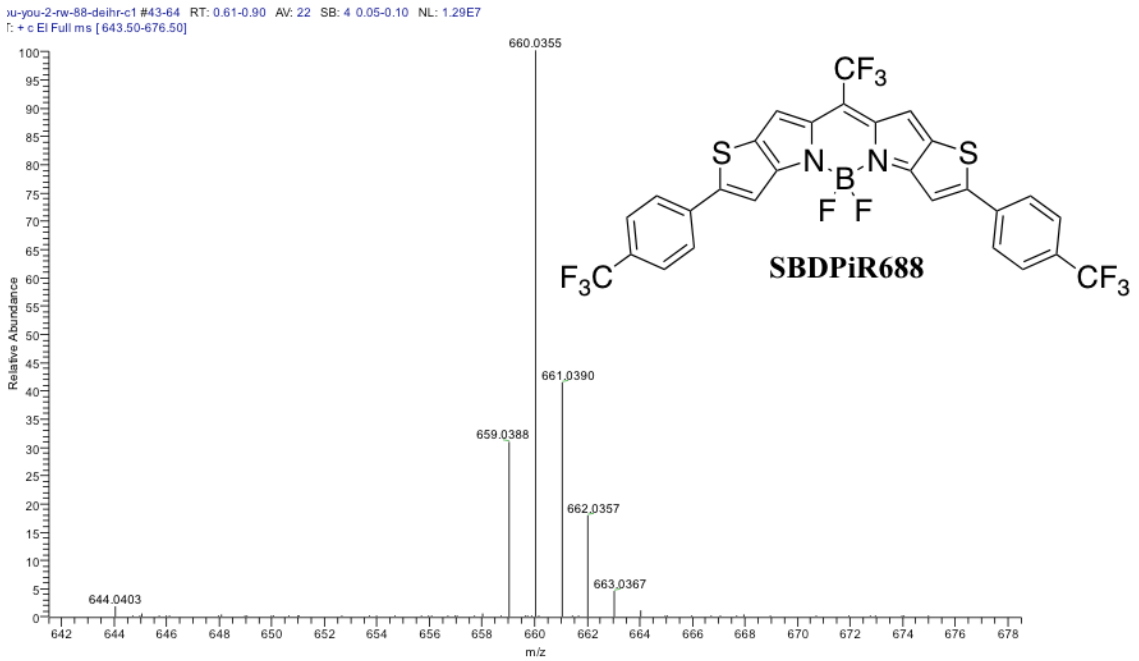


Figure 39. HRMS EI of **SBDPiR688**.

2.0.8 (SBDPiR740) 5,5-Difluoro-2,8-bis(4-hydroxyphenyl)-11-(trifluoromethyl)-5H-thieno [2',3':4,5] pyrrolo[1,2-c]thieno[2',3':4,5]pyrrolo[2,1-f][1,3,2]diazaborinin-4-ium-5-uide [102]: **SBDPiR740** was synthesized according to reported literature.[105] ^{1}H NMR (acetone-d_6, 300 MHz): δ 7.8 (d, J = 9.0 Hz, 4H), 7.5 (s, 2H), 7.4 (s, 2H) 7.0 (d, J = 9.0 Hz, 4H); HRMS EI (m/z): Calculated for $C_{26}H_{14}BF_5N_2O_2S_2$ 556.0510; Found: 556.0520 [M]+.

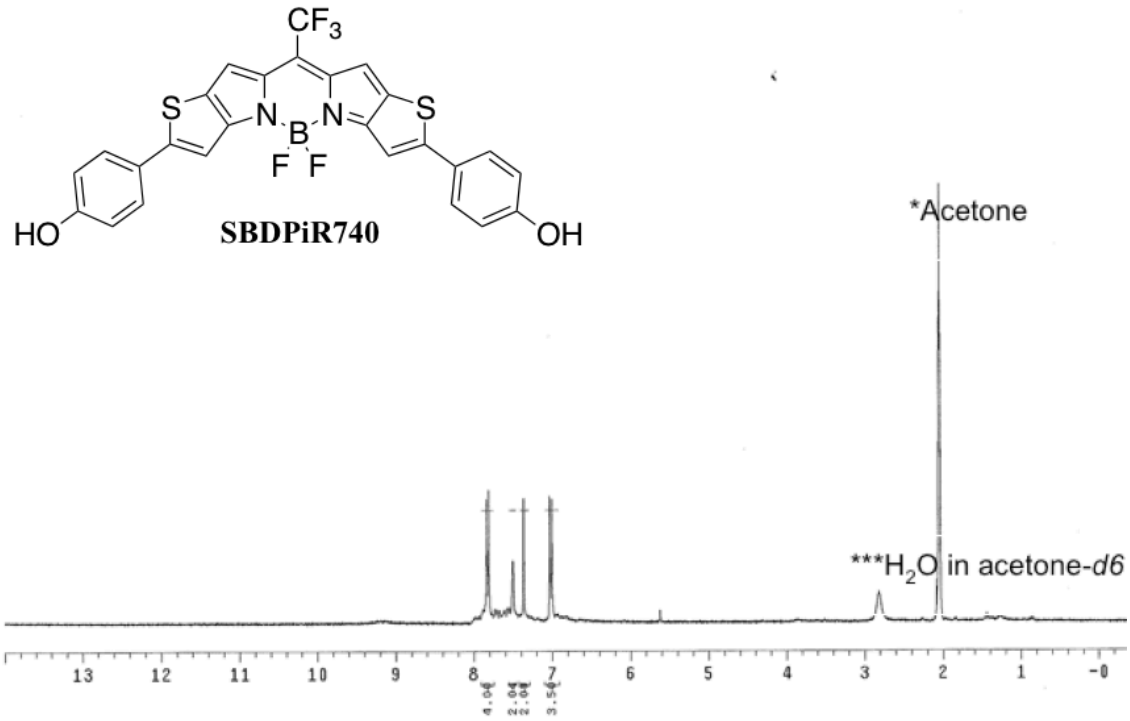


Figure 40. ^{1}H NMR of **SBDPiR740**.

2.0.9 (SBDPiR710): 5,5-Difluoro-2,8-di-p-tolyl-11-(trifluoromethyl)-5H-thieno[2',3':4,5]pyrrolo[1,2-c]thieno[2',3':4,5]pyrrolo[2,1-f][1,3,2]diazaborinin-4-ium-5-uide: The method described for **SBDPiR698** was followed using **BDP635** (0.100 g, 0.188 mmol), *p*-tolylboronic acid (0.076 g, 0.560 mmol), Na_2CO_3 (0.060 g, 0.566 mmol). The dried mixture was purified by silica-gel column chromatography (70:30 hexanes:toluene) to afford **SBDPiR710** as a dark green solid (0.024 g, 43%). ^{1}H NMR (acetone-d_6, 300 MHz): δ= 7.67 (d, J = 7.2 Hz, 4H), 7.4 (s, 2H), 7.3 (m, 6H), 2.4 (s, 6H); LRMS EI (m/z): calculated for $C_{28}H_{18}BF_5N_2S_2$ 552.1: found 552.0 [M]+.

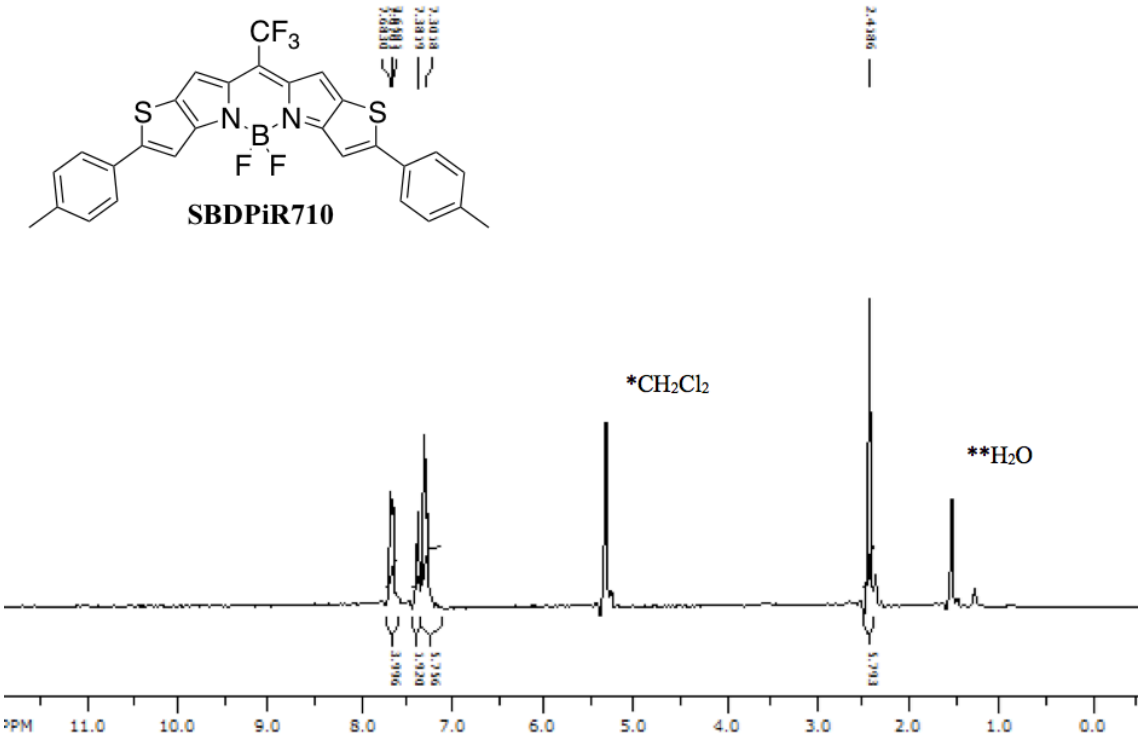


Figure 41. ^{1}H NMR of **SBDPiR710**.

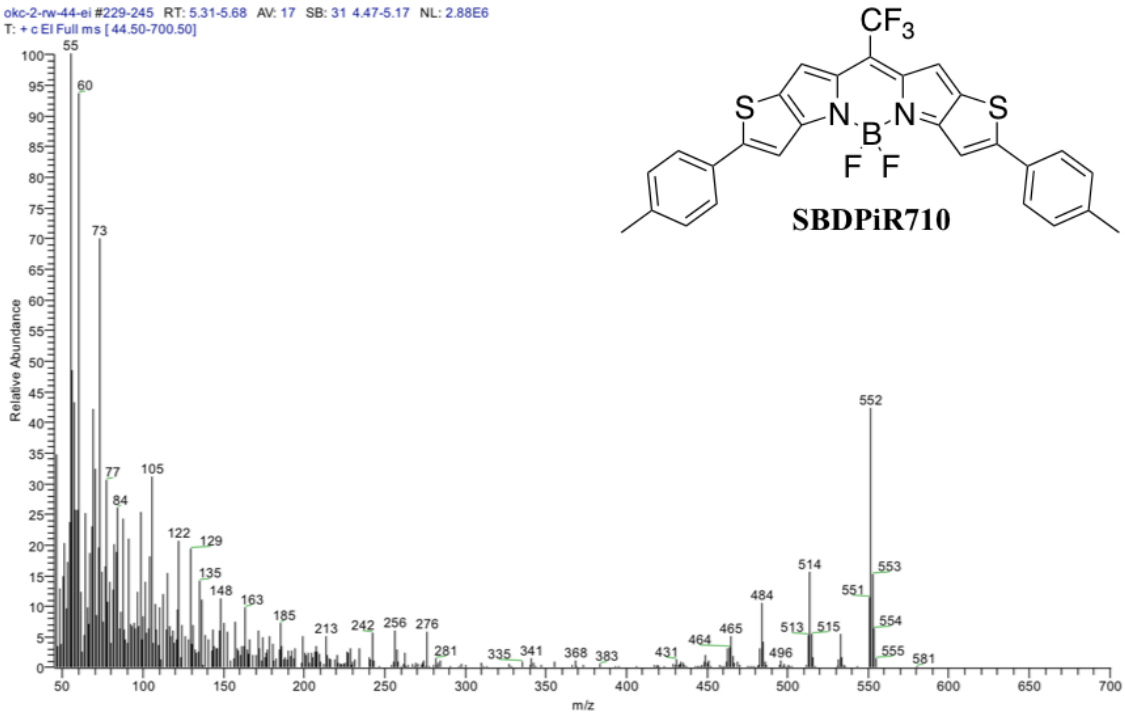


Figure 42. LRMS EI of **SBDPiR710**.

2.1.0 (SBDPiR700) 2,8-Bis(4-cyanophenyl)-5,5-difluoro-11-(trifluoromethyl)-5H-thieno[2',3':4,5]pyrrolo[1,2-c]thieno[2',3':4,5]pyrrolo[2,1-f][1,3,2]diazaborinin-4-ium-5-uide: The method described for **SBDPiR698** was followed using **BDP635** (0.100 g, 0.188 mmol), *p*-cyanophenyl boronic acid (0.083 g, 0.565 mmol), Na_2CO_3 (0.080 g, 0.755 mmol). The dried mixture was purified by silica-gel column chromatography (80:20 hexanes: ethyl acetate) to afford **SBDPiR700** as a dark green solid (0.024 g, 37%). ^{1}H NMR (300 MHz, CD_2Cl_2) δ 0.89 (t, J = 7.2 Hz, 3H), 2.89 (q, 2H), 7.45 (s, 1H), 7.52 (s, 1H), 7.78 (d, J = 8.4 Hz, 2H), 7.87 (d, J = 8.6 Hz, 2H). HRMS EI (m/z): calculated for $C_{28}H_{12}BF_5N_4S_2$ 574.1: found 574.05[M]+.

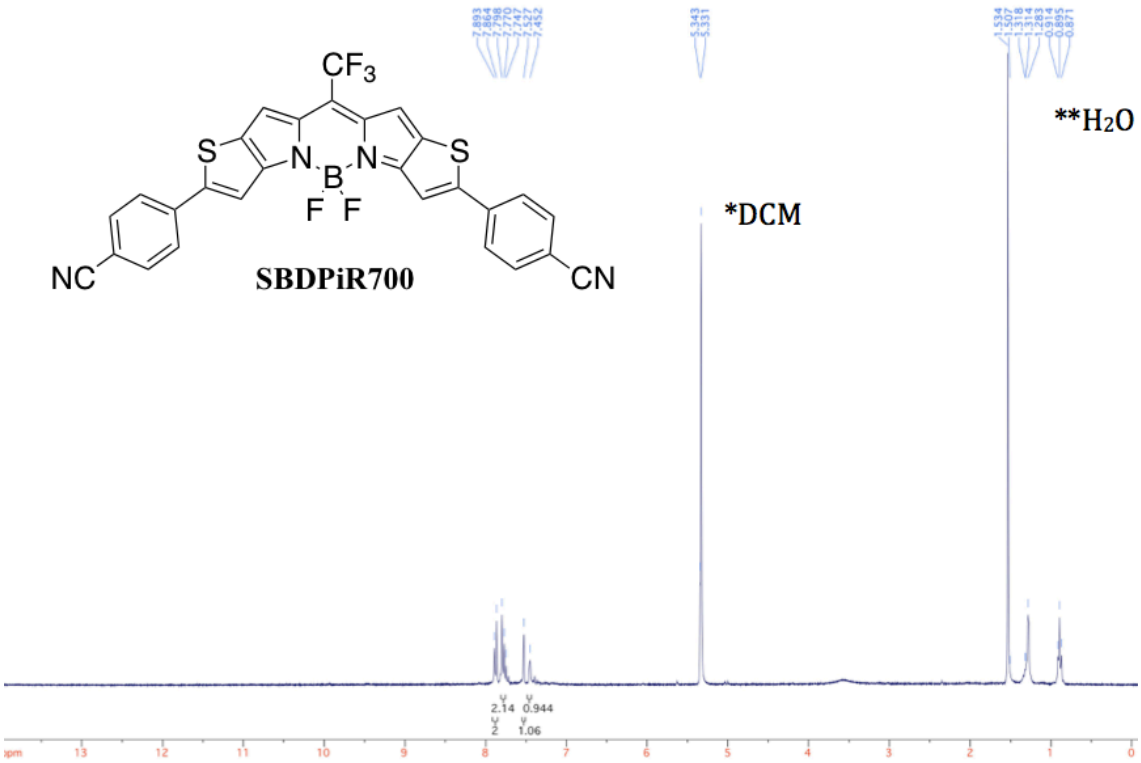


Figure 43. ^{1}H NMR of **SBDPiR700**.

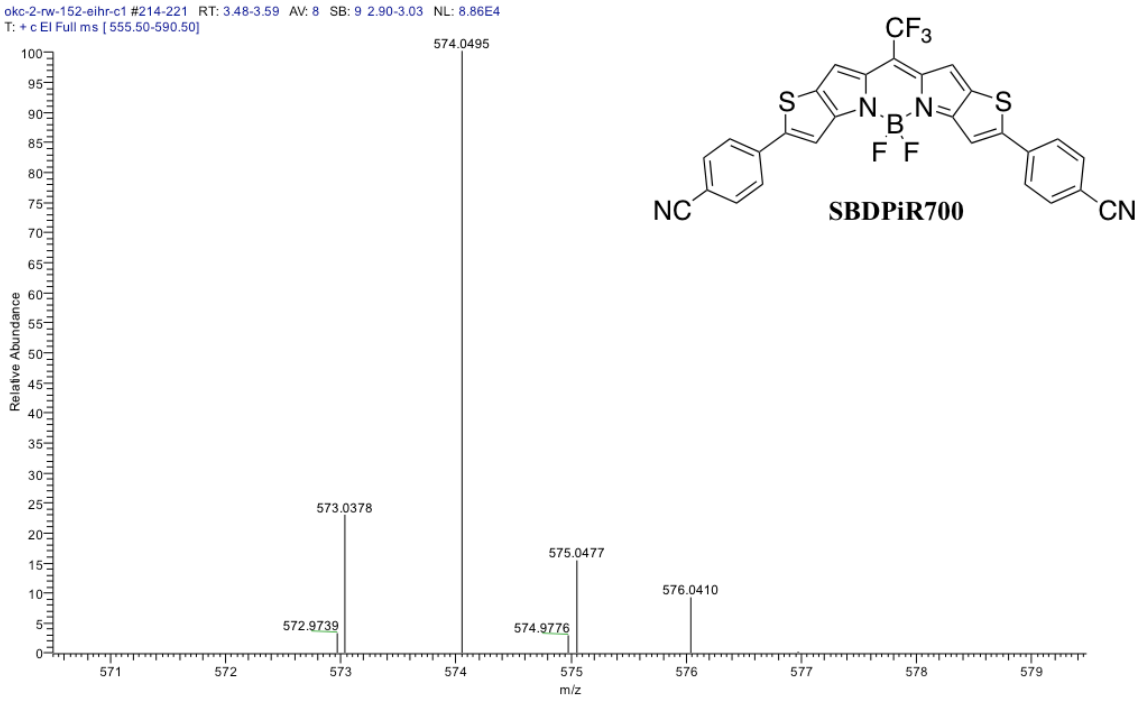


Figure 44. HRMS EI of **SBDPiR700**.

Absorbance spectra were recorded on a Perkin Elmer lambda 25 UV/Vis spectrometer. Steady-state and lifetime fluorescence were measure using a Horiba Jobin Yvon UV/Vis/NIR fluorimeter a data station. Extinction coefficients were determined experimentally. SBDPiR (ca. 1 mg) was dissolved in $CHCl_3$ (5mL) and serially diluted to yield variable concentrations (10^{-6} to 10^{-7} M). A graph illustrating the slope of absorbance versus concentration was plotted and fitted into Beer-Lambert Law. Fluorescence quantum yields were estimated according to standard protocol.

Fluorescence lifetimes were obtained by a single exponential curve. The fluorescence emission spectra of SBDPiRs using aza-BODIPY (Φ_{flu}= 0.34) as a standard were recorded at 25^{o}C. Spectra of diluted SBDPiR and aza-BODIPY were obtained to compare their fluorescence emission spectra after excitation of 710 nm. The absorbance

of SBDPiR and aza-BODIPY were also obtained. A graph of fluorescence versus absorbance was plotted to generate the gradient (G). Fluorescence quantum yield was calculated using the equation:

$$\Phi_x = \Phi_{std}(G_x/G_{std}) (\eta^2_x/\eta^2_{std})$$

Where the subscripts std and x represent the standard and SBDPiR sample. Φ denotes fluorescence quantum yield, G is the gradient obtain from absorbance versus fluorescence intensity, and η is equivalent to the refractive index of the solvent.

A Horiba Jobin Yvon UV-Vis/NIR fluorimeter was used to measure the singlet oxygen luminescence spectra at 1270 nm. SO quantum yield was determined in $CHCl_3$ with $[Ru(bipy)_3]Cl_2$ as a reference ($\Phi_\Delta = 0.77$ in MeOH).

Redox potentials of all SBDPiRs were measured by Dr. Francis D'souza at the University of North Texas. Redox potentials were determined with a homemade three electrode divided cell consisting of a carbon working electrode, a saturated calomel reference electrode (SCE) and a platinum wire counter auxiliary electrode. A fritted-glass bridge of low porosity was used to separate the SCE from bulk solution, which contained the electrolyte tetra-*n*-butylammonium perchlorate, TBAP.

Chapter III. Application of NIR Dual Functioning BODIPY PS SBDPiR690

3.0 Introduction

The evaluation of BODIPY dyes as a novel class of highly active PDT agents has recently become of prime interest.[99b, 108] As discussed, PDT is a promising non-invasive treatment modality that relies on the illumination of a systemically administered photosensitizer with visible/NIR light to generate reactive oxygen species, predominantly, singlet oxygen ($^1O_2$) – a key cytotoxic agent.[109] The cytotoxic species as a result of PDT performs tumor destruction through various mechanisms. A direct effect on cancer cells leads to cell death by necrosis or apoptosis is commonly experienced. PDT can also affect tumor vasculature to shut down blood vessels, which consequently affects oxygen and nutrient supply to the tumor. The immune system can also be affected after PDT and leads to immunostimulatory or immunosuppressive conditions.[47] PDT is in current clinical and preclinical use for the treatment of broad cancerous conditions including breast, skin, lung, gastrointestinal tract, colon, ovarian and prostate cancers.

Non-malignant diseased states such as age-related macular degeneration (AMD), resistant microbial infections and atherosclerosis are treated with PDT. In addition to the mechanisms, the outcomes of PDT can be influenced by photosensitizer concentration, light dose, drug-light and oxygen availability.[27] Antivascular effects of PDT are primarily facilitated by the natural tendency of sensitizers to accumulate in blood vessels. Photosensitizers may be referred to as anti-angiogenesis agents, which prevent the formation of blood vessels and growth of endothelial cells. During

antiangiogenic PDT, short drug administration and light illumination intervals are desired.[110] Vascular-targeted PDT (VTP) possesses numerous advantages in improved efficacy of treatment. Photosensitizers accumulate in high concentrations within tumor blood vessels after intravenous administration. The essential element for photochemical reaction, molecular oxygen, is readily available.[110-111] Moreover, the role of the vascular network to supply oxygen and nutrients to cancer cells make the occlusion of vessels an effective approach to treat tumors. Overall, this approach can be used to treat different tumor types when considering the shared biochemical and morphological properties of cancerous blood vessels.[111]

Herein, we demonstrate *in vitro* and *in vivo* imaging and PDT following a short drug-light interval protocol of the non-halogenated NIR BODIPY, **SBDPiR690**. The appreciable fluorescence and singlet oxygen properties of **SBDPiR690** coupled with the in vivo PDT performance shows promise for what is term fluorescence guided - vascular targeted PDT (FG-VTP).

3.1 *In vitro* Photo and Dark Toxicity

Varying concentrations of SBDPiR690 from a DMSO stock solution were incubated with the cells in the dark for 24 h. Subsequently, the culture medium was removed and fresh culture medium was added to each well. The plates were irradiated with a laser light source of wavelength 690 nm at a delivered light dose of 5.6 mW cm^{-2} for 30 min (~10 J cm^{-2}). After illumination, the cells were returned to normal medium and incubated for an additional 24 h at 37 °C following which percent cell viability was

determined using MTT assay. Dark toxicity of SBDPiR690 was determined in similar fashion as described above without illumination. All assay experiments were carried out in triplicate and an average of the three individual runs are presented.

Following our assay protocol, colon 26 cells displayed no determinable dark toxicity (DT) with SBDPiR690 up to a concentration of 10^{-4} M. In contrast, illumination with 10 J cm^{-2} light dose displayed significant phototoxicity (PT) with IC_{50} values determined as 3.2 x 10^{-6} M (Fig. 45).

The remarkable phototoxicity of SBDPiR690 was encouraging, as this molecule contains no halogens as characterized by BODIPY photosensitizers and sets up an unprecedented non-halogenated NIR BODIPY structure as a photocytotoxic agent. The data clearly demonstrates that we have achieved promising activity (micro molar range) with the structurally unique SBDPiR690. The heavy-atom contributions through fusion of thiophene units are currently under investigation as the sulfur atoms may influence the excited triplet-state population and aid in the production of moderate singlet oxygen quantum yields.

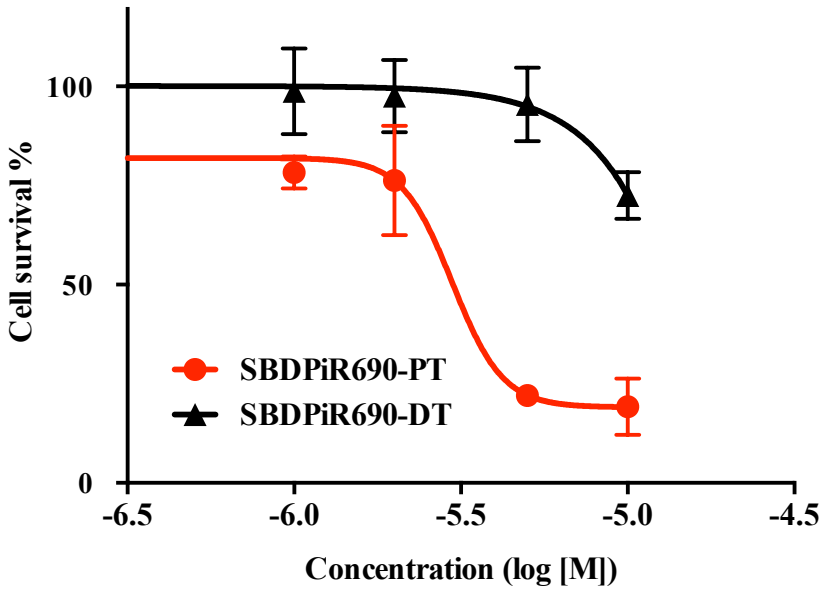


Figure 45. SBDPiR690 Concentration dependent cell survival.

3.2 Drug Bio-distribution and Clearance using SBDPiR690

Small animal whole body fluorescence imaging was performed with an IVIS Spectrum (PerkinElmer Inc.) and the acquired images and fluorescence signals were analyzed using Living Image Software v4.0 (PerkinElmer Inc.). Excitation and emission wavelengths 675 and 720 nm respectively were used for acquiring in vivo SBDPiRs fluorescent images. All images were obtained using an exposure time of 0.5 or 2 s and an f/stop of 2. Mice were injected with 2 μmole/kg SBDPiR690 through the retro-orbital vein and were anesthetized before imaging using the excitation and emission wavelength of SBDPiR690 at various time points.

Ex vivo imaging from excised organs and fluorescence quantification was used to demonstrate drug distribution patterns (Fig. 46). Generally, fluorescent signals from

organs reduced to reach baseline levels by the 24 h time point. It was evident that fluorescent signals within the lungs and liver peaked at 3 h and 9 h respectively and 1 h for the spleen, indicating high SBDPiR690 concentrations at those time points. Furthermore, the heart, kidneys and tumor showed maximum SBDPiR690 concentrations at 15 min as evidenced by their fluorescence intensity signals and subsequently cleared over time. Although a fluorescence signal within the tumor was relatively weak it provides useful information for precise drug-light interval towards effective PDT.

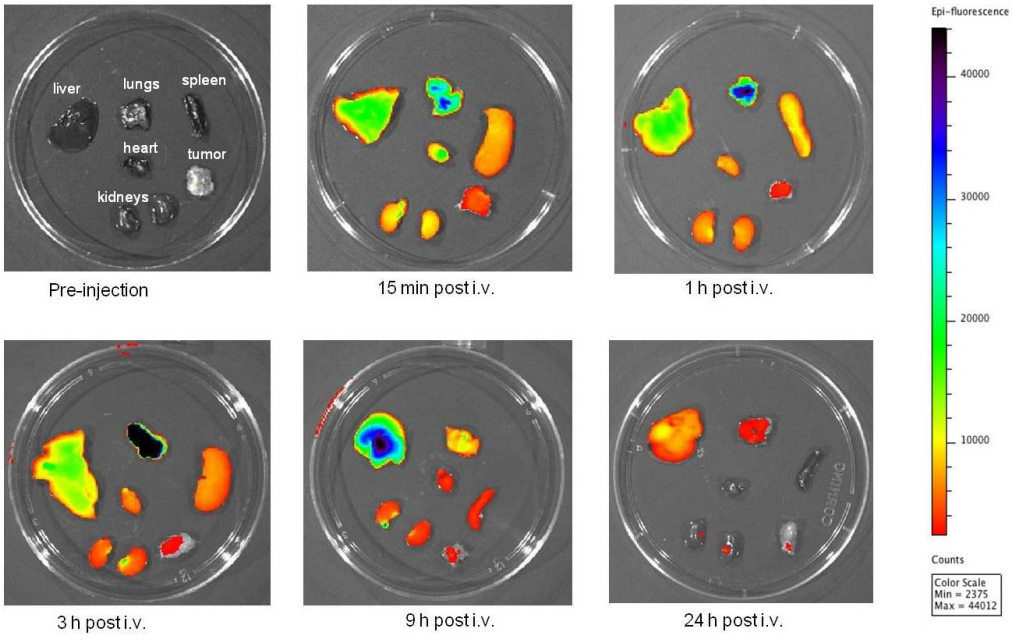


Figure 46. Optical Imaging or excised organs from Balb/C mice bearing subcutaneous colon-26 tumors.

3.3 Whole Body *In Vivo* Imaging

Time dependent in vivo imaging was conducted to monitor the distribution of SBDPiR690 in live mouse (Fig. 47). Whole body imaging with SBDPiR690 displayed clearance by 24 h and highest fluorescence signal at 30 min, this observation lead to the assertion that SBDPiR690 may have minimal skin retention and its maximum concentration for treatment would be at the mentioned time point. The relatively small size and the freely rotating phenyl rings positioned at the periphery of the BODIPY core may influence the observed clearance pattern ex vivo and by whole body imaging with SBDPiR690.

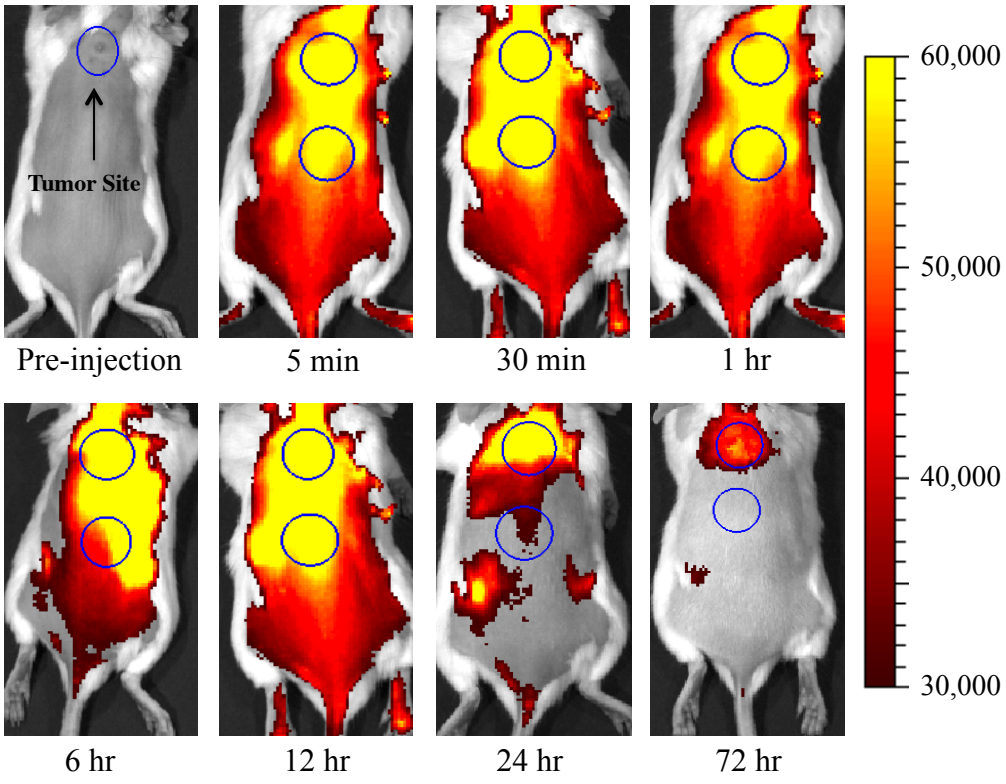


Figure 47. Whole Body Imaging with SBDPiR690.

3.4 Optical Guided SBDPiR690 Photodynamic Therapy

Mice (24 mice) were inoculated with colon 26 cells in the head neck area and tumor growth was monitored with a digital caliper. Two dimensions, l and w (l, the longest axis of tumor; w, the axis perpendicular to l), were used to calculate tumor volume ($lw^2/2$). Stock solutions in DMSO (4 mM) and further dilutions in 1% Tween 80 and 5% dextrose solution to achieve final doses were as follows: Control, SBDPiR690 only, light only, 5 μmol/kg SBDPiR690 + 100 mW cm^{-2} light for 30 min. Samples were filtered using 0.2 μm sterile syringe filter. To each mouse, 200 μL of sample was injected IV (via intraocular injection). After a 15 min of drug administration mice were anesthetized with ketamine 80 mg kg^{-1} and xylazine 6 mg kg^{-1}, by IP injection. Tumors were irradiated with a 690 nm diode laser at 100 mW cm^{-2} for 30 min (180 J cm^{-2}). Tumor size was measured every day after the treatment. Mice recovered after light irradiation and returned to normal activity.

Mice were divided into 4 groups: control (negative control), dark control (SBDPiR690 only), light control (light only), and SBDPiR690-PDT. 200μL of SBDPiR690 (5 μmole/kg) was intravenously injected into the mice, followed by light illumination [690 nm diode laser, 100 mW/cm^2, 30 min (150 J/cm^2)] after 30 min post IV-injection using a 690 nm diode laser. *[This time point was determined by the above whole body images aiming to damage the tumor vasculature]*. While the two positive control groups (either only hv or SBPiR690) did not show any significant tumor growth delay compared to the negative control group, PDT treated group showed dramatic reduction of tumors (Fig. 48). Mass necrosis localized at the tumor region was evident after 24 - 72 hr after the

illumination. An associated edema and inflammation were observed after 24 h, but healed after a few days. Mice were pronounced cured after tissue remodeling with no palpable tumor observed even after 60 days post-treatment (Fig. 50)

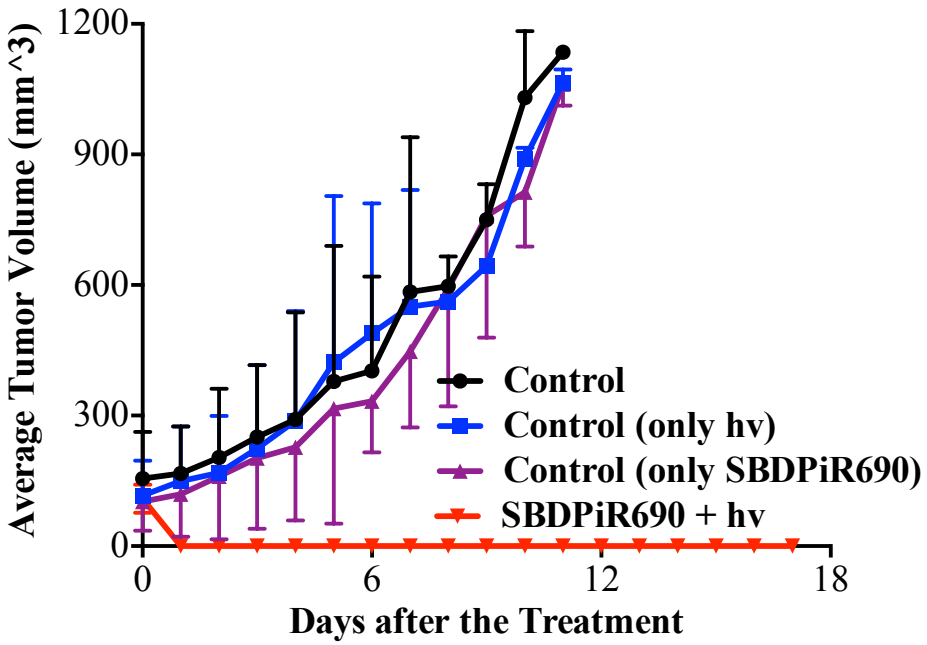


Figure 48. Tumor growth curves in response to various experimental conditions with SBDPiR690 (5 μmole/kg) in Balb/c mice with colon 26 tumor model.

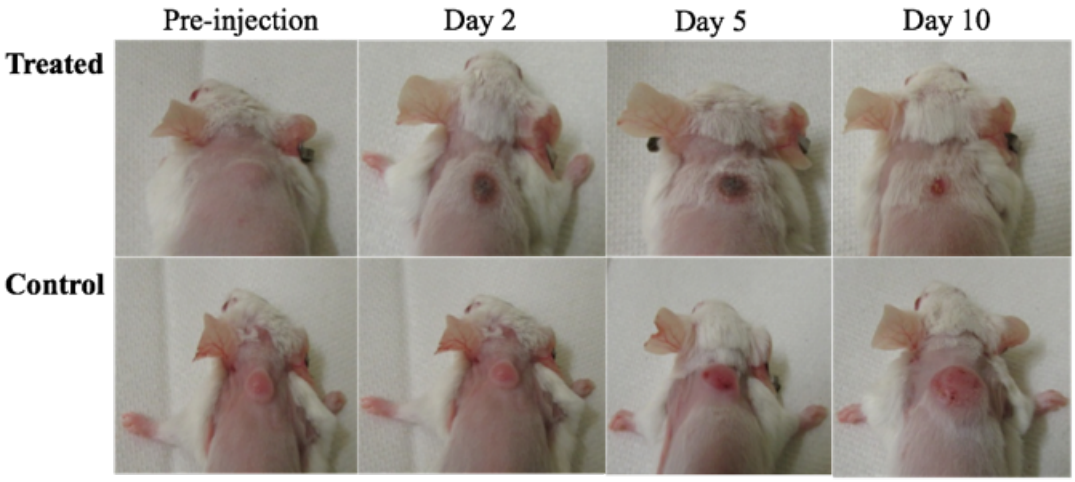


Figure 49. Mouse images post-PDT treatment illustrating antitumor effect of PDT with SBDPiR690 (5 μmole/kg) in Balb/c mice with colon 26 tumor model (n=4).

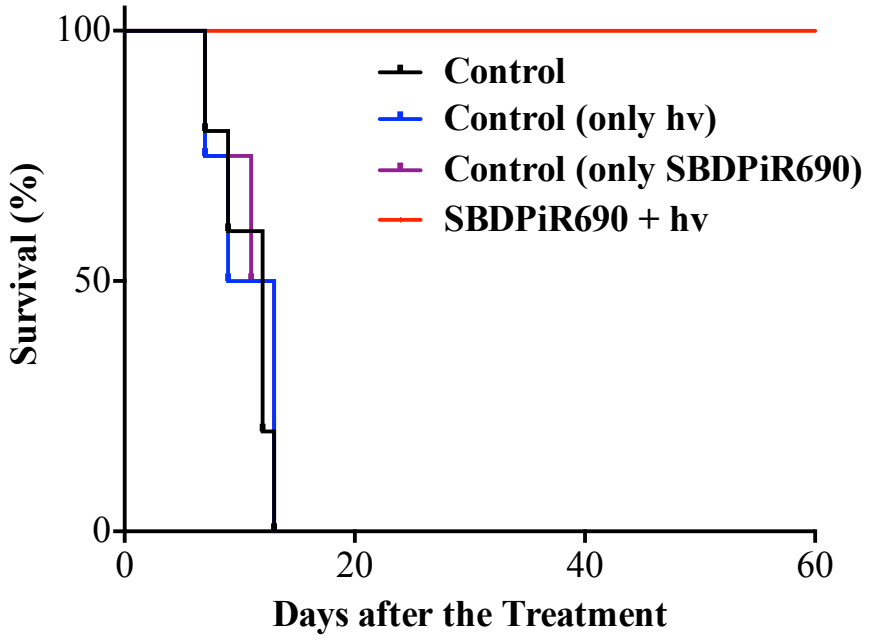


Figure 50. Kaplan-Meier Plot of mouse survival days after PDT treatment with SBDPiR690 (5 μmole/kg) in Balb/c mice with colon 26 tumor model.

3.5 Conclusion

Considering the many non-linear variables of the biological system and PDT, we successfully translate the advantageous bright and phototoxic properties found within test tubes *in vitro* and *in vivo*. Furthermore all analogs are applicable to sub-epithelial tissue due to their NIR absorption (688-700 nm). The coexisting photophysical characteristics permit fusion of photodynamic therapy and diagnosis (theranostics) upon administration of a single photosensitizer for optical guided photodynamic therapy.

We essentially use the brightness of the BODIPY PS to determine a drug-light interval aimed at hemorrhage of the tumor vasculature. Our results potentially revolutionize future design of BODIPY photosensitizers in that (1) NIR absorption can be

accomplished through the extended conjugation without altering π-donor and π-acceptor groups, (2) spin orbit coupling and subsequent ISC can be accomplished without HAE, and (3) dual functioning BODIPY PS possesses characteristics required for fluorescence guided-vascular targeted PDT.

3.6 Experimental Conditions

Assays were performed using colon-26 cells. The specified cell line was obtained from NCI and cultured in Dubelco minimum essential medium (DMEM) supplemented with 10% (v/v) fetal calf serum, 1% (v/v) L-glutamine, 50 U mL^{-1} penicillin, 50 μg mL^{-1} stre22221ptomycin. All cells were maintained in 5 % CO_2 (v/v) and 21 % O_2 (v/v) at 37 °C.

All animal experiments were approved by the Institutional Animal Care and Use Committee (IACUC) at the University of Oklahoma Health Science Center. Four- to six-week-old Balb/c mice (18–20 g, Charles River Laboratories, Inc.) were used for the murine tumor model. The mice were inoculated subcutaneously with 2×10^6 colon 26 cells in PBS (100 μL) on the lower back-neck region. Tumors grew predictably in all mice and reached a size of 5 – 6 mm diameter (tumor growth monitored with a digital caliper). Within 10 – 14 days after the inoculation, mice were used for imaging. For ex vivo bio distribution studies, mice were euthanized and the tumor, liver, lungs, heart, spleen and kidneys were excised and fluorescent images at different time points were taken.

Chapter IV. Functionalization and Photophysics of NIR Dual Functioning Photosensitizers

4.0 Introduction

Surgical resection of cancerous tissue continues to be the most efficient and conventional therapeutic modality. The success of treatment relies on the surgeon's ability to accurately identify tumor lesions. Recognition of malignant disease is currently achieved by two methods. First, the abnormalities of cancerous tissue are visually discernable as masses and nodules and have a contrasting color, distinct morphology, and/or extend beyond the confines of healthy tissue. Second, malignant flat lesions are identified intraoperativly through the assistance of fluorescent probes.[112] Passive targeting of current fluorophores allows selective disease accumulation serving as disease highlighters. The improved contrast between diseased and normal tissue significantly reduce recurrence rate through the removal of otherwise residual cells.[27]

While the above, termed fluorescence guided surgery, has improved therapeutic outcome, the passive diffusion into targets has the disadvantage of background signals complicating the delineation of disease tissue.[33] Furthermore, many of the current probes used for optical guided resection are of the porphyrin scaffold. Porphyrins demonstrate selective accumulation, but the photophysical properties, particularly brightness, are less than optimal. The scientific community has aimed at improving the specificity of porphryins through conjugation of ligands (e.g. folic acid) to fluorescent molecules. These ligands deliver the fluorescent signal directly to over-expressed

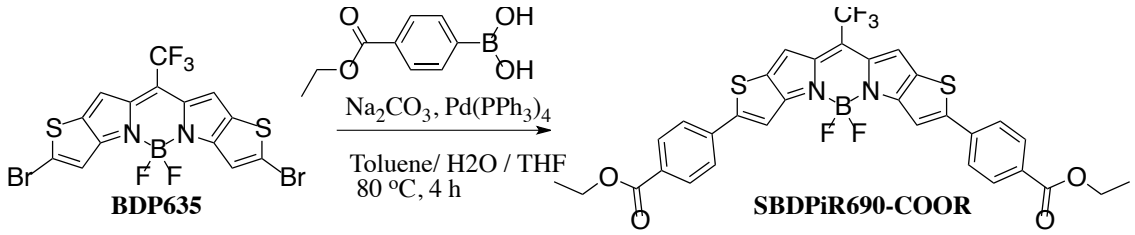
receptors, which limits the background signal and improving the target concentration.[27, 113]

The design dual functioning (bright and phototoxic) NIR BODIPY PS, the application of such exquisite optical properties for surgical guidance is advantageous. The location of malignant tissue is a major determinant of therapeutic choice. The removal of diseased and/or healthy tissue within sensitive organs, specifically the brain, is detrimental to patient quality of life.[27] The designed dual functioning PS potentially allow surgeons to apply the brightness parameter as a guide for marginal resection and eradicate residual disease tissue through the inherent phototoxic power. However, the issue of low target-to-background ratio persists in dual functioning photosensitizers since these are not targeted.

Hence in this chapter we have functionalized our lead and designed analogs with ester functionality at the peripheral and boron center respectively. Upon hydrolysis, the two amendments will improve target concentration and bioavailability through increased water solubility and disruption of symmetry. Importantly, the appropriate functional groups for conjugation to cancer specific ligand were successfully installed.

4.1 Synthesis of Peripheral Functionalized NIR BODIPY SBDPiR690-COOR

The peripheral synthetic strategy installs an ethylcarboxylate at the peripheral position of the thiophene-fused BODIPY core. The approach follows the established design of



Scheme 2. Synthesis of **SBDPiR690-COOR**.

NIR dual functioning PS in that carboxylate groups are moderately deactivating. The synthesis utilizes the BDP635 intermediate as a substrate for Suzuki coupling conditions, yielding the phenyl ester **SBDPiR690-COOR** (Scheme 2). Suzuki coupling reaction conditions were used in the presence of BDP 635 to accomplish the functionalization.

4.2 Optical Properties of SBDPiR690-COOR

The absorption and emission spectra of **SBDPiR690-COOR** exhibits signature sharp absorption characteristic of BODIPY dyes indicative of the $S_0 - S_1$ transition (Fig. 51). The inclusion of the carboxylate group bathochromatically shifts the absorbance maxima from 690 nm to 705 nm. In turn there was a moderate affect to emission maxima (Fig. 52).

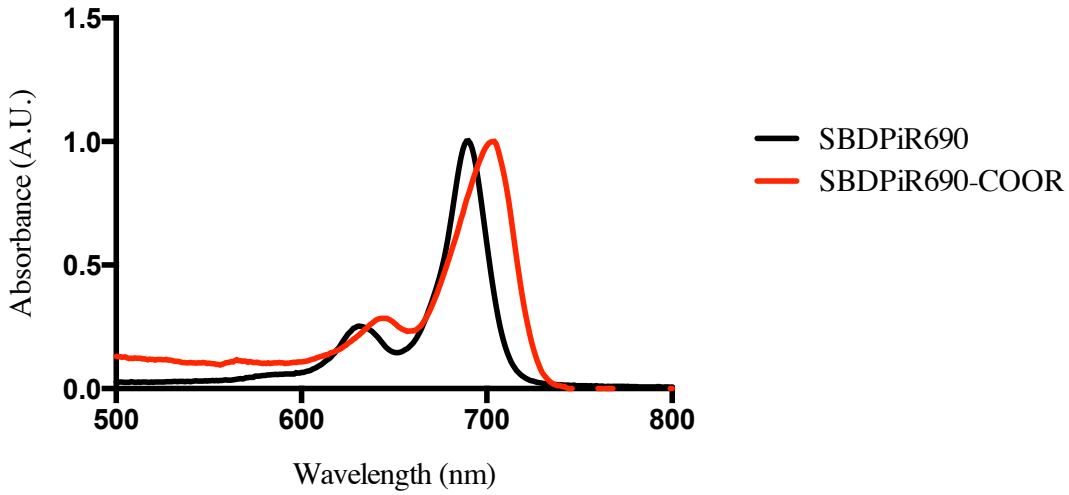


Figure 51. Absorbance comparison of SBDPiR690 and SBDPiR690-COOR.

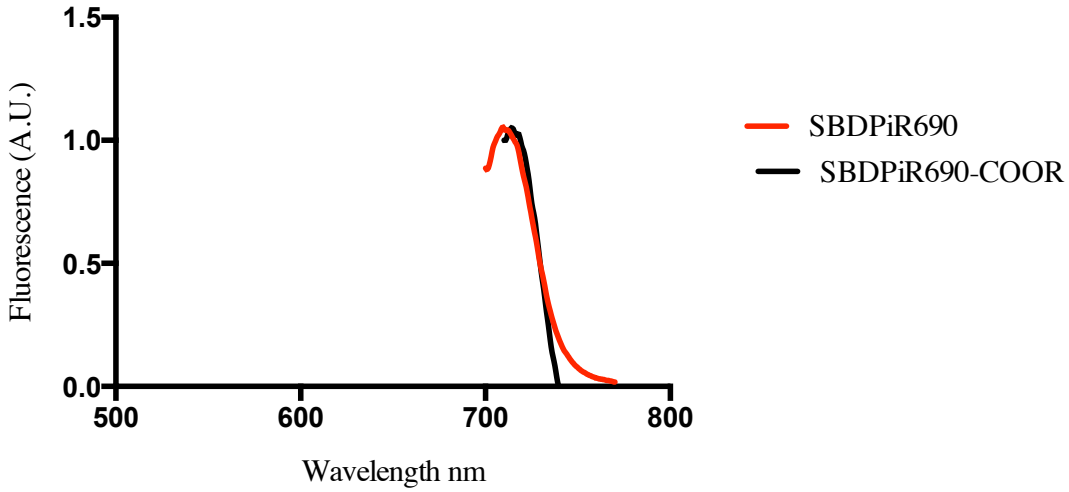


Figure 52. Fluorescence spectra comparison of SBDPiR690-COOR.

4.3 Extinction Coefficient of SBDP690-COOR

Extinction coefficients were determined experimentally. **SBDPiR690-COOR** (ca. 1mg) was dissolved in $CHCl_3$ (5mL) and serially diluted to yield variable concentrations (10^{-6} to 10^{-7}). The absorbance maxima were taken at each concentration and a graph illustrating the slope of absorbance versus concentration was plotted and fitted into Beer-Lambert Law (Fig. 53). The decrease in extinction coefficient from the parent compound was undesired (120,000 $M^{-1}cm^{-1}$), however the determined 71,745 $M^{-1}cm^{-1}$ coefficient is superior to approved PS **(Photofrin** = 5,000 M^{-1} cm^{-1}).

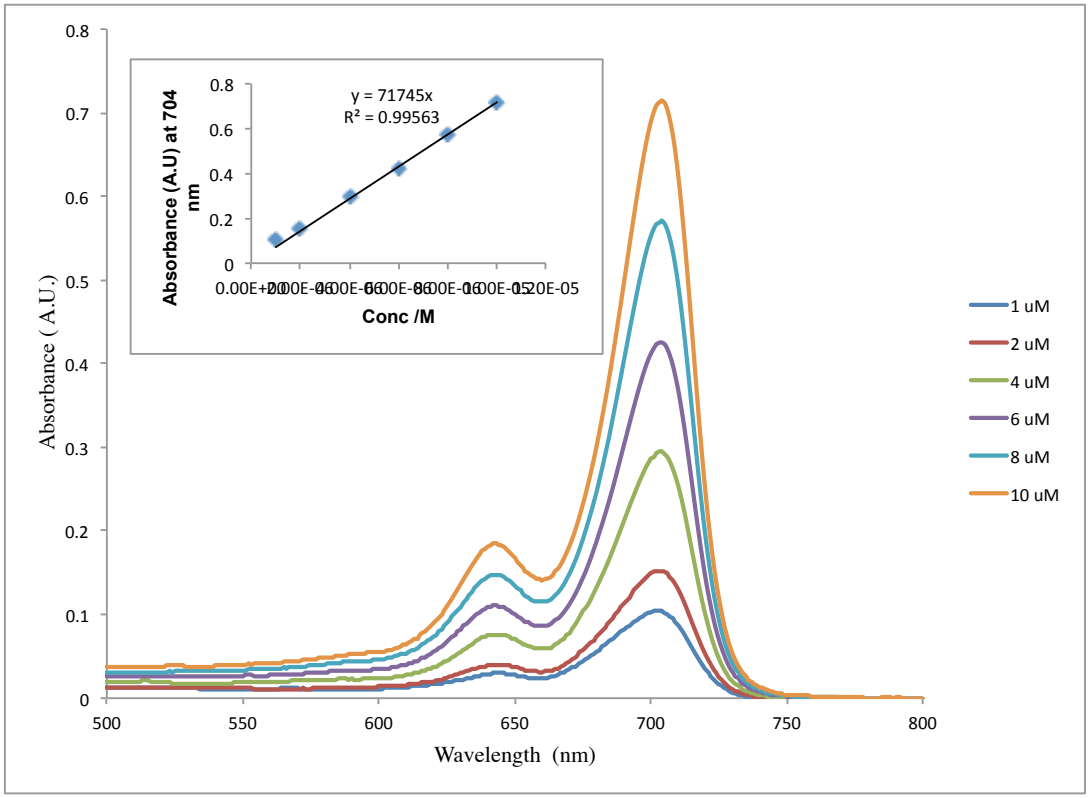


Figure 53. Molar extinction coefficient of SBDPiR690-COOR.

4.4 DPBF Method for Detection of Singlet Oxygen SBDPiR690-COOR

The analogs present were investigated for singlet oxygen generation. Tetrahydrofuran (THF) solutions of **SBDiR690-COORs** were irradiated with broadband light, 400-850 nm, at 0.5 mW/cm^2. Singlet oxygen generation was approximated experimentally through the oxidation of 1,3-diphenylisobenzofuran (DPBF), a known singlet oxygen scavenger.[99a] The presence of reactive oxygen species such as singlet oxygen causes an evident decrease in the DPBF absorbance band at 410 nm. The initial concentrations were 5 x 10^{-6} M of **SBDPiR690** and **SBDPiR690-COOR** along with 90 x 10^{-6} M of **DPBF** over a period of 16 min. The control represents 90 x 10^{-6} M **DPBF** alone in the presence of light. The parent compound **SBDPiR690** was shown in our previous study to have a high singlet oxygen quantum yield (O_{Δ}) of 0.42, and therefore was used as positive control. In reference to the parent compound, **SBDPiR690-COOR** oxidizes **DPBF** higher relative rate of singlet oxygen, 2.8 fold compared to 2.5 fold by **SBDPiR690** (Fig. 54). The ability to incorporate reactive functional groups and maintain the singlet oxygen generation capability was essential for potentially improving the efficacy of **SBDPiR690** through conjugation of target moieties.

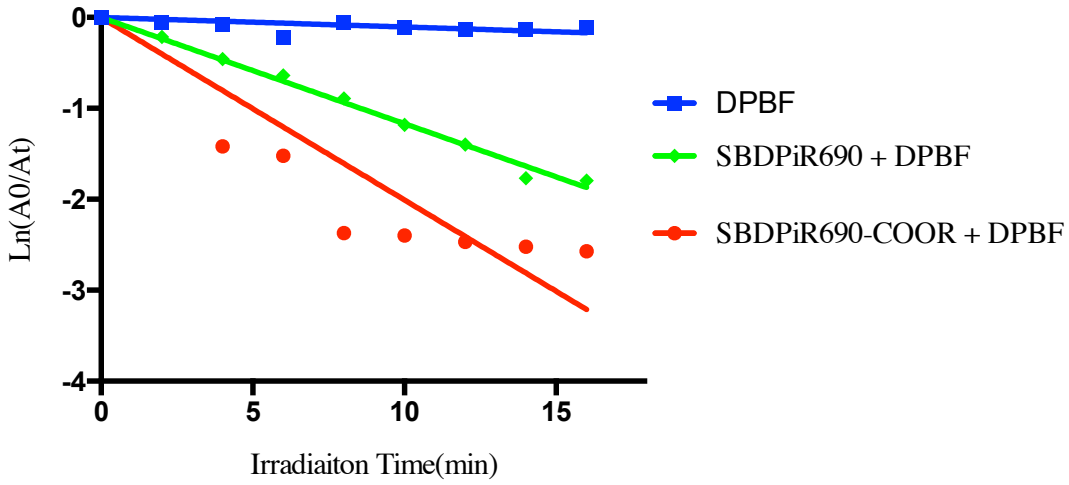


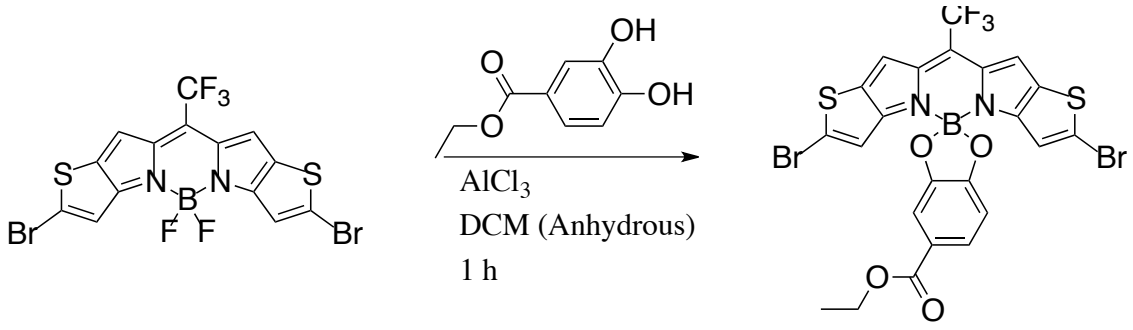
Figure 54. Time-dependent decrease of absorbance (410 nm) by oxidation of DPBF (90 x 10^{-6} M) with **SBDPiR690-COOR** and **SBDPiR690** (5 x 10^{-6} M) under broad band light (400-850 nm at 0.5 mW/cm^2).

4.5 Functionalized Intermediate BDP635-COOR

In attempt to broaden the application of SBDPiRs, we functionalized BDP635 with an ester group, facilitating further conjugation of target specific ligands. The functionalized di-bromo intermediate is a prime substrate for Suzuki coupling reactions. This established platform with absorption of 642 nm allows us to produce various functionalized NIR BODIPY. Moreover the intermediate allows us to apply the established ideology for production of functionalized BODIPY analogs with imaging and therapeutic capability.

Upon obtaining **BDP635** according to the **scheme 2**, a one-pot reaction **BDP635** was solvated in dichloromethane (anhydrous) and degassed with nitrogen. The reaction was

Lewis acid catalyzed by aluminum chloride allowing substitution of the fluoro groups by ethyl 3,4, dihydroxybenzoate in approximately one hour **Scheme 3**.

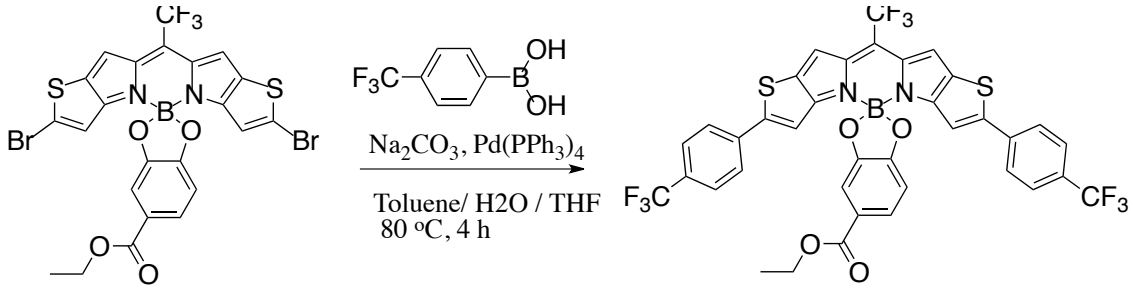


BDP635 **BDP635-COOR**

Scheme 3. Synthesis of **BDP635-COOR**.

4.6 Functionalized Theranostic PS SBDPiR688-COOR

SBDPiR688 analog demonstrates improved Brightness (82,290 M^{-1} cm^{-1}) and Phototoxic Power (99,170 M^{-1} cm^{-1}) in comparison to the lead compound **SBDPiR690**, 26, 400 and 50,400 $M^{-1}cm^{-1}$ respectively. We therefore used our functionalized intermediate to produce the functionalized **SBDPiR688-COOR** derivative (Scheme 4). In a one-pot reaction, **BDP635-COOR**, trifluoromethylphenyl boronic acid, and Na_2CO_3 were dissolved in a biphasic mixture of THF, water, and toluene and allowed to stir under nitrogen. Palladium tetrakis-triphenyl phosphine was used to catalyze the reaction under reflux for 3h, yielding **SBDPiR688-COOR**.



BDP635-COOR **SBDPiR688-COOR**

Scheme 4. Synthesis of SBDPiR688-COOR.

4.7 Optical Properties of SBDPiR688-COOR

In comparison to the parent compound the optical properties (absorbance and fluorescence) were shifted bathochromatically (Fig. 55). This was expected as the conjugation of the molecule was extended. The extinction coefficient was reduced **SBDPiR688** (211,000 M^{-1} cm^{-1}) and **SBDPiR688-COOR** (197,202 M^{-1} cm^{-1}) (Fig. 56), but very much appreciable in comparison to current approved PS (**Photofrin** 5,000 M^{-1} cm^{-1}).

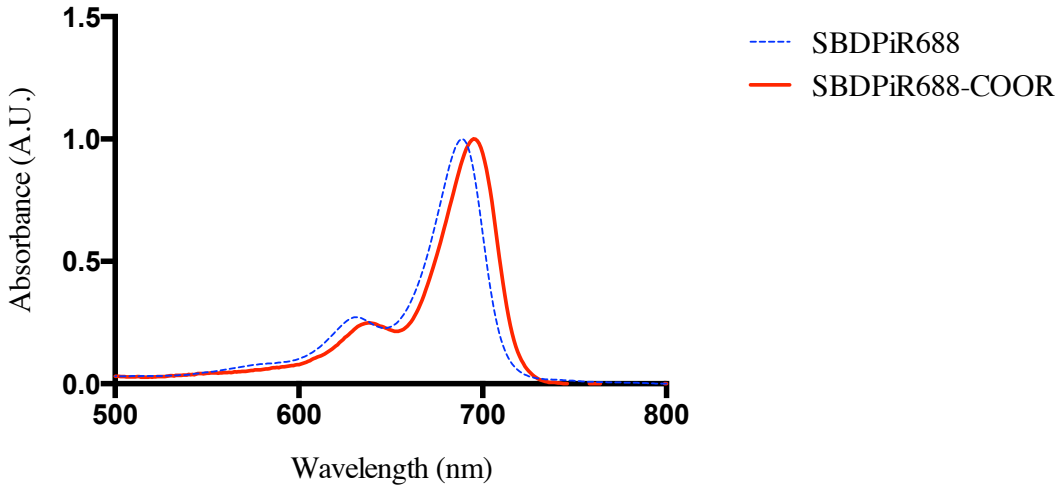


Figure 55. Absorbance spectra comparison of SBDPiR688 and SBDPiR688-COOR.

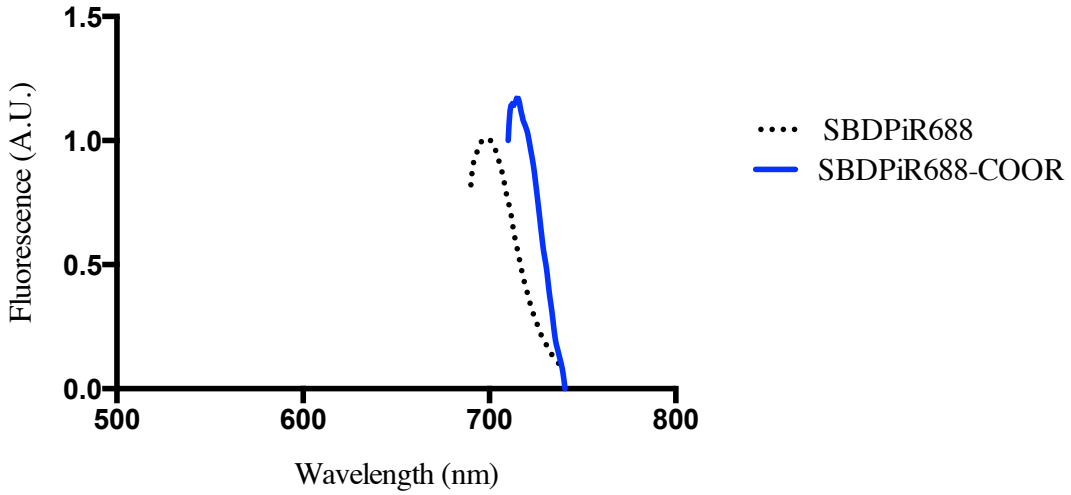


Figure 56. Fluorescence spectra comparison of SBDPiR688 and SBDPiR688-COOR.

4.8 Extinction Coefficient of SBDPiR688-COOR

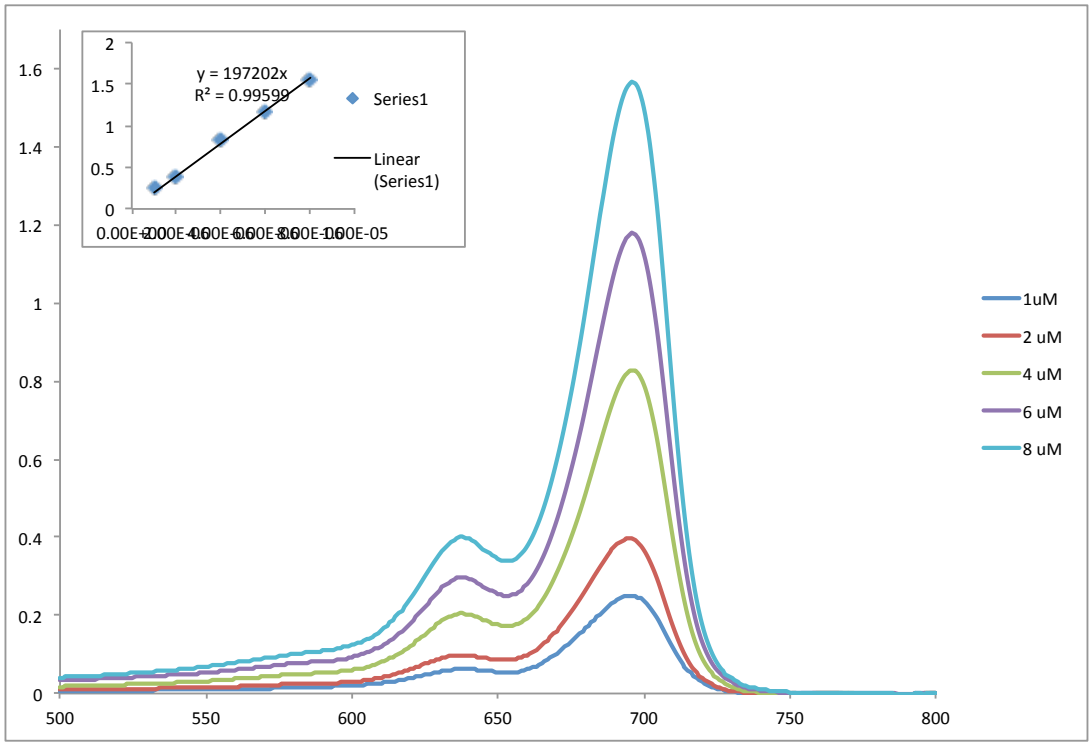


Figure 57. Molar Extinction Coefficient of SBDPiR688-COOR.

4.9 DPBF Method for Detection of Singlet Oxygen of SBDPiR688-COOR

The determination of singlet oxygen generation was performed according to procedures mentioned above. The parent compound **SBDPiR688** was our most efficient singlet oxygen generator. Ability to include functionality and maintain these dual functioning properties would be essential in furthering its application for target specific PDT. However, modification of the BODIPY core altered the photophysics to exclude singlet oxygen generating capabilities (Fig. 58). The structure photophysical property study revealed the importance of the HOMO LUMO gap ranging at or above 1.5 to achieve appreciable singlet oxygen generation. The resonance contribution of oxygen affects the

HOMO LUMO energy levels, hypothetically. A more detail investigation into the actual energy gap of **SBDPiR688-COOR** would offer concrete evidence for our hypothesis.

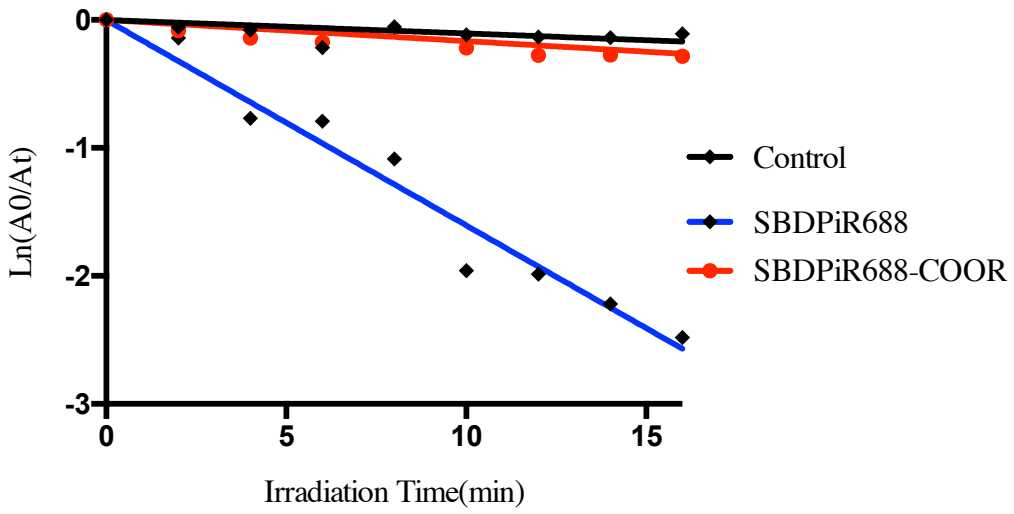


Figure 58. Time-dependent decrease of absorbance (410 nm) by oxidation of DPBF (90 x 10^{-6} M) with **SBDPiR688-COOR** and **SBDPiR688** (5 x 10^{-6} M) under broadband light (400-850 nm at 0.5 mW/cm^2).

4.0.1 Conclusion

While substitution at the boron center is advantageous for increased aqueous solubility and allows functionalization of improved dual functioning analogs, the replacement of fluorine affects the singlet oxygen generating capability. Therefore, modification at the peripheral is a valid method for functionalization of the newly designed molecules. Upon conversion to the carboxylic acid, **SBDPiR690-COOR** can be tethered to desired targets for imaging and therapeutic usage.

4.0.2 Experimental and General Methods

4.0.3 (SBDPiR690-COOR) 2,8-Bis(4-(ethoxycarbonyl)phenyl)-5,5-difluoro-11-(trifluoromethyl)-5H-thieno[2',3':4,5]pyrrolo[1,2-c]thieno[2',3':4,5]pyrrolo[2,1-f][1,3,2]diazaborinin-4-ium-5-uide: **BDP635** (0.100 g, 0.190 mmol) was synthesized according to Scheme 1 and dissolved in toluene, tetrahydrofuran, water (30 mL 1:1:1). Commercially available 4-ethoxycarbonylphenyl boronic acid (0.109 g, 0.515 mmol) and Na_2CO_3 (0.080 g, 0.756 mmol) was added and the reaction was purged with nitrogen gas for 10 min. $Pd(PPh_3)_4$ (0.022 g, check this wt ~5 mol %) was used to catalyzed the reaction at 80 °C for 2-3 h. Upon completion, the reaction was diluted with 10 mL water and extracted with toluene. The combined organic layer was washed with water and brine (100 mL each) and dried over anhydrous Na_2SO_4. The dried mixture was purified by silica-gel column chromatography (1:99) hexanes:toluene) to afford **SBDPiR690-COOR** as a dark green solid (0.028 g, 22%). ^{1}H NMR (300 MHz, CD_2Cl_2) δ 1.14 (t, J = 6.9 Hz, 3H), 4.41 (q, 2H), 7.42 (s, 1H), 7.53 (s, 1H), 7.85 (d, J =

8.4 Hz, 2H), 8.13 (d, J = 8.6 Hz, 2H). HRMS EI (m/z): calculated for $C_{32}H_{22}BF_5N_2O_4S_2$ 668.1034; found 668.1010 [M]+.

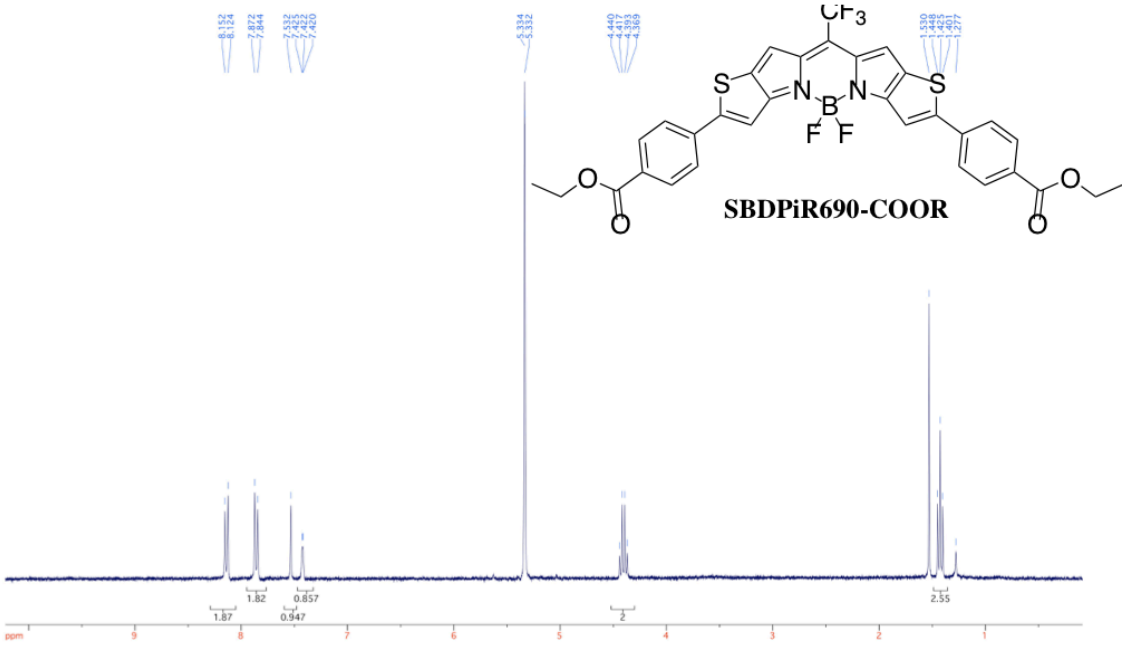


Figure 59. ^{1}H NMR of **SBDPiR690-COOR**.

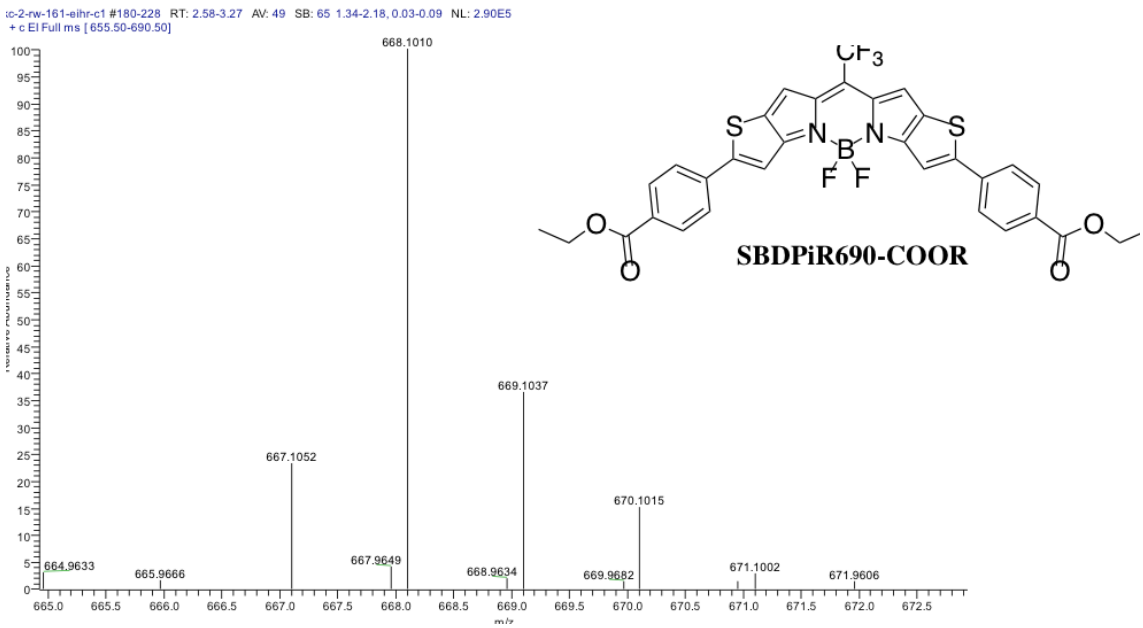


Figure 60. HRMS EI of **SBDPiR690-COOR**.

4.0.4 (BDP635-COOR) 2',8'-Dibromo-5-(ethoxycarbonyl)-11'-(trifluoromethyl)spiro [benzo[d][1,3,2]dioxaborole-2,5'- thieno[2',3':4,5]pyrrolo[1,2-c]thieno [2',3':4,5]pyrrolo [2,1-f][1,3,2]diazaborinin]-4'-ium-12-uide: **BDP635** (0.050g, 0.094 mmol) was dissolved in dry dichloromethane (20 mL) and stirred under argon for 20 min. Then $AlCl_3$ (0.062 g, 0.466 mmol) was added and the solution was further stirred for 15 min before addition of ethyl 3,4-dihydroxybenzoate (0.085 g, 0.467 mmol). The mixture was stirred for 20 min and the solvent was evaporated under reduced pressure. The crude product was purified on silica gel with CH_2Cl_2/ Hexanes 1:1 to give a brown solid **BDP635-COOR** (0.027 g, 42%). ^{1}H NMR (300 MHz, CD_2Cl_2) δ 1.31 (t, J = 7.0 Hz, 3H), 4.27 (q, 2H), 6.19 (s, 1H), 6.78 (d, J = 8.1 Hz, 1H), 7.32 (s, 1H), 7.42 (s, 1H), 7.61 (d, J = 8.1 Hz, 1H). HRMS EI (m/z): calculated for $C_{32}H_{22}BF_5N_2O_4S_2$ 671.8630; found 671.8632 [M]+.

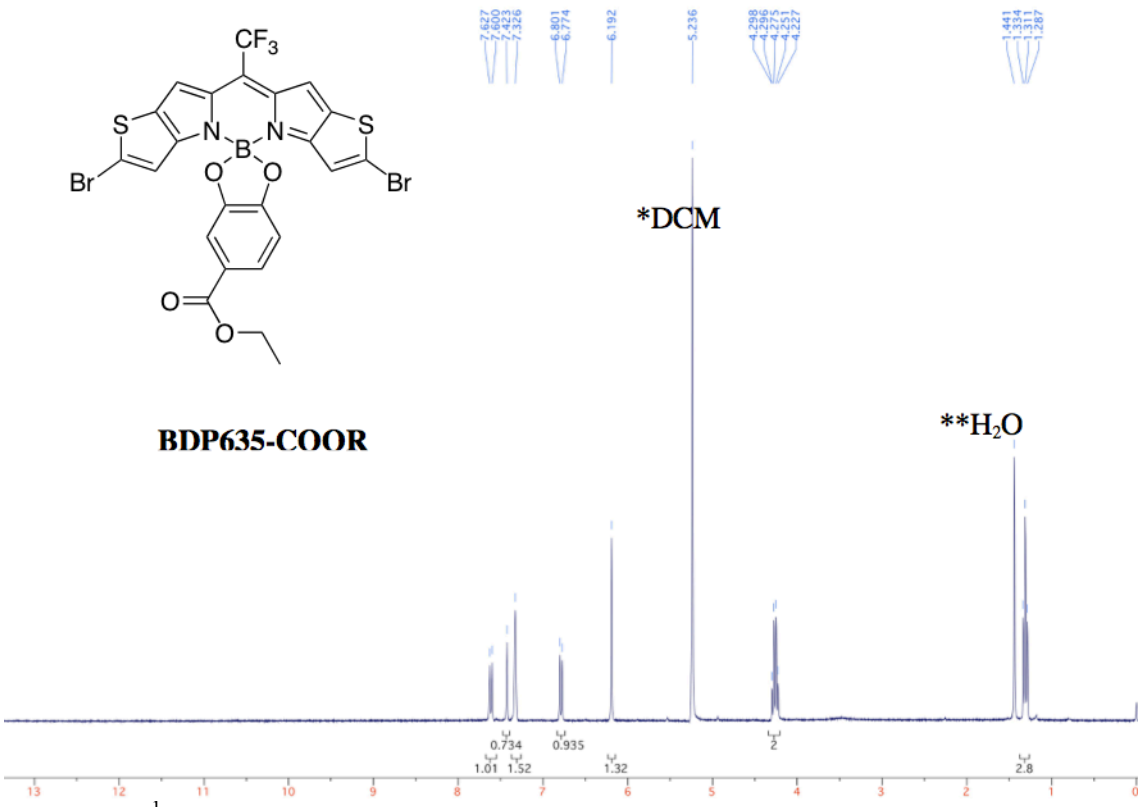


Figure 61. ^{1}H NMR of **BDP635-COOR**.

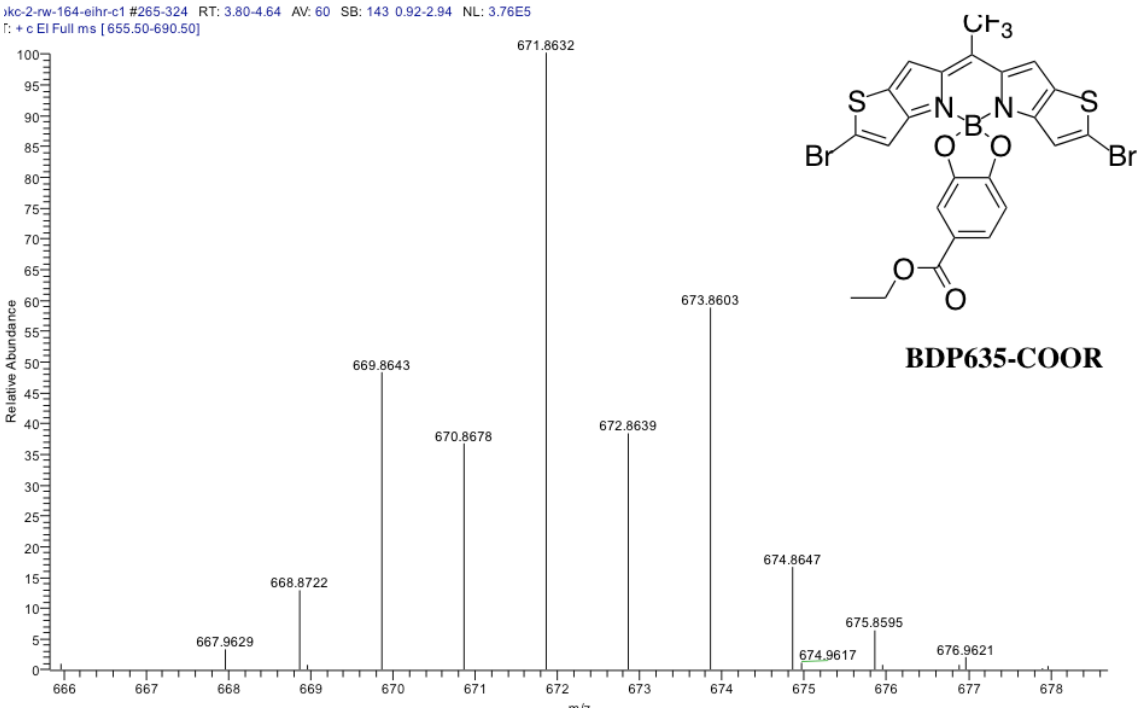


Figure 62. HRMS EI of **BDP635-COOR**.

4.0.5 (SBDPiR688-COOR) 5-(Ethoxycarbonyl)-11'-(trifluoromethyl)-2',8'-bis(4-(trifluoromethyl) phenyl) spiro[benzo[d][1,3,2]dioxaborole-2,5'-thieno[2',3':4,5]pyrrolo[1,2-c]thieno [2',3':4,5]pyrrolo[2,1-f][1,3,2]diazaborinin]-4'-ium-12-uide: To a solution of **BDP635-COOR** (0.050 g, 0.094 mol) in toluene, tetrahydrofuran, water (15mL 1:1:1) was added 4-trifluormethylphenylboronic acid (0.042 g, 0.223 mmol), Na_2CO_3 (0.031 g, 0.298 mmol). The reaction was purged with nitrogen gas for 10 min. A catalytic amount of $[Pd(PPh_3)_4]$ (0.010 g,(~10 mol %) was added and the reaction was heated to 80 ºC for 2-3 h. After completion of the reaction as judged by TLC, the reaction was diluted with 10 mL water and extracted with toluene. The combined organic layer was washed with water and brine (100 mL each) and dried over anhydrous Na_2SO_4. The dried mixture was purified by silica-gel column chromatography (60:40) hexanes:toluene) to afford **SBDPiR88-COOR** as a dark green solid (0.018 g, 30%). ^{1}H NMR (300 MHz, CD_2Cl_2) δ= 1.41 (t, *J* = 7.0 Hz, 3H), 4.40(q, 2H), 6.56 (s, 2H), 6.96 (d, *J* = 8.1 Hz, 1H), 7.50 (s, 1H), 7.58 (s, 1H), 7.60 (s, 2H), 7.65 (s, 2H), 7.67 (s, 1H), 7.8 (d, *J*=6.6, 1H). HRMS EI (m/z): calculated for calculated for $C_{37}H_{20}BF_9N_2O_4S_2$ 802.0814; found 802.0834 [M]+.

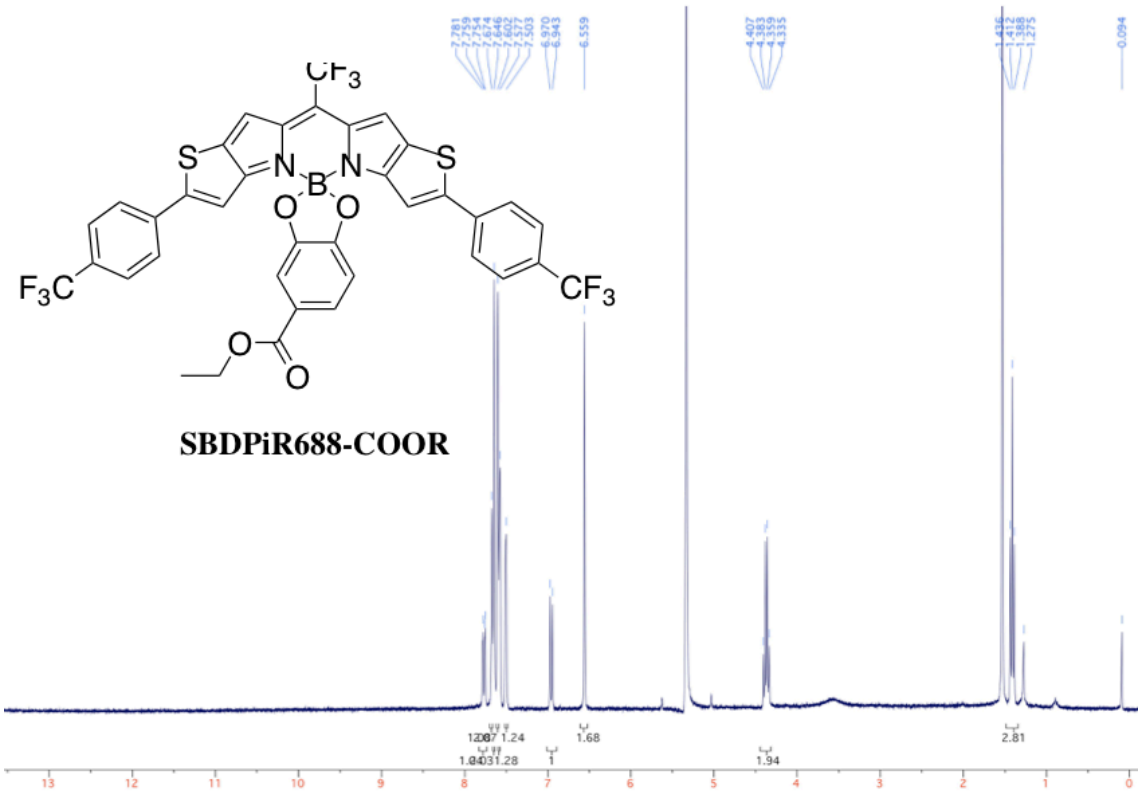


Figure 63. ^{1}H NMR of **SBDPiR688-COOR**.

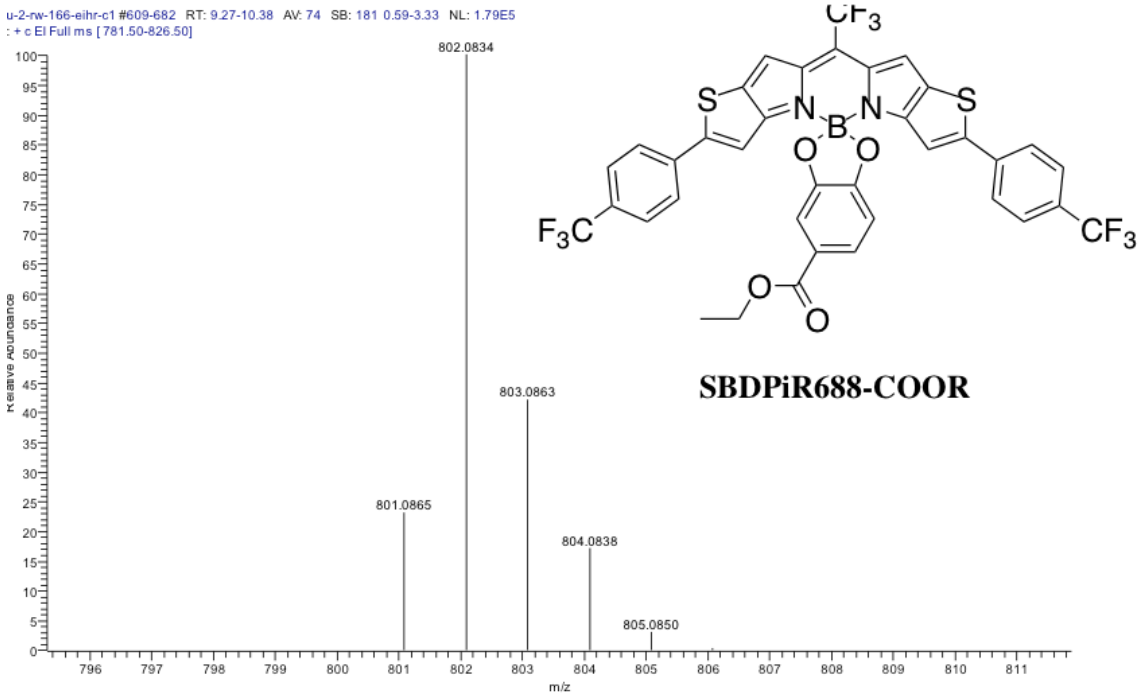


Figure 64. HRMS EI of **SBDPiR688-COOR**

Chapter V. Conclusion and Perspective

The ability to image and treat intact malignant tissue non-invasively is an emerging modality. Preclinical and clinical investigations reveal the advantages of fluorescence imaging and PDT for dependable prognosis and curing of disease, specifically cancer. The clinical slow progression of fluorescence imaging and PDT is a result of the difficulty in optimizing the variable components of PDT for treatment. Furthermore, the currently approved light sources and photosensitizers, while effective, do not illustrate stark improvements in comparison to conventional treatments (chemotherapy and radiotherapy). To further the mainstream expansion of theranostic PDT, efficient NIR absorbing fluorescent photosensitizers are needed.

The ideal agent should possess 1) sharp absorption and emission bands, 2) a high molar extinction coefficient, 3) appreciable singlet oxygen and fluorescence quantum yields, and 4) reactivity for functionalization. Currently approved PSs lack these characteristics, which limits their application to surface malignancies. Furthermore, development remains focused on the design of separate imaging and therapeutic agents for the accomplishment of two objectives. The combination of imaging and therapy in one setting is known as theranostics. The fusion of the two modalities offers imaging and monitoring of diseased tissue, biodistribution, and therapeutic efficacy. Further development includes the ability to fine tune therapy and dose amidst application. Also, the ability to characterize tissue pre, during, and post treatment will offer a patient personalized therapeutic approach for disease.

In this dissertation, the design, synthesis, and application of NIR dual functioning BODIPY analogs serve to: 1) understand the contributing factors for yielding both appreciable fluorescence and singlet oxygen quantum yields in the versatile BODIPY PS and 2) effectively apply the brightness for imaging of bio distribution for determining the optimal drug light interval for vascular targeting photodynamic therapy. NIR BODIPY dyes (imaging agents) are primarily achieved through extended conjugation of the core in addition to possessing a donor-π-acceptor system. With these in place NIR BODIPY dyes can be converted to photosensitizers (photodynamic agents) through inclusion of heavy atoms such as bromine and iodine, chemically inducing intersystem crossing. However, this method significantly diminishes the fluorescence quantum yield, brightness, and overall imaging capability.

The dissertation successfully demonstrates NIR absorbing BODIPY analogs through fusion of the pyrrole and thiophene rings proceeding carbon-carbon coupling of the thiophene moiety to phenyl rings. The methodology is unique in that we exclude the donor-π-acceptor acceptor principle, which prevents the production of singlet oxygen without heavy atom assistance. Incorporation of neutral to electron-withdrawing groups facilitates a theranostic approach with brighter photodynamic NIR agents.

While the present photosensitizers are rare in their dual functionality, the agents are not without limitation. As seen in our whole body images, the current molecules exhibit non-specific distribution. The brief localization of the drug is a result of low-density lipophilic proteins acting as a carrier to the tumor site and home via the enhance

permeation and retention effect associated with passive diffusion of malignant tissue.[47] Therefore our agents, while effective, lack distinct selectivity as with conventional therapy methods. We used the brightness to determine the appropriate irradiation time, but the methodology of vascular targeting through short (15 to 30 min) drug light intervals has been firmly established within the PDT community.[110-111]

The purpose of tumor vascular targeting is to selectively alter the tumor vasculature. The vasculature is a prime target in that disrupting the circulatory function shutdowns nutrient supply and moreover eliminates its means of spreading cancer cells to nearby healthy organs and tissue. Efforts to incorporate carboxylate synthons facilitate a solution to the selectivity issue. However, while various vascular markers have shown to be overexpressed, an absolute biomarker for tumor vasculature has yet to be discovered. Furthermore, conjugation of BODIPY potentially alters the natural pharmacokinetics of target ligands and resulting in extensive circulation and low clearance rates. These together result in dark toxicity and affect imaging efficacy due to increased background signals.[114]

In the event an absolute marker is discovered, the optimal PS would not only be NIR targeted but exists as a quenched precursor that is activated at the target site. This approach allows significant target-to-background ratios.[55] Otherwise an extensive structure activity relationship would be advantageous for locating the optimal hydrophobicity for increasing selective uptake and photosensitizing efficacy. This

particular SAR was key for identifying structure modification of porphryin-based scaffolds.[96]

PDT has been approved for more than 25 years in respect to oncology; however, is not exercised as a mainstream therapy. This is in part due to the above facts. Overall, the capacities in which established drug light combinations have been applied (i.e. photodynamic therapy) hold no clear advantage over conventional therapies. As with our dual functioning PS, advancements have only been successful at demonstrating the viability of photodynamic therapy. Furthermore, failure to establish optimal routine variables for the multifaceted PDT dissuades clinicians' interests.[49c] However, it is the multi components that enforce a personalized approach, which is vital for treating the evolving disease of cancer.

References

1. Umar, A.; Dunn, B. K.; Greenwald, P., Future directions in cancer prevention. *Nat Rev Cancer* **2012,** *12* (12), 835-848.
2. Donna Hoyert, J. X., Deaths: Preliminary Data for 2011. *National Vital Statistics Reports* **2012,** *61* (6), p. 4
3. Bode, A. M.; Dong, Z. G., Cancer prevention research - then and now. *Nat Rev Cancer* **2009,** *9* (7), 508-516.
4. Lander, E. S., Initial impact of the sequencing of the human genome. *Nature* **2011,** *470* (7333), 187-197.
5. Barrett, J. C.; Wiseman, R. W., Cellular and Molecular Mechanisms of Multistep Carcinogenesis - Relevance to Carcinogen Risk Assessment. *Environ Health Persp* **1987,** *76*, 65-70.
6. Barrett, J. C., Mechanisms of Multistep Carcinogenesis and Carcinogen Risk Assessment. *Environ Health Persp* **1993,** *100*, 9-20.
7. Fitzakerley, J. 2014 Antineoplastics http://www.d.umn.edu/~jfitzake/Lectures/DMED/Antineoplastics/GeneralConcepts/CellKillHypothesis.html.
8. Control, C. f. D. Leading Causes of Death. http://www.cdc.gov/nchs/fastats/leading-causes-of-death.htm (accessed December 31, 2014).
9. Bertram Katzung, S. M., Anthony trevor *Basic and Clinical Pharmacology* McGraw Hill Professionall 2012.
10. Frangioni, J. V., New technologies for human cancer imaging. *J Clin Oncol* **2008,** *26* (24), 4012-4021.
11. Brindle, K., New approaches for imaging tumour responses to treatment. *Nat Rev Cancer* **2008,** *8* (2), 94-107.
12. Fass, L., Imaging and cancer: A review. *Mol Oncol* **2008,** *2* (2), 115-152.
13. Conway, J. R. W.; Carragher, N. O.; Timpson, P., Developments in preclinical cancer imaging: innovating the discovery of therapeutics. *Nat Rev Cancer* **2014,** *14* (5), 314-328.
14. Albert, F. K.; Forsting, M.; Sartor, K.; Adams, H. P.; Kunze, S., Early postoperative magnetic resonance imaging after resection of malignant glioma: objective evaluation of residual tumor and its influence on regrowth and prognosis. *Neurosurgery* **1994,** *34* (1), 45-60; discussion 60-1.
15. Greco, C.; Wolden, S., Current status of radiotherapy with proton and light ion beams. *Cancer* **2007,** *109* (7), 1227-38.
16. Bergh, J., Quo vadis with targeted drugs in the 21st century? *J Clin Oncol* **2009,** *27* (1), 2-5.

17. Hay, M.; Thomas, D. W.; Craighead, J. L.; Economides, C.; Rosenthal, J., Clinical development success rates for investigational drugs. *Nature Biotechnol* **2014,** *32* (1), 40-51.

18. Dougherty, T. J., Hematoporphyrin as a Photosensitizer of Tumors. *Photochem Photobiol* **1983,** *38* (3), 377-379.

19. Kennedy, J. C.; Pottier, R. H.; Pross, D. C., Photodynamic Therapy with Endogenous Protoporphyrin .9. Basic Principles and Present Clinical-Experience. *J Photoch Photobio B* **1990,** *6* (1-2), 143-148.

20. Pushpan, S. K.; Venkatraman, S.; Anand, V. G.; Sankar, J.; Parmeswaran, D.; Ganesan, S.; Chandrashekar, T. K., Porphyrins in photodynamic therapy - a search for ideal photosensitizers. *Curr Med Chem Anticancer Agents* **2002,** *2* (2), 187-207.

21. Ethirajan, M.; Chen, Y.; Joshi, P.; Pandey, R. K., The role of porphyrin chemistry in tumor imaging and photodynamic therapy. *Chem Soc Rev* **2011,** *40* (1), 340-62.

22. Lavis, L. D.; Raines, R. T., Bright ideas for chemical biology. *ACS Chem Biol* **2008,** *3* (3), 142-155.

23. Loudet, A.; Burgess, K., BODIPY dyes and their derivatives: syntheses and spectroscopic properties. *Chem Rev* **2007,** *107* (11), 4891-932.

24. Ulrich, G.; Ziessel, R.; Harriman, A., The chemistry of fluorescent bodipy dyes: versatility unsurpassed. *Angew Chem Int Ed Engl* **2008,** *47* (7), 1184-201.

25. Awuah, S. G.; You, Y., Boron dipyrromethene (BODIPY)-based photosensitizers for photodynamic therapy. *Rsc Adv* **2012,** *2* (30), 11169-11183.

26. Allison, R. R.; Moghissi, K., Oncologic photodynamic therapy: Clinical strategies that modulate mechanisms of action. *Photodiagn Photodyn* **2013,** *10* (4), 331-341.

27. Celli, J. P.; Spring, B. Q.; Rizvi, I.; Evans, C. L.; Samkoe, K. S.; Verma, S.; Pogue, B. W.; Hasan, T., Imaging and photodynamic therapy: mechanisms, monitoring, and optimization. *Chem Rev* **2010,** *110* (5), 2795-838.

28. Dolmans, D. E. J. G. J.; Fukumura, D.; Jain, R. K., Photodynamic therapy for cancer. *Nat Rev Cancer* **2003,** *3* (5), 380-387.

29. Robertson, C. A.; Evans, D. H.; Abraharnse, H., Photodynamic therapy (PDT): A short review on cellular mechanisms and cancer research applications for PDT. *J Photoch Photobio B* **2009,** *96* (1), 1-8.

30. Dougherty, T. J.; Gomer, C. J.; Henderson, B. W.; Jori, G.; Kessel, D.; Korbelik, M.; Moan, J.; Peng, Q., Photodynamic therapy. *J Natl Cancer I* **1998,** *90* (12), 889-905.

31. Brancaleon, L.; Moseley, H., Laser and non-laser light sources for photodynamic therapy. *Lasers Med Sci* **2002,** *17* (3), 173-86.

32. Wilson, B. C.; Patterson, M. S., The physics, biophysics and technology of photodynamic therapy. *Phys Medi Biol* **2008,** *53* (9), R61-109.

33. Kobayashi, H.; Ogawa, M.; Alford, R.; Choyke, P. L.; Urano, Y., New Strategies for Fluorescent Probe Design in Medical Diagnostic Imaging. *Chem Rev* **2010,** *110* (5), 2620-2640.

34. *al,* V. K. *e.*, Solid state lasers for photodynamic therapy of the malignant neoplasm. *Proceeding of SPIE* **2002,** *4615*.

35. Varma, S.; Wilson, H.; Kurwa, H. A.; Gambles, B.; Charman, C.; Pearse, A. D.; Taylor, D.; Anstey, A. V., Bowen's disease, solar keratoses and superficial basal cell carcinomas treated by photodynamic therapy using a large-field incoherent light source. *Brit J Dermatol* **2001,** *144* (3), 567-574.

36. Ericson, M. B.; Wennberg, A. M.; Larko, O., Review of photodynamic therapy in actinic keratosis and basal cell carcinoma. *Ther Clin Risk Manag* **2008,** *4* (1), 1-9.

37. Lim, H. S., Development and optimization of a diode laser for photodynamic therapy. *Laser Therapy* **2011,** *20* (3), 195-203.

38. Schmidt, R., Photosensitized generation of singlet oxygen. *Photochem Photobiol* **2006,** *82* (5), 1161-1177.

39. Schweitzer, C.; Schmidt, R., Physical mechanisms of generation and deactivation of singlet oxygen. *Chem Rev* **2003,** *103* (5), 1685-1757.

40. Andrews, L. J.; Abrahams.Ew, Formation of O2sigma+-1(G) by 1-Fluoronaphthalene Sensitization. *Chem Phys Lett* **1971,** *10* (2), 113-&.

41. Schmidt, R.; Bodesheim, M., Efficiencies of O2((1)Sigma(G)(+)) and O2((1)Delta(G)) Formation in the Primary Steps of Triplet-State Photosensitization in Solution. *Chem Phys Lett* **1993,** *213* (1-2), 111-116.

42. Prasad, P. N., *Introdcution to Biophotonics* John Wiley & Sons 2003. p.112

43. (a) Gorman, A. A.; Hamblett, I.; Lambert, C.; Prescott, A. L.; Rodgers, M. A. J.; Spence, H. M., Aromatic Ketone Naphthalene Systems as Absolute Standards for the Triplet-Sensitized Formation of Singlet Oxygen, O-2(1-Delta-G), in Organic and Aqueous-Media - a Time-Resolved Luminescence Study. *J Am Chem Soc* **1987,** *109* (10), 3091-3097; (b) Niedre, M.; Patterson, M. S.; Wilson, B. C., Direct near-infrared luminescence detection of singlet oxygen generated by photodynamic therapy in cells in vitro and tissues in vivo. *Photochem Photobiol* **2002,** *75* (4), 382-391.

44. (a) Kraljic, I.; Mohsni, S. E., New Method for Detection of Singlet Oxygen in Aqueous-Solutions. *Photochem Photobiol* **1978,** *28* (4-5), 577-581; (b) AmatGuerri, F.; Lempe, E.; Lissi, E. A.; Rodriguez, F. J.; Trull, F. R., Water-soluble 1,3-diphenylisobenzofuran derivatives. Synthesis and evaluation as singlet molecular oxygen acceptors for biological systems. *J Photoch Photobio A* **1996,** *93* (1), 49-56.

45. Lipson, R. L.; Baldes, E. J.; Olsen, A. M., Use of a Derivative of Hematoporphyrin in Tumor Detection. *J Natl Cancer I* **1961,** *26* (1), 1-&.

46. Dougherty, T. J.; Grindey, G. B.; Weishaupt, K. R., Photoradiation Therapy of Animal Tumors. *P Am Assoc Canc Res* **1975,** *16* (Mar), 29-29.

47. Agostinis, P.; Berg, K.; Cengel, K. A.; Foster, T. H.; Girotti, A. W.; Gollnick, S. O.; Hahn, S. M.; Hamblin, M. R.; Juzeniene, A.; Kessel, D.; Korbelik, M.; Moan, J.; Mroz, P.; Nowis, D.; Piette, J.; Wilson, B. C.; Golab, J., Photodynamic Therapy of Cancer: An Update. *CA-Cancer J Clin* **2011,** *61* (4), 250-281.

48. Dougherty, T. J., A brief history of clinical photodynamic therapy development at Roswell Park Cancer Institute. *J Clin Laser Med Surg* **1996,** *14* (5), 219-21.

49. (a) Dougherty, T. J., Studies on the Structure of Porphyrins Contained in Photofrin-Ii. *Photochem Photobiol* **1987,** *46* (5), 569-573; (b) Herrera-Ornelas, L.; Petrelli, N. J.; Mittelman, A.; Dougherty, T. J.; Boyle, D. G., Photodynamic therapy in patients with colorectal cancer. *Cancer* **1986,** *57* (3), 677-84; (c) Brown, S. B.; Brown, E. A.; Walker, I., The present and future role of photodynamic therapy in cancer treatment. *Lancet Oncol* **2004,** *5* (8), 497-508.

50. (a) Sharman, W. M.; Allen, C. M.; van Lier, J. E., Photodynamic therapeutics: basic principles and clinical applications. *Drug Discov today* **1999,** *4* (11), 507-517; (b) Pushpan, S. K.; Venkatraman, S.; Anand, V. G.; Sankar, J.; Rath, H.; Chandrashekar, T. K., Inverted porphyrins and expanded porphyrins: An overview. *P Indian as-Chem Sci* **2002,** *114* (4), 311-338.

51. Lovell, J. F.; Liu, T. W. B.; Chen, J.; Zheng, G., Activatable Photosensitizers for Imaging and Therapy. *Chem Rev* **2010,** *110* (5), 2839-2857.

52. Chance, B., Optical Method. *Annu Rev Biophys Bio* **1991,** *20*, 1-28.

53. Josefsen, L. B.; Boyle, R. W., Unique Diagnostic and Therapeutic Roles of Porphyrins and Phthalocyanines in Photodynamic Therapy, Imaging and Theranostics. *Theranostics* **2012,** *2* (9), 916-966.

54. Ikeda, S.; Yanai, N.; Ishikawa, S., Flexible bronchofiberscope. *Keio J Med* **1968,** *17* (1), 1-16.

55. Weissleder, R., A clearer vision for in vivo imaging. *Nat Biotechnol* **2001,** *19* (4), 316-317.

56. Alander, J. T.; Kaartinen, I.; Laakso, A.; Patila, T.; Spillmann, T.; Tuchin, V. V.; Venermo, M.; Valisuo, P., A review of indocyanine green fluorescent imaging in surgery. *Int J Biom Imaging* **2012,** *2012*, 940585.

57. Frangioni, J. V., In vivo near-infrared fluorescence imaging. *Curr Opin Chem Biol* **2003,** *7* (5), 626-634.

58. Kobayashi, H.; Ogawa, M.; Alford, R.; Choyke, P. L.; Urano, Y., New strategies for fluorescent probe design in medical diagnostic imaging. *Chem Rev* **2010,** *110* (5), 2620-40.

59. Cohen, R.; Stammes, M. A.; de Roos, I. H.; Stigter-van Walsum, M.; Visser, G. W.; van Dongen, G. A., Inert coupling of IRDye800CW to monoclonal antibodies for clinical optical imaging of tumor targets. *EJNMMI research* **2011,** *1* (1), 31.

60. Mang, T. S.; Mcginnis, C.; Liebow, C.; Nseyo, U. O.; Crean, D. H.; Dougherty, T. J., Fluorescence Detection of Tumors - Early Diagnosis of Microscopic Lesions in Preclinical Studies. *Cancer* **1993,** *71* (1), 269-276.

61. Gregorie, H. B.; Horger, E. O.; Ward, J. L.; Green, J. F.; Richards, T.; Robertso.Hc; Stevenso.Tb, Hematoporphyrin-Derivative Fluorescence in Malignant Neoplasms. *Ann Surg* **1968,** *167* (6), 820-&.

62. Kennedy, J. C.; Pottier, R. H., Endogenous protoporphyrin IX, a clinically useful photosensitizer for photodynamic therapy. *J Photochem Photobiol. B, Biology* **1992,** *14* (4), 275-92.

63. Moghissi, K.; Stringer, M. R.; Dixon, K., Fluorescence photodiagnosis in clinical practice. *Photodiagn Photodyn* **2008,** *5* (4), 235-237.

64. Riedl, C. R.; Daniltchenko, D.; Koenig, F.; Simak, R.; Loening, S. A.; Pflueger, H., Fluorescence endoscopy with 5-aminolevulinic acid reduces early recurrence rate in superficial bladder cancer. *J Urology* **2001,** *165* (4), 1121-1123.

65. Boens, N.; Leen, V.; Dehaen, W., Fluorescent indicators based on BODIPY. *Chem Soc Rev* **2012,** *41* (3), 1130-72.

66. Li, L.; Nguyen, B.; Burgess, K., Functionalization of the 4,4-difluoro-4-bora-3a, 4a-diaza-s-indacene (BODIPY) core. *Bioorg Med Chem Lett* **2008,** *18* (10), 3112-3116.

67. Jiao, L.; Yu, C.; Li, J.; Wang, Z.; Wu, M.; Hao, E., Beta-formyl-BODIPYs from the Vilsmeier-Haack reaction. *J Org Chem* **2009,** *74* (19), 7525-8.

68. Banuelos, J.; Arroyo-Cordoba, I. J.; Valois-Escamilla, I.; Alvarez-Hernandez, A.; Pena-Cabrera, E.; Hu, R. R.; Tang, B. Z.; Esnal, I.; Martinez, V.; Arbeloa, I. L., Modulation of the photophysical properties of BODIPY dyes by substitution at their meso position. *Rsc Adv* **2011,** *1* (4), 677-684.

69. (a) Loudet, A.; Bandichhor, R.; Wu, L. X.; Burgess, K., Functionalized BF(2) chelated azadipyrromethene dyes. *Tetrahedron* **2008,** *64* (17), 3642-3654; (b) McDonnell, S. O.; O'shea, D. F., Near-infrared sensing properties of dimethlyamino-substituted BF2-azadipyrromethenes. *Org Lett* **2006,** *8* (16), 3493-3496.

70. Li, L. L.; Han, J. Y.; Nguyen, B.; Burgess, K., Syntheses and spectral properties of functionalized, water-soluble BODIPY derivatives. *J Org Chem* **2008,** *73* (5), 1963-1970.

71. Lee, J. I.; Klaerner, G.; Davey, M. H.; Miller, R. D., Color tuning in polyfluorenes by copolymerization with low band gap comonomers. *Synthetic Met* **1999,** *102* (1-3), 1087-1088.

72. Thivierge, C.; Bandichhor, R.; Burgess, K., Spectral dispersion and water solubilization of BODIPY dyes via palladium-catalyzed C-H functionalization. *Org Lett* **2007,** *9* (11), 2135-2138.

73. Pavlopoulos, T. G.; Boyer, J. H.; Shah, M.; Thangaraj, K.; Soong, M. L., Laser Action from 2,6,8-Position Trisubstituted 1,3,5,7-Tetramethylpyrromethene-Bf2 Complexes .1. *Appl Optics* **1990,** *29* (27), 3885-3886.

74. Niu, S. L.; Massif, C.; Ulrich, G.; Ziessel, R.; Renard, P. Y.; Romieu, A., Water-solubilisation and bio-conjugation of a red-emitting BODIPY marker. *Org Biomol Chem* **2011,** *9* (1), 66-69.

75. Rohand, T.; Baruah, M.; Qin, W. W.; Boens, N.; Dehaen, W., Functionalisation of fluorescent BODIPY dyes by nucleophilic substitution. *Chem Commun* **2006,** (3), 266-268.

76. (a) Ziessel, R.; Ulrich, G.; Harriman, A., The chemistry of Bodipy: a new El Dorado for fluorescence tools. *New J Chem* **2007,** *31* (4), 496-501; (b) Li, L.; Nguyen, B.; Burgess, K., Functionalization of the 4,4-difluoro-4-bora-3a,4a-diaza-s-indacene (BODIPY) core. *Bioorg Med Chem Lett* **2008,** *18* (10), 3112-6.

77. Ulrich, G.; Goeb, S.; De Nicola, A.; Retailleau, P.; Ziessel, R., Chemistry at boron: synthesis and properties of red to near-IR fluorescent dyes based on boron-substituted diisoindolomethene frameworks. *J Org Chem* **2011,** *76* (11), 4489-505.

78. Niu, S. L.; Ulrich, G.; Ziessel, R.; Kiss, A.; Renard, P. Y.; Romieu, A., Water-Soluble BODIPY Derivatives. *Org Lett* **2009,** *11* (10), 2049-2052.

79. Marshall, M. V.; Draney, D.; Sevick-Muraca, E. M.; Olive, D. M., Single-Dose Intravenous Toxicity Study of IRDye 800CW in Sprague-Dawley Rats. *Mol Imaging Biol* **2010,** *12* (6), 583-594.

80. Zhang, D. K.; Wang, Y. C.; Xiao, Y.; Qian, S. X.; Qian, X. H., Long-wavelength boradiazaindacene derivatives with two-photon absorption activity and strong emission: versatile candidates for biological imaging applications. *Tetrahedron* **2009,** *65* (39), 8099-8103.

81. Kele, P.; Li, X. H.; Link, M.; Nagy, K.; Herner, A.; Lorincz, K.; Beni, S.; Wolfbeis, O. S., Clickable fluorophores for biological labeling-with or without copper. *Org Biomol Chem* **2009,** *7* (17), 3486-3490.

82. Lakowicz, J. R., *Principles of Fluorescence Spectroscopy* Third ed.; Springer 2006.

83. Sato, K.; Nagai, Y.; Suzuki, M., Purification and Partial Characterization of an Acid Proteinase from Dirofilaria-Immitis. *Mol Biochem Parasit* **1993,** *58* (2), 293-299.

84. Geoghegan, K. F.; Emery, M. J.; Martin, W. H.; Mccoll, A. S.; Daumy, G. O., Site-Directed Double Fluorescent Tagging of Human Renin and Collagenase

(Mmp-1) Substrate Peptides Using the Periodate-Oxidation of N-Terminal Serine - an Apparently General Strategy for Provision of Energy-Transfer Substrates for Proteases. *Bioconjugate Chem* **1993,** *4* (6), 537-544.

85. Jones, L. J.; Upson, R. H.; Haugland, R. P.; PanchukVoloshina, N.; Zhou, M. J.; Haugland, R. P., Quenched BODIPY dye-labeled casein substrates for the assay of protease activity by direct fluorescence measurement. *Anal Biochem* **1997,** *251* (2), 144-152.

86. Han, F. F.; Xu, Y. M.; Jiang, D. C.; Qin, Y.; Chen, H. Y., A BODIPY-derived fluorescent probe for cellular pH measurements. *Anal Biochem* **2013,** *435* (2), 106-113.

87. Wu, Y. K.; Peng, X. J.; Guo, B. C.; Fan, J. L.; Zhang, Z. C.; Wang, J. Y.; Cui, A. J.; Gao, Y. L., Boron dipyrromethene fluorophore based fluorescence sensor for the selective imaging of Zn(II) in living cells. *Org Biomol Chem* **2005,** *3* (8), 1387-1392.

88. Dodani, S. C.; He, Q. W.; Chang, C. J., A Turn-On Fluorescent Sensor for Detecting Nickel in Living Cells. *J Am Chem Soc* **2009,** *131* (50), 18020-+.

89. Baruah, M.; Qin, W. W.; Vallee, R. A. L.; Beljonne, D.; Rohand, T.; Dehaen, W.; Boens, N., A highly potassium-selective ratiometric fluorescent indicator based on BODIPY azacrown ether excitable with visible light. *Org Lett* **2005,** *7* (20), 4377-4380.

90. Yuan, L.; Lin, W. Y.; Zheng, K. B.; He, L. W.; Huang, W. M., Far-red to near infrared analyte-responsive fluorescent probes based on organic fluorophore platforms for fluorescence imaging. *Chem Soc Rev* **2013,** *42* (2), 622-661.

91. Lakowicz, J., *Pinciples of Fluorescence Spectroscopy* Third ed.; Springer 2006.

92. Bestvater, F.; Spiess, E.; Stobrawa, G.; Hacker, M.; Feurer, T.; Porwol, T.; Berchner-Pfannschmidt, U.; Wotzlaw, C.; Acker, H., Two-photon fluorescence absorption and emission spectra of dyes relevant for cell imaging. *J Microsc-Oxford* **2002,** *208*, 108-115.

93. Loudet, A.; Ueno, Y.; Wu, L. X.; Jose, J.; Barhoumi, R.; Burghardt, R.; Burgess, K., Organelle-selective energy transfer: A fluorescent indicator of intracellular environment. *Bioorg Med Chem Lett* **2011,** *21* (6), 1849-1851.

94. (a) Keene, J. P.; Kessel, D.; Land, E. J.; Redmond, R. W.; Truscott, T. G., Direct Detection of Singlet Oxygen Sensitized by Hematoporphyrin and Related-Compounds. *Photochem Photobiol* **1986,** *43* (2), 117-120; (b) Baron, E. D.; Malbasa, C. L.; Santo-Domingo, D.; Fu, P. F.; Miller, J. D.; Hanneman, K. K.; Hsia, A. H.; Oleinick, N. L.; Colussi, V. C.; Cooper, K. D., Silicon Phthalocyanine (Pc 4) Photodynamic Therapy Is a Safe Modality for Cutaneous Neoplasms: Results of a Phase 1 Clinical Trial. *Laser Surg Med* **2010,** *42* (10), 728-735; (c) Lozovaya, G. I.; Masinovsky, Z.; Sivash, A. A., Protoporphyrin-Ix as a Possible Ancient Photosensitizer - Spectral and Photochemical Studies. *Origins Life Evol B* **1990,** *20* (3-4), 321-330; (d) Fernandez, J. M.; Bilgin, M. D.;

Grossweiner, L. I., Singlet oxygen generation by photodynamic agents. *J Photoch Photobio B* **1997,** *37* (1-2), 131-140.

95. Bonnett, R.; Charlesworth, P.; D. Djelal, B.; Foley, S.; J. McGarvey, D.; George Truscott, T., Photophysical properties of 5,10,15,20-tetrakis(m-hydroxyphenyl)porphyrin (m-THPP), 5,10,15,20-tetrakis(m-hydroxyphenyl)chlorin (m-THPC) and 5,10,15,20-tetrakis(m-hydroxyphenyl)bacteriochlorin (m-THPBC): a comparative study. *J Chem Soc, Perkin Trans 2* **1999,** (2), 325-328.

96. Pandey, R. K.; Sumlin, A. B.; Constantine, S.; Aoudia, M.; Potter, W. R.; Bellnier, D. A.; Henderson, B. W.; Rodgers, M. A.; Smith, K. M.; Dougherty, T. J., Alkyl ether analogs of chlorophyll-a derivatives .1. Synthesis, photophysical properties and photodynamic efficacy. *Photochem Photobiol* **1996,** *64* (1), 194-204.

97. Aveline, B.; Hasan, T.; Redmond, R. W., Photophysical and Photosensitizing Properties of Benzoporphyrin Derivative Monoacid Ring-a (Bpd-Ma). *Photochem Photobiol* **1994,** *59* (3), 328-335.

98. (a) He, J.; Larkin, H. E.; Li, Y. S.; Rihter, B. D.; Zaidi, S. I. A.; Rodgers, M. A. J.; Mukhtar, H.; Kenney, M. E.; Oleinick, N. L., The synthesis, photophysical and photobiological properties and in vitro structure-activity relationships of a set of silicon phthalocyanine PDT photosensitizers. *Photochem Photobiol* **1997,** *65* (3), 581-586; (b) Wang, K. K. H.; Wilson, J. D.; Kenney, M. E.; Mitra, S.; Foster, T. H., Irradiation-induced enhancement of Pc 4 fluorescence and changes in light scattering are potential dosimeters for Pc 4-PDT. *Photochem Photobiol* **2007,** *83* (5), 1056-1062; (c) Barker, C. A.; Findlay, K. S.; Bettington, S.; Batsanov, A. S.; Perepichka, I. F.; Bryce, M. R.; Beeby, A., Synthesis of new axially-disubstituted silicon-phthalocyanine derivatives: optical and structural characterisation. *Tetrahedron* **2006,** *62* (40), 9433-9439.

99. (a) Awuah, S. G.; Polreis, J.; Biradar, V.; You, Y., Singlet oxygen generation by novel NIR BODIPY dyes. *Org Lett* **2011,** *13* (15), 3884-7; (b) Yogo, T.; Urano, Y.; Ishitsuka, Y.; Maniwa, F.; Nagano, T., Highly efficient and photostable photosensitizer based on BODIPY chromophore. *J Am Chem Soc* **2005,** *127* (35), 12162-3; (c) Yogo, T.; Urano, Y.; Ishitsuka, Y.; Maniwa, F.; Nagano, T., Highly efficient and photostable photosensitizer based on BODIPY chromophore. *J Am Chem Soc* **2005,** *127* (35), 12162-12163.

100. Gorman, A.; Killoran, J.; O'Shea, C.; Kenna, T.; Gallagher, W. M.; O'Shea, D. F., In vitro demonstration of the heavy-atom effect for photodynamic therapy. *J Am Chem Soc* **2004,** *126* (34), 10619-10631.

101. Cakmak, Y.; Kolemen, S.; Duman, S.; Dede, Y.; Dolen, Y.; Kilic, B.; Kostereli, Z.; Yildirim, L. T.; Dogan, A. L.; Guc, D.; Akkaya, E. U., Designing excited states: theory-guided access to efficient photosensitizers for photodynamic action. *Angew Chem Int Ed Engl* **2011,** *50* (50), 11937-41.

102. Awuah, S. G.; Das, S. K.; D'Souza, F.; You, Y., Thieno-Pyrrole-Fused BODIPY Intermediate as a Platform to Multifunctional NIR Agents. *Chem Asian J* **2013,** *8* (12), 3123-32.

103. Awuah, S. G.; Polreis, J.; Prakash, J.; Qiao, Q. Q.; You, Y. J., New pyran dyes for dye-sensitized solar cells. *J Photoch Photobio A* **2011,** *224* (1), 116-122.

104. Gagne, R. R.; Koval, C. A.; Lisensky, G. C., Ferrocene as an Internal Standard for Electrochemical Measurements. *Inorg Chem* **1980,** *19* (9), 2854-2855.

105. Awuah, S.G.;Bandi, V.; Das, S. K.; You, Y.; D'Souza, F., Thieno-pyrrole-fused 4,4-difluoro-4-bora-3a,4a-diaza-s-indacene-fullerene dyads: utilization of near-infrared sensitizers for ultrafast charge separation in donor-acceptor systems. *J Am Chem Soc* **2014,** *136* (21), 7571-4.

106. (a) Amin, A. N.; El-Khouly, M. E.; Subbaiyan, N. K.; Zandler, M. E.; Fukuzumi, S.; D'Souza, F., A novel BF2-chelated azadipyrromethene-fullerene dyad: synthesis, electrochemistry and photodynamics. *Chem Commun (Camb)* **2012,** *48* (2), 206-8; (b) Zhang, C. S.; Zhao, J. Z.; Wu, S.; Wang, Z. L.; Wu, W. H.; Ma, J.; Guo, S.; Huang, L., Intramolecular RET Enhanced Visible Light-Absorbing Bodipy Organic Triplet Photosensitizers and Application in Photooxidation and Triplet-Triplet Annihilation Upconversion. *J Am Chem Soc* **2013,** *135* (28), 10566-10578.

107. Guo, S*. et al.* BODIPY triads triplet photosensitizers enhanced with intramolecular resonance energy transfer (RET): broadbandvisible light absoption and application in photoxidaiton *Chemical Science* **2014,** *5*, 489-500.

108. Anyanee Kamkae, S. H. L., Hong Boon Lee, Lik Voon Kiew, Lip Yong Chung, Kevin Burgess, BODIPY Dyes in photodyanmic therapy. *Chemical Society reviews* **2013,** *42*, 77-78.

109. Sibata, C. H.; Colussi, V. C.; Oleinick, N. L.; Kinsella, T. J., Photodynamic therapy in oncology. *Expert opinion on pharmacotherapy* **2001,** *2* (6), 917-27.

110. Chen, B.; Pogue, B. W.; Luna, J. M.; Hardman, R. L.; Hoopes, P. J.; Hasan, T., Tumor vascular permeabilization by vascular-targeting photosensitization: Effects, mechanism, and therapeutic implications. *Clin Cancer Res* **2006,** *12* (3), 917-923.

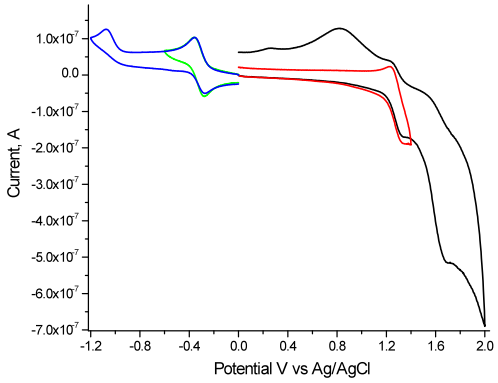
111. Chen, B.; Pogue, B. W.; Hoopes, P. J.; Hasan, T., Vascular and cellular targeting for photodynamic therapy. *Crit Rev Eukar Gene* **2006,** *16* (4), 279-305.

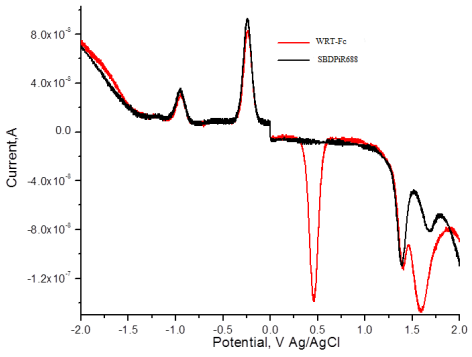
112. Kitai, T.; Inomoto, T.; Miwa, M.; Shikayama, T., Fluorescence navigation with indocyanine green for detecting sentinel lymph nodes in breast cancer. *Breast cancer* **2005,** *12* (3), 211-5.

113. Kelderhouse, L. E.; Chelvam, V.; Wayua, C.; Mahalingam, S.; Poh, S.; Kularatne, S. A.; Low, P. S., Development of Tumor-Targeted Near Infrared Probes for Fluorescence Guided Surgery. *Bioconjugate Chem* **2013,** *24* (6), 1075-1080.

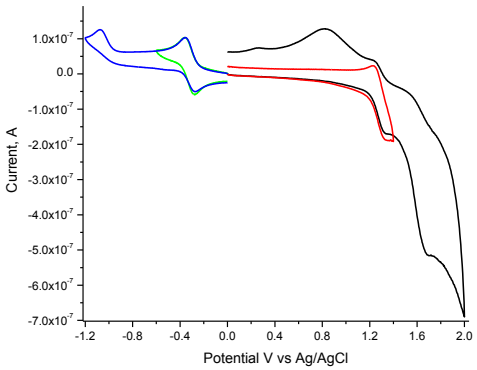
114. Chen, B.; Pogue, B. W.; Hoopes, P. J.; Hasan, T., Vascular and cellular targeting for photodynamic therapy. *Crit Rev Eukaryot Gene Expr* **2006,** *16* (4), 279-305.

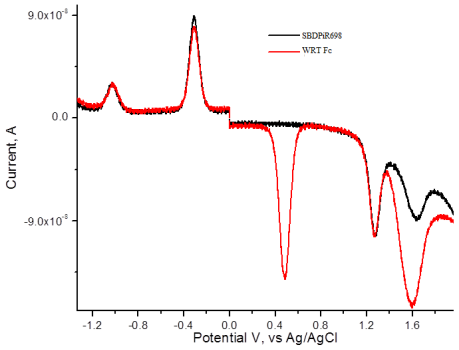
Appendix



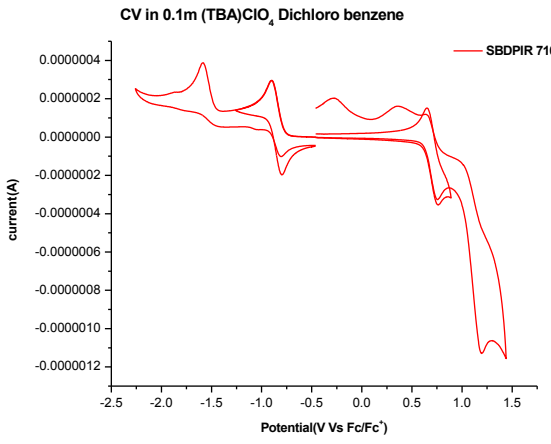


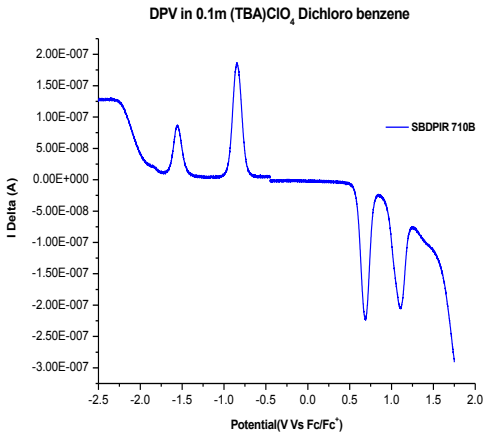
SBDPiR688





SBDPiR698





SBDPiR710

Figure 65. Cyclic voltammogram and differential pulse voltammetry.

List of Abbreviations

^{1}H NMR	Proton Nuclear Magnetic Resonance
$^1O_2$:	Singlet Oxygen
^{1}PS:	Singlet State Photosensitizer
$^3O_2$:	Molecular Oxygen
^{3}PS:	Triplet State Photosensitizer
BDP	BODIPY
BODIPY	4,4-Difluoro-4-bora-3a, 4a-diaza-s-indacene
$CDCl_3$	Deuterated Chloroform
CD_2Cl_2	Deuterated Methylene Chloride
COOR	Ester
DCM	Dichloromethane
DPBF	1,3-Diphenylisobenzofuran
Femto	10^{-15}
fPS	fluorescent Photosensitizers
HOMO	Highest Occupied Molecular Orbital
HPLC	High Pressure Liquid Chromatography
HRMS EI	High Resolution Mass Spectrometry Electron Impact
IUPAC	International Union of Pure and Applied Chemistry
LED	Light Emitting Diodes
LIFE	Light Induced Fluorescence Emission

LRMS EI	Low Resolution Mass Spectrometry Electron Impact
LUMO	Lowest Unoccupied Molecular Orbital
Nano	10^{-9}
PDT	Photodynamic Therapy
Pico	10^{-12}
PSFD	Photosensitizer Fluorescence Detection
SBDPiR	Thiophene-fused BODIPY Infrared

List of ^{1}H NMR Spectra

Spectrum Page

1. ^{1}H NMR spectrum of compound **35**……61
2. ^{1}H NMR spectrum of compound **36**……62
3. ^{1}H NMR spectrum of compound **BDP635**……..63
4. ^{1}H NMR spectrum of compound **SBDPIR690**……...64
5. ^{1}H NMR spectrum of compound **SBDPIR731**……...65
6. ^{1}H NMR spectrum of compound **SBDPiR698**……66
7. ^{1}H NMR spectrum of compound **SBDPiR688**……67
8. ^{1}H NMR spectrum of compound **SBDPiR740**……69
9. ^{1}H NMR spectrum of compound **SBDPiR710** ……...70
10. ^{1}H NMR spectrum of compound **SBDPiR700**……72
11. ^{1}H NMR spectrum of compound **SBDPiR690-COOR**……..99
12. ^{1}H NMR spectrum of compound **BDP635-COOR**……...101
13. ^{1}H NMR spectrum of compound **SBDPiR688-COOR**……103

List of Reaction Schemes

Scheme Page

1. Synthesis of NIR BODIPY PS ……...…….……...40
2. Synthesis of **SBDPIR690-COOR**……...……...……88
3. Synthesis of **BDP635-COOR**……...……...…..93
4. Synthesis of **SBDPiR688-COOR**……...……94

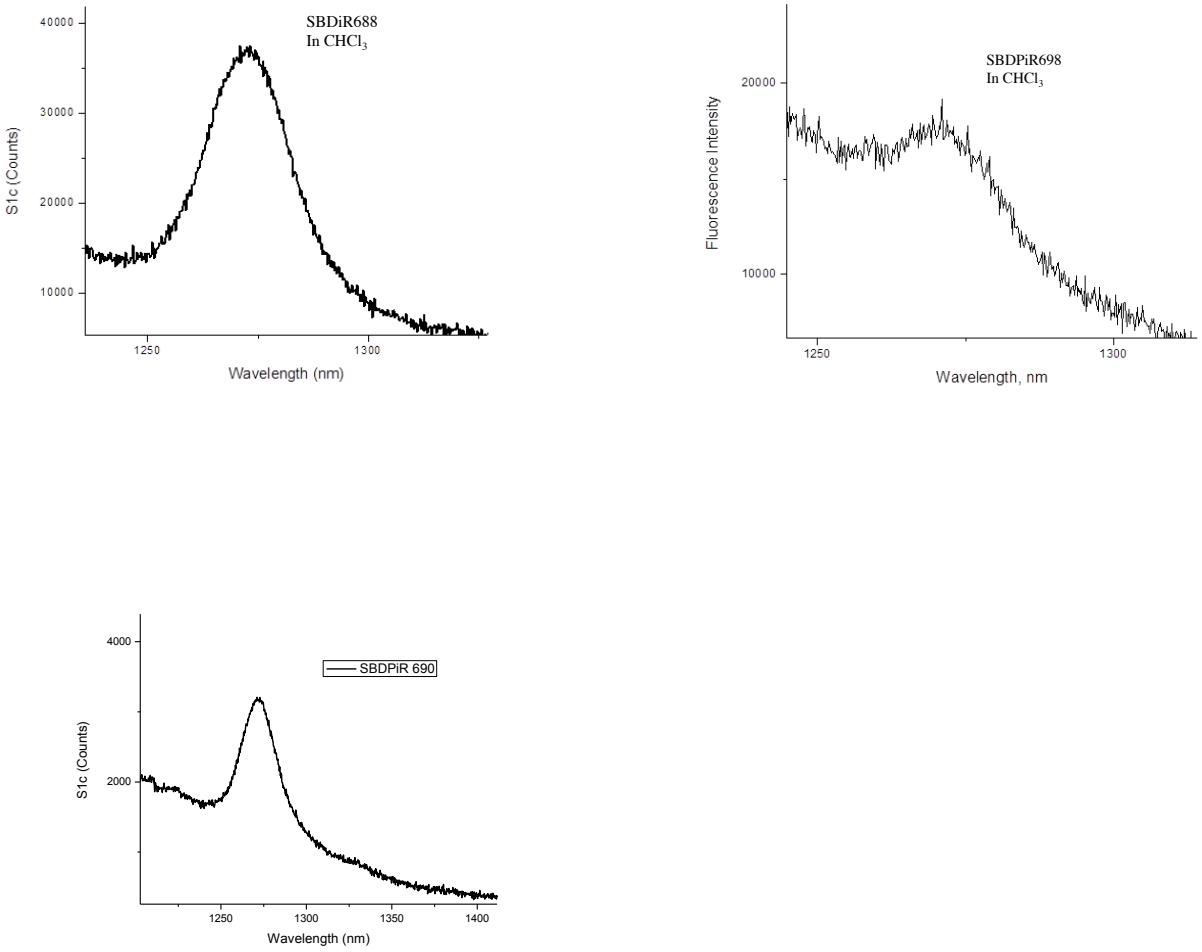


Figure 66. Singlet Oxygen Luminescence

Table 5. **X-ray crystal structure of SBDPiR690**

Crystal data and structure refinement for **SBDPiR690.**

Identification code	p21c	
Empirical formula	C26 H14 B F5 N2 S2	
Formula weight	524.32	
Temperature	200(2) K	
Wavelength	0.71073 Å	
Crystal system	Monoclinic	
Space group	P 21/c	
Unit cell dimensions	a = 13.976(3) Å	α = 90°.
	b = 11.672(3) Å	β= 111.368(4)°.
	c = 14.646(4) Å	γ = 90°.
Volume	2224.9(9) $Å^3$	
Z	4	
Density (calculated)	1.565 Mg/m^3	
Absorption coefficient	0.301 mm^{-1}	
F(000)	1064	
Crystal size	0.20 x 0.16 x 0.03 mm^3	
Theta range for data collection	1.56 to 26.02°.	
Index ranges	-17<=h<=17, -14<=k<=14, -18<=l<=18	
Reflections collected	19787	
Independent reflections	4387 [R(int) = 0.1118]	
Completeness to theta = 26.02°	100.0 %	
Absorption correction	Semi-empirical from equivalents	
Max. and min. transmission	0.9916 and 0.9417	
Refinement method	Full-matrix least-squares on F^2	
Data / restraints / parameters	4387 / 0 / 325	
Goodness-of-fit on F^2	1.025	
Final R indices [I>2sigma(I)]	R1 = 0.0657, wR2 = 0.1128	
R indices (all data)	R1 = 0.1606, wR2 = 0.1407	
Largest diff. peak and hole	0.428 and -0.339 $e.Å^{-3}$	

Atomic coordinates (x 10^4) and equivalent isotropic displacement parameters ($Å^2$x 10^3)

for **SBDPiR690**. U(eq) is defined as one third of the trace of the orthogonalized U^{ij} tensor.

---

	x	y	z	U(eq)
S(1)	857(1)	6931(1)	5385(1)	58(1)
F(1)	3459(2)	3260(2)	5971(2)	64(1)
N(1)	2124(2)	4322(3)	4771(2)	41(1)
C(1)	1669(3)	4996(3)	5243(3)	41(1)
B(1)	2594(4)	3146(4)	5115(3)	46(1)
S(2)	3879(1)	110(1)	3302(1)	62(1)
F(2)	1897(2)	2438(2)	5309(2)	65(1)
N(2)	2875(3)	2673(3)	4287(2)	46(1)
C(2)	1428(3)	4884(3)	6082(3)	46(1)
F(3)	3722(3)	5178(3)	2652(2)	113(1)
C(3)	984(3)	5854(3)	6260(3)	45(1)
F(4)	2326(3)	4592(3)	1688(2)	107(1)
C(4)	1411(3)	6056(3)	4760(3)	44(1)
F(5)	2418(3)	6128(3)	2440(2)	134(2)
C(5)	1718(3)	6041(4)	3980(3)	53(1)
C(6)	2172(3)	4945(3)	3978(3)	45(1)
C(7)	2613(3)	4427(4)	3369(3)	48(1)
C(8)	2944(3)	3289(4)	3495(3)	48(1)
C(9)	3324(3)	2536(4)	2940(3)	54(1)
C(10)	3471(3)	1492(4)	3387(3)	50(1)
C(11)	3684(3)	-290(4)	4377(3)	51(1)
C(12)	3318(3)	591(3)	4776(3)	49(1)
C(13)	3197(3)	1591(3)	4218(3)	44(1)
C(14)	619(3)	6048(4)	7063(3)	52(1)
C(15)	-62(4)	6937(4)	7024(4)	69(1)
C(16)	-428(4)	7046(5)	7786(5)	86(2)
C(17)	-132(5)	6312(6)	8560(5)	92(2)
C(18)	552(5)	5464(5)	8606(4)	86(2)
C(19)	937(4)	5334(4)	7869(3)	72(2)
C(20)	3876(3)	-1464(4)	4767(3)	57(1)
C(21)	3579(4)	-1787(4)	5534(3)	64(1)
C(22)	3783(4)	-2869(4)	5950(4)	71(1)
C(23)	4282(4)	-3653(4)	5595(4)	80(2)
C(24)	4583(4)	-3346(4)	4832(4)	77(2)

C(25)	4392(4)	-2260(4)	4407(3)	68(1)
C(26)	2748(4)	5088(4)	2541(3)	62(1)

Bond lengths [Å] and angles [°] for **SBDPiR690.**

S(1)-C(4)	1.732(4)
S(1)-C(3)	1.757(4)
F(1)-B(1)	1.394(5)
N(1)-C(1)	1.350(4)
N(1)-C(6)	1.392(4)
N(1)-B(1)	1.526(5)
C(1)-C(2)	1.394(5)
C(1)-C(4)	1.405(5)
B(1)-F(2)	1.383(5)
B(1)-N(2)	1.509(5)
S(2)-C(10)	1.731(4)
S(2)-C(11)	1.756(4)
N(2)-C(13)	1.357(5)
N(2)-C(8)	1.397(5)
C(2)-C(3)	1.361(5)
C(2)-H(2A)	0.9500
F(3)-C(26)	1.315(6)
C(3)-C(14)	1.460(5)
F(4)-C(26)	1.306(5)
C(4)-C(5)	1.358(5)
F(5)-C(26)	1.288(5)
C(5)-C(6)	1.428(5)
C(5)-H(5A)	0.9500
C(6)-C(7)	1.394(5)
C(7)-C(8)	1.396(5)
C(7)-C(26)	1.506(6)
C(8)-C(9)	1.425(5)
C(9)-C(10)	1.363(6)

C(9)-H(9A)	0.9500
C(10)-C(13)	1.408(5)
C(11)-C(12)	1.370(5)
C(11)-C(20)	1.472(6)
C(12)-C(13)	1.399(5)
C(12)-H(12A)	0.9500
C(14)-C(19)	1.380(6)
C(14)-C(15)	1.395(6)
C(15)-C(16)	1.394(7)
C(15)-H(15A)	0.9500
C(16)-C(17)	1.359(7)
C(16)-H(16A)	0.9500
C(17)-C(18)	1.361(7)
C(17)-H(17A)	0.9500
C(18)-C(19)	1.378(6)
C(18)-H(18A)	0.9500
C(19)-H(19A)	0.9500
C(20)-C(21)	1.385(6)
C(20)-C(25)	1.392(6)
C(21)-C(22)	1.385(6)
C(21)-H(21A)	0.9500
C(22)-C(23)	1.364(6)
C(22)-H(22A)	0.9500
C(23)-C(24)	1.377(7)
C(23)-H(23A)	0.9500
C(24)-C(25)	1.394(7)
C(24)-H(24A)	0.9500
C(25)-H(25A)	0.9500

C(4)-S(1)-C(3)	91.03(18)
C(1)-N(1)-C(6)	107.3(3)
C(1)-N(1)-B(1)	125.5(3)
C(6)-N(1)-B(1)	126.9(3)
N(1)-C(1)-C(2)	135.0(4)
N(1)-C(1)-C(4)	109.7(3)
C(2)-C(1)-C(4)	115.3(3)

F(2)-B(1)-F(1)	108.5(3)
F(2)-B(1)-N(2)	110.8(4)
F(1)-B(1)-N(2)	111.3(4)
F(2)-B(1)-N(1)	110.7(4)
F(1)-B(1)-N(1)	109.9(4)
N(2)-B(1)-N(1)	105.6(3)
C(10)-S(2)-C(11)	91.1(2)
C(13)-N(2)-C(8)	107.0(3)
C(13)-N(2)-B(1)	126.2(3)
C(8)-N(2)-B(1)	126.6(3)
C(3)-C(2)-C(1)	111.3(4)
C(3)-C(2)-H(2A)	124.3
C(1)-C(2)-H(2A)	124.3
C(2)-C(3)-C(14)	126.9(4)
C(2)-C(3)-S(1)	112.8(3)
C(14)-C(3)-S(1)	120.3(3)
C(5)-C(4)-C(1)	108.1(3)
C(5)-C(4)-S(1)	142.3(3)
C(1)-C(4)-S(1)	109.6(3)
C(4)-C(5)-C(6)	106.9(3)
C(4)-C(5)-H(5A)	126.6
C(6)-C(5)-H(5A)	126.6
N(1)-C(6)-C(7)	118.3(4)
N(1)-C(6)-C(5)	108.0(3)
C(7)-C(6)-C(5)	133.7(4)
C(6)-C(7)-C(8)	122.0(3)
C(6)-C(7)-C(26)	120.5(4)
C(8)-C(7)-C(26)	117.5(4)
C(7)-C(8)-N(2)	118.7(3)
C(7)-C(8)-C(9)	133.3(4)
N(2)-C(8)-C(9)	108.0(4)
C(10)-C(9)-C(8)	107.4(3)
C(10)-C(9)-H(9A)	126.3
C(8)-C(9)-H(9A)	126.3
C(9)-C(10)-C(13)	107.6(4)
C(9)-C(10)-S(2)	142.6(3)

C(13)-C(10)-S(2)	109.8(3)
C(12)-C(11)-C(20)	125.2(4)
C(12)-C(11)-S(2)	112.8(3)
C(20)-C(11)-S(2)	122.0(3)
C(11)-C(12)-C(13)	111.2(4)
C(11)-C(12)-H(12A)	124.4
C(13)-C(12)-H(12A)	124.4
N(2)-C(13)-C(12)	135.0(3)
N(2)-C(13)-C(10)	110.0(4)
C(12)-C(13)-C(10)	115.0(4)
C(19)-C(14)-C(15)	119.1(4)
C(19)-C(14)-C(3)	119.9(4)
C(15)-C(14)-C(3)	121.0(4)
C(16)-C(15)-C(14)	118.6(5)
C(16)-C(15)-H(15A)	120.7
C(14)-C(15)-H(15A)	120.7
C(17)-C(16)-C(15)	121.5(5)
C(17)-C(16)-H(16A)	119.3
C(15)-C(16)-H(16A)	119.3
C(16)-C(17)-C(18)	119.6(5)
C(16)-C(17)-H(17A)	120.2
C(18)-C(17)-H(17A)	120.2
C(17)-C(18)-C(19)	120.6(6)
C(17)-C(18)-H(18A)	119.7
C(19)-C(18)-H(18A)	119.7
C(18)-C(19)-C(14)	120.5(5)
C(18)-C(19)-H(19A)	119.7
C(14)-C(19)-H(19A)	119.7
C(21)-C(20)-C(25)	118.4(5)
C(21)-C(20)-C(11)	120.2(4)
C(25)-C(20)-C(11)	121.4(5)
C(20)-C(21)-C(22)	122.0(4)
C(20)-C(21)-H(21A)	119.0
C(22)-C(21)-H(21A)	119.0
C(23)-C(22)-C(21)	119.7(5)
C(23)-C(22)-H(22A)	120.1

C(21)-C(22)-H(22A)	120.1
C(22)-C(23)-C(24)	119.0(5)
C(22)-C(23)-H(23A)	120.5
C(24)-C(23)-H(23A)	120.5
C(23)-C(24)-C(25)	122.3(5)
C(23)-C(24)-H(24A)	118.9
C(25)-C(24)-H(24A)	118.9
C(20)-C(25)-C(24)	118.6(5)
C(20)-C(25)-H(25A)	120.7
C(24)-C(25)-H(25A)	120.7
F(5)-C(26)-F(4)	106.9(4)
F(5)-C(26)-F(3)	104.5(5)
F(4)-C(26)-F(3)	103.9(4)
F(5)-C(26)-C(7)	115.5(4)
F(4)-C(26)-C(7)	113.4(4)
F(3)-C(26)-C(7)	111.6(4)

Symmetry transformations used to generate equivalent atoms:

Anisotropic displacement parameters ($Å^2 x\ 10^3$) for **SBDPiR690**. The anisotropic displacement factor exponent takes the form: $-2\pi^2[\ h^2\ a^{*2}U^{11} + ... + 2\ h\ k\ a^*\ b^*\ U^{12}\ ]$

	U^{11}	U^{22}	U^{33}	U^{23}	U^{13}	U^{12}
S(1)	72(1)	42(1)	63(1)	0(1)	27(1)	13(1)
F(1)	81(2)	74(2)	36(1)	7(1)	23(1)	32(2)
N(1)	55(2)	37(2)	36(2)	7(2)	22(2)	8(2)
C(1)	50(3)	38(2)	38(2)	-1(2)	20(2)	2(2)
B(1)	62(4)	42(3)	42(3)	3(2)	28(3)	10(3)
S(2)	67(1)	69(1)	56(1)	-26(1)	29(1)	4(1)
F(2)	95(2)	41(1)	83(2)	13(1)	62(2)	15(1)
N(2)	58(3)	44(2)	40(2)	0(2)	25(2)	8(2)
C(2)	55(3)	46(3)	43(2)	0(2)	23(2)	6(2)
F(3)	89(3)	169(3)	90(2)	46(2)	45(2)	-23(2)
C(3)	44(3)	43(2)	47(2)	-8(2)	17(2)	2(2)
F(4)	152(3)	128(3)	40(2)	1(2)	34(2)	-54(2)

C(4)	49(3)	37(2)	47(2)	0(2)	18(2)	1(2)
F(5)	246(5)	95(2)	116(3)	55(2)	131(3)	55(3)
C(5)	60(3)	48(3)	46(2)	9(2)	15(2)	-1(2)
C(6)	49(3)	49(3)	39(2)	6(2)	17(2)	2(2)
C(7)	52(3)	58(3)	36(2)	3(2)	17(2)	-4(2)
C(8)	53(3)	59(3)	38(2)	1(2)	22(2)	2(2)
C(9)	53(3)	74(3)	40(2)	-13(2)	23(2)	-4(3)
C(10)	49(3)	60(3)	42(2)	-16(2)	17(2)	0(2)
C(11)	47(3)	55(3)	52(2)	-16(2)	19(2)	0(2)
C(12)	57(3)	48(3)	46(2)	-8(2)	23(2)	8(2)
C(13)	51(3)	49(3)	36(2)	-6(2)	18(2)	5(2)
C(14)	44(3)	58(3)	56(3)	-19(2)	20(2)	0(2)
C(15)	60(3)	67(3)	81(3)	-31(3)	25(3)	-1(3)
C(16)	66(4)	90(4)	114(5)	-58(4)	46(4)	-7(3)
C(17)	80(5)	124(6)	87(4)	-61(4)	50(4)	-35(4)
C(18)	91(5)	117(5)	63(3)	-17(3)	41(3)	1(4)
C(19)	80(4)	93(4)	55(3)	-7(3)	41(3)	17(3)
C(20)	51(3)	49(3)	67(3)	-25(2)	16(3)	1(2)
C(21)	65(4)	48(3)	78(3)	-9(3)	25(3)	4(3)
C(22)	71(4)	48(3)	88(4)	-8(3)	22(3)	4(3)
C(23)	72(4)	50(3)	107(4)	-21(3)	20(4)	-2(3)
C(24)	62(4)	56(4)	105(4)	-38(3)	20(3)	8(3)
C(25)	55(3)	60(3)	81(3)	-26(3)	14(3)	10(3)
C(26)	82(4)	69(4)	44(3)	6(2)	32(3)	-4(3)

Hydrogen coordinates (x 10^4) and isotropic displacement parameters (Å^{2}x 10^3) for SBDPiR690.

	x	y	z	U(eq)
H(2A)	1557	4215	6479	56
H(5A)	1645	6644	3524	63
H(9A)	3452	2727	2364	64

H(12A)	3167	531	5356	59
H(15A)	-271	7457	6488	83
H(16A)	-896	7646	7764	104
H(17A)	-401	6391	9067	110
H(18A)	766	4956	9150	104
H(19A)	1425	4749	7917	86
H(21A)	3224	-1251	5783	77
H(22A)	3576	-3063	6481	85
H(23A)	4421	-4400	5870	96
H(24A)	4932	-3892	4587	93
H(25A)	4609	-2067	3883	82

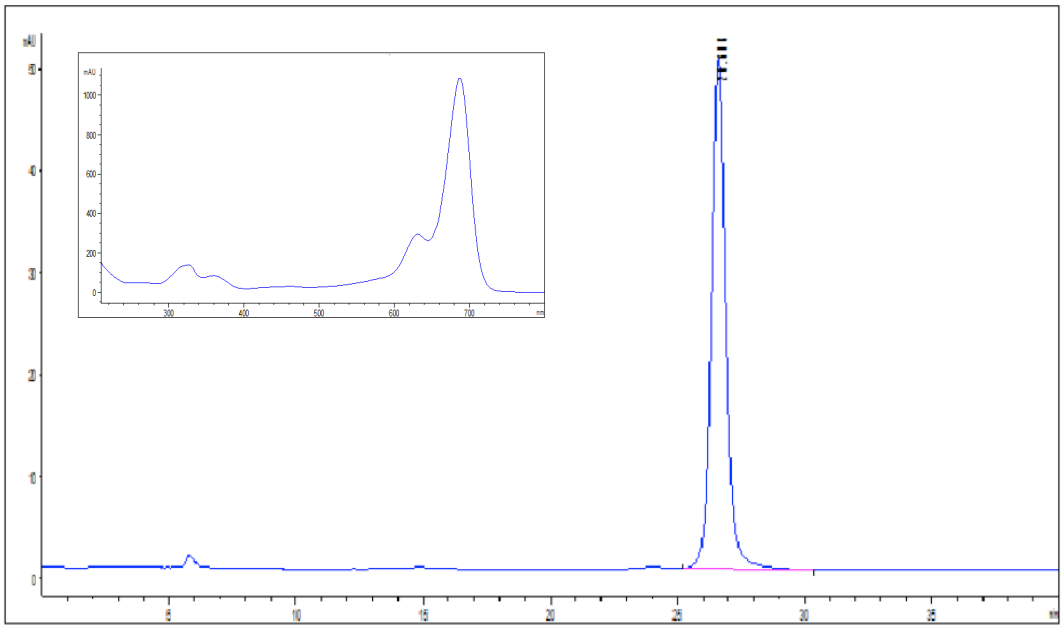


Figure 67. HPLC Chromatogram of SBDPiR690: mobile phase = 100% acetonitrile, flow rate 0.25 ml/min, detection at 254 nm, rt (retention time) = 26.61 min; purity = 99 %. SBDPiR690.

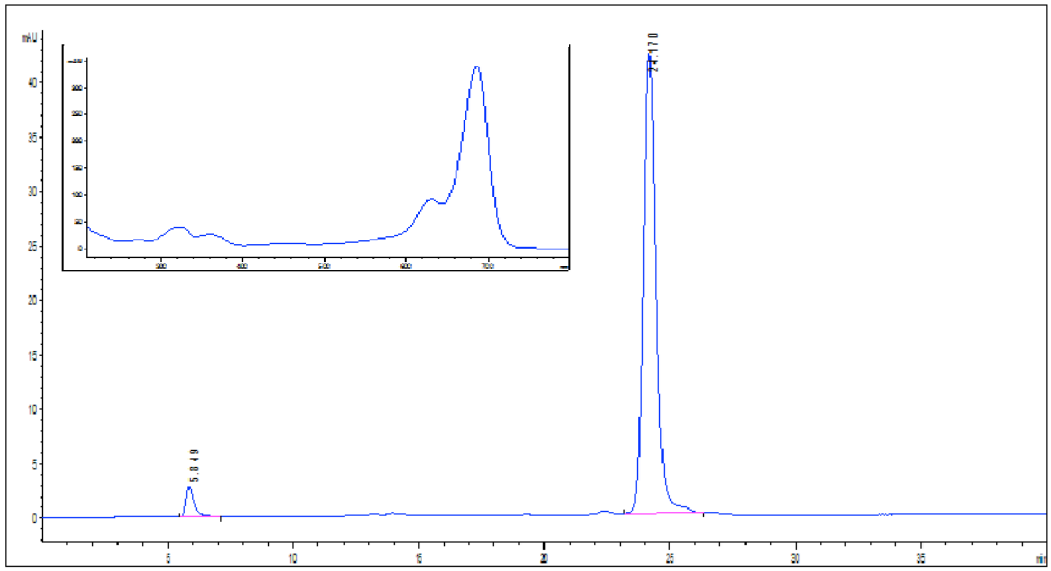


Figure 68. HPLC Chromatogram of SBDPiR698: mobile phase = 100% acetonitrile, flow rate 0.25 ml/min, detection at 254 nm, rt (retention time) = 24.17 min; purity = 96 %.

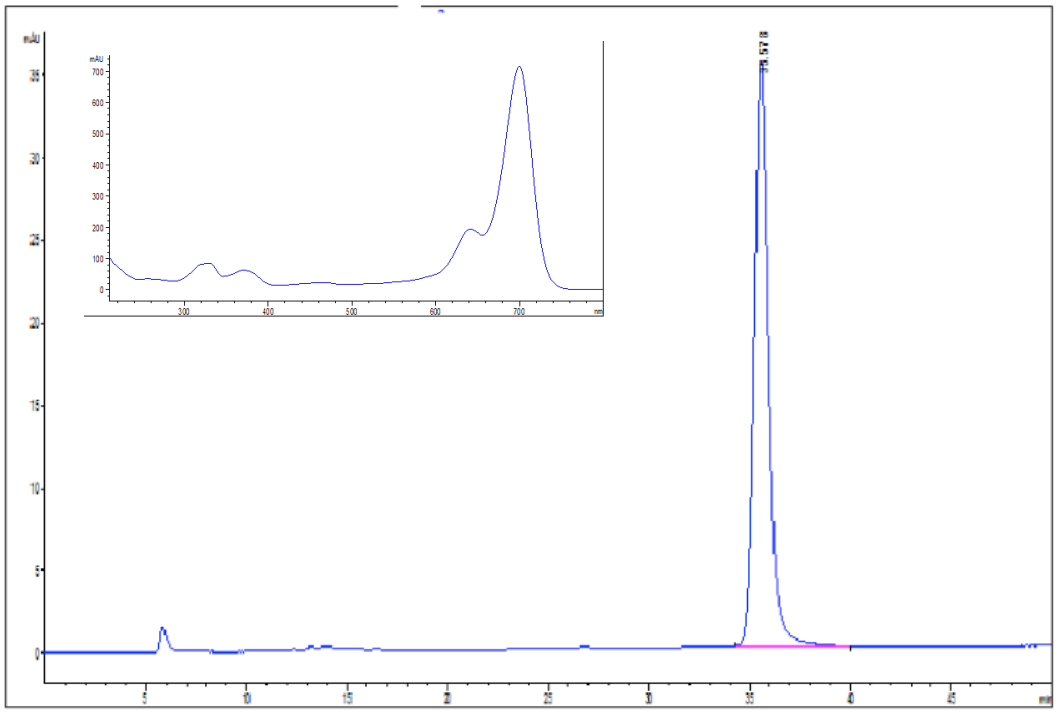


Figure 69. HPLC Chromatogram of SBDPiR688: mobile phase = 100% acetonitrile, flow rate 0.25 ml/min, detection at 254 nm, rt (retention time) = 26.91 min; purity = 94 %.

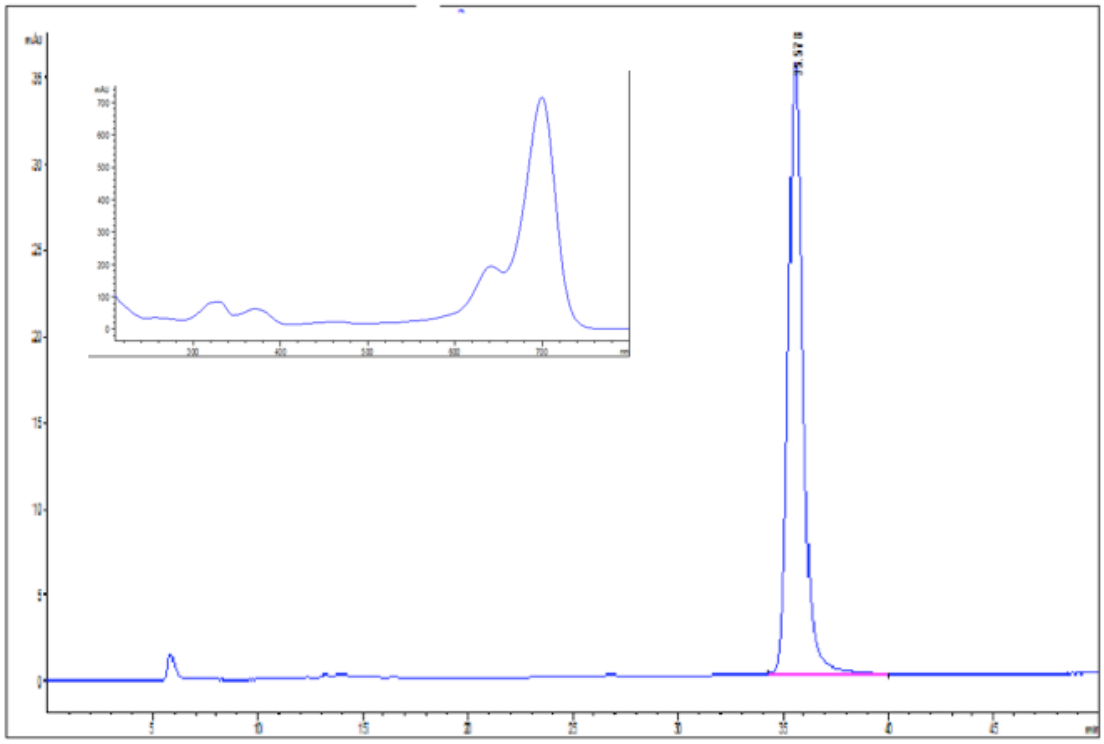


Figure 70. HPLC Chromatogram of SBDPiR710: mobile phase = 100% acetonitrile, flow rate 0.25 ml/min, detection at 254 nm, rt (retention time) = 35.58 min; purity = 99 %.